Nolinear Dynamics of Tapping Mode Atomic Force Microscopy

Arash Bahrami

Dissertation submitted to the Faculty of the

Virginia Polytechnic Institute and State University

in partial fulfillment of the requirements for the degree of

Doctor of Philosophy

in

Engineering Mechanics

Ali H. Nayfeh, Co-Chair

Muhammad R. Hajj, Co-Chair

Shane D. Ross

Rafaella De Vita

Mark R. Paul

August 3, 2012

Blacksburg, Virginia

Keywords: Nonlinear Dynamics, Atomic Force Microscopy, Tapping Mode, Multimode

Galerkin Procedure, Differential Quadrature Method

Nolinear Dynamics of Tapping Mode Atomic Force Microscopy

Arash Bahrami

(ABSTRACT)

A mathematical model is developed to investigate the grazing dynamics of tapping mode atomic force microscopes (AFM) subjected to a base harmonic excitation. The nonlinear dynamics of the AFM microcantilever are studied in both of the monostable and bistable phases with the microcantilever tip being, respectively, located in the monostable and bistable regions of the static bifurcation diagram in the reference configuration. Free-vibration responses of the AFM probes, including the microcantilever natural frequencies and mode shapes, are determined. It is found that, for the parameters used in a practical operation of an AFM, the natural frequencies and mode shapes of the AFM microcantilever are almost the same as those of a free-end microcantilever with the same geometry and made of an identical material. A multimode Galerkin approximation is utilized to discretize the nonlinear partial-differential equation of motion and associated boundary conditions governing the cantilever response and obtain a set of nonlinearly coupled ordinary-differential equations (ODE) governing the time evolution of the system dynamics. The corresponding nonlinear ODE set is then solved using numerical integration schemes. A comprehensive numerical analysis is performed for a wide range of the excitation amplitude and frequency. The tip oscillations are examined using nonlinear dynamic tools through several examples. The non-smoothness in the tip/sample interaction model is treated rigorously. A higher-mode

Galerkin analysis indicates that period doubling bifurcations and chaotic vibrations are possible in tapping mode microscopy for certain operating parameters. It is also found that a single-mode Galerkin approximation, which accurately predicts the tip nonlinear responses far from the sample, is not adequate for predicting all of the nonlinear phenomena exhibited by an AFM, such as grazing bifurcations, and leads to both quantitative and qualitative errors. A point-mass model is also developed based on the single-mode Galerkin procedure to compare with the present distributed-parameter model.

In addition, a reduced-order model based on a differential quadrature method (DQM) is employed to explore the dynamics of the AFM probe in the bistable phase where the multi-mode Galerkin procedure is computationally expensive. We found that the DQM with a few grid points accurately predicts the static bifurcation diagram. Moreover, we found that the DQM is capable of precise prediction of the lowest natural frequencies of the microcantilever with only a few grid points. For the higher natural frequencies, however, a large number of grid points is required. We also found that the natural frequencies and mode shapes of the microcantilever about non-contact equilibrium positions are almost the same as those of the free-end microcantilever. On the other hand, free-vibration responses of the microcantilever about contact equilibrium positions are quite different from those of the free-end microcantilever. Moreover, we used the DQM to discretize the partial-differential equation governing the microcantilever motion and a finite-difference method (FDM) to calculate limit-cycle responses of the AFM tip. It is shown that a combination of the DQM and FDM applied, respectively, to discretize the spatial and temporal derivatives provides an efficient, accurate

procedure to address the complicated dynamic behavior exhibited by the AFM probe. The procedure was, therefore, utilized to study the response of the microcantilever to a base harmonic excitation through several numerical examples. We found that the dynamics of the AFM probe in the bistable region is totally different from those in the monostable region.

Dedication

I dedicate this dissertation to my parents Bijan and Fereshteh.

Acknowledgments

I would like to express my deepest gratitude and appreciation to my advisor, Dr. Ali Nayfeh for his insightful advice and compassionate support throughout my Ph.D. studies. I appreciate his tremendous insight, guidance, resourcefulness, kindness, and patience throughout this research. He introduced me to the wonders, accomplishments, and frustrations of a scientific research and opened my eyes to the unreasonable beauties of nonlinear science. Dr. Nayfeh's mentorship style granted me freedom and independence without which my achievements would have been of less significance and flavor. I would also like to extend my appreciation to my co-advisor, Dr. Muhammad Hajj for believing in me and for his endless supports not only as my co-advisor but also as the ESM department graduate director. It would have been impossible to complete my Ph.D. without his continuous helps and encouragement.

I am very grateful to have the opportunity to work under the supervision of Dr. Romesh Batra during the summers I collaborated with him. I appreciate his passion for research, his excellent teaching, and his exemplary scientific personality. I would also like to thank Dr.

Glenn Kraige for his genuine guidance and numerous help when I was his teaching assistant and an instructor for Dynamics in the ESM department. It was one of the greatest honors of my academic life to get the chance to work with him as a teaching assistant and an instructor. His skillful teaching, his admirable sense of responsibility, and his caring attitudes towards his students would remain an inspiration to me throughout my entire life. Many thanks go to Dr. Shane Ross, Dr. Rafaella De Vita, and Dr. Mark Paul for serving in my committee and providing valuable inputs on this research.

It is hardly enough to mention the debt I owe to my Masters advisor at Sharif University of Technology, Dr. Asghar Nosier for his excellent lectures, for teaching me how to face a scientific problem and how to think independently and creatively, and for challenging me to grow. He was the first brilliant scholar I met in my academic life whose inspiring personality sparked my interest in theoretical mechanics and propelled me to pursue my studies towards the Ph.D. degree.

I would like to acknowledge my brother Dr. Amir Bahrami and my friends Dr. Alireza Karimi, Dr. Amin Karami, and Mr. Hodjat Pendar for useful discussions during the course of this work. I wish to express sincere thanks to all my friends and especially my roommates who helped me enjoy the life during the years of my Ph.D. in Blacksburg. Our staunch friendship and unforgettable memories we made together have been engraved on my mind and will never fade. I am also thankful to Mrs. Sally Shrader for her helps and friendship.

Last but not least, words cannot be brought to express my heartfelt, eternal gratitude, appreciation, and thanks to my wonderful mother Fereshteh, my diligent father Bijan, and my

kind siblings Amir, Iman, and Azita for their everlasting love and unconditional supports and prayers throughout my life. I feel fortunate to have such a supportive family which has always offered me courage, inspiration, and strength to prevail over the personal difficulties and professional challenges in the arduous times of my life. In a way, my Ph.D. degree in Engineering Mechanics is the crop of the seeds my parents planted years ago by their immaculate training and never-ending sacrifices. To them, I wish to dedicate this dissertation.

Although my tenure at Virginia Tech is about to end, I truly believe that the lessons I have learned here, will prove to be of profound impact throughout my entire life. I would like to conclude this section with a verse of my favorite Iranian poet Hafiz:

It's an abomination

to rely on abstinence and wisdom

Hundred crafts though he may know

the seeker shall trust divine grace

Blacksburg, Virginia, August 3, 2012

Contents

List of Figures

List of Tables

Chapter 1

Introduction

1.1 Background

Scanning probe microscopy (SPM) [1] has been demonstrated as one of the most powerful tools to investigate the surface topography and measure local mechanical and chemical properties of materials in nanometer scales. The basic principle of the scanning probe microscopy is surprisingly simple in a sense that the surface information is gathered by scanning the surface with a mechanical probe rather than using an incident beam (light or electrons) as in classical microscopy. A sharp probe moves mechanically across the sample surface and the probe-sample interactions are monitored and used to generate topographical images of the surface. Scanning probe microscopy, in fact, started with the invention of a scanning tunneling microscope (STM) in 1982 [2]. The STM invention was quickly followed by the atomic

force microscope (AFM) introduced by Binnig, Quate, and Gerber in 1986 [3]. Among the large family of scanning probe microscopy, atomic force microscopy is widely utilized to generate atomic or near-atomic resolution images and measure different mechanical and chemical properties of a large variety of materials, including biological substrates, polymers, and biomaterials on fine scales, down to the level of molecules and atoms [4–14]. More particularly, applications of the AFM in biological science have remarkably increased in recent years and continue to grow at a rapid pace. Modern atomic force microscopy imaging techniques have opened a new avenue to the world of living cells, proteins, cellular membranes, and DNA. Cell biologists have applied the AFM's unique capabilities to study the dynamic behavior of living cells, such as red and white blood cells, and bacteria. A high-resolution topographical image of a cellular membrane constructed by an AFM probe is seen in Fig. 1.1 [15].

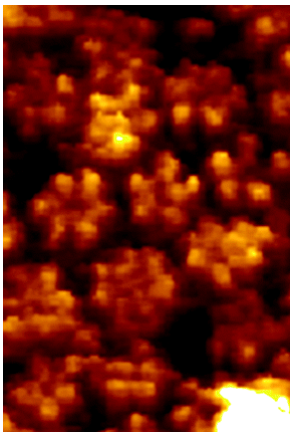

Figure 1.1: A high-resolution topographical image of a cell membrane generated by the AFM, [15] D.J. Muller. AFM: A Nanotool in Membrane Biology. Biochemistry, **47**, 7986, 2008, Used under fair use guidelines, 2012.

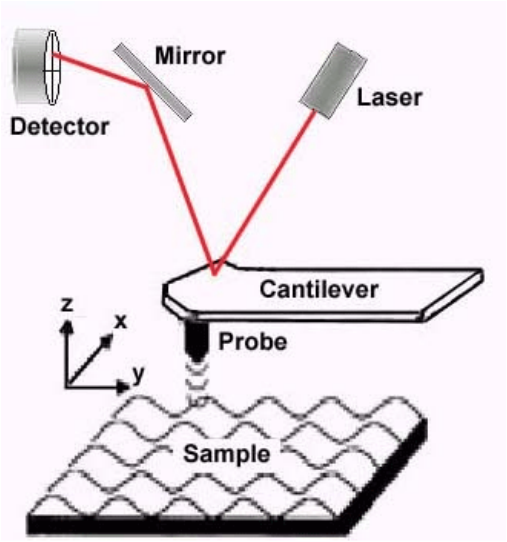

Figure 1.2: AFM operation mechanism.

1.2 Basic Principles of Atomic Force Microscopy

An atomic force microscope, in essence, consists of a nanoscale tip mounted on a micro scale flexible cantilever. Most commercial microcantilevers are either v-shaped or rectangular beams. AFM microcantilevers and tips are usually made of silicon or silicon nitride and are fabricated based on microfabrication techniques [6, 8]. Recently, some attempts have been made to use carbon nanotubes (CNT) as tips for AFM experiments [16]. Due to their high modulus of elasticity and other desirable mechanical and chemical properties, carbon nanotube tips may lead to substantial enhancement of imaging processes.

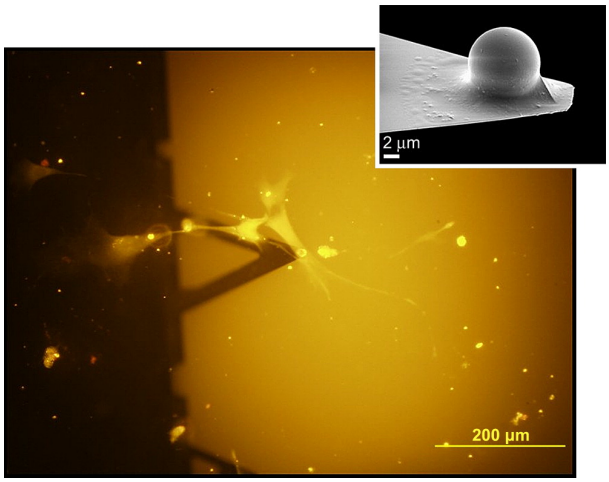

Figure 1.3: Single cell indentation experiment using AFM, [17] M. Nikkhah, J.S. Strobl, R. De Vita, and M. Agah. The cytoskeletal organization of breast carcinoma and fibroblast cells inside three dimensional (3-D) isotropic silicon microstructures. Biomaterials, **31**, (16) 4552, 2010, Used under fair use guidelines, 2012.

1.2.1 AFM Operational Modes

In general, the AFM may be used in three different operational modes: contact mode, non-contact mode, and tapping mode. In the contact mode, the probe tip maintains close contact with the sample surface and the static deflection of the microcantilever tip is used as a feedback signal. In this mode, the interaction force between the sample and the AFM tip is kept constant by maintaining a constant deflection while the probe is scanning the sample surface. The main disadvantage of contact mode atomic force microscopy is that the tip might damage the sample surface, specially when soft materials, such as biological samples, are probed.

In the non-contact mode, on the contrary, the tip does not touch the sample surface, but it oscillates over the sample during scanning. In this operational regime, the microcantilever is driven to oscillate near its first natural frequency. Because most samples are covered with liquid layers, it is difficult to keep the AFM tip in close proximity of the sample so that the long-range interaction forces become detectable and to prevent the tip from contacting the surface. Therefore, non-contact mode imaging is usually performed in an ultra vacuum conditions to generate high-resolution images.

The tapping mode or intermittent contact atomic force microscopy was developed to address difficulties involved in the contact and non-contact imaging modes and to provide more opportunities for achieving enhanced surface images. In the tapping mode operation of the AFM, the probe is often subjected to a harmonic base excitation at or near its fundamental natural frequency [6–8]. The external excitation is usually performed via a dither piezo. As the microcantilever oscillates in the vicinity of the sample, the deflection of the microcantilever tip is influenced by the intermolecular interaction forces between the tip and the sample. As depicted in Fig. 1.2, this deflection is usually measured using a laser spot focused on the probe tip and reflected into a photodiode, which is then used for nanoscale characterization of the sample. The capability of the tapping mode AFM to generate high-resolution images in a variety of ambient media, such as air and liquid, has been already established [6–8].

As aforementioned, a particular interaction parameter, such as the amplitude or frequency, is chosen as the feedback parameter. Depending on the choice of the feedback parameter,

atomic force microscopy is classified as frequency modulation (FM) AFM and amplitude modulation (AM) AFM [6]. In the frequency modulation AFM, the feedback parameter is a frequency shift between the resonant frequency far from the sample and the resonant frequency in proximity of the sample. In the amplitude modulation AFM, however, variations in either the oscillation amplitude or the phase provide the feedback signal for imaging purposes. Although the amplitude modulation AFM has been utilized in the non-contact mode by employing very stiff microcantilevers in ultra vacuum conditions, it is mainly associated with the operation of the tapping mode AFM.

1.2.2 Tip/Sample Interaction Forces

The complexity of AFM dynamics, in essence, stems from the nonlinear interaction forces between the microcantilever tip and the sample surface. In the absence of the nonlinear tip/sample interactions, the AFM dynamics reduce to the simple vibration problem of a free-end microcantilever subjected to an external excitation. The dynamics of the microcantilever, on the other hand, are directly influenced by these interaction forces. Therefore, providing a reliable tip/sample interaction model is a critical part in any AFM study. A variety of tip/sample interaction models have been reported in the literature, so far. Depending on the tip geometry, the sample material, and the operating medium, the tip/sample interactions may be approximated by different models. In air, the dominant forces are long-range van der Waals interactions, short-range repulsive interactions, and capillary effects. When the AFM operates in a fluid, the electrostatic double-layer, Derjaguin-Landau-Verwey-Overbeek, and

solvation forces should be considered, in addition [6]. The van der Waals forces, which are of electromagnetic origin, are always attractive in air or in vacuum, but might be repulsive between different materials in liquids [6].

The repulsive contact forces, which arise upon touching the sample by the probe tip, are described based on contact mechanics models. Both continuum-based models and atomic simulations have been already employed to investigate the contact mechanism between the tip and the sample. Atomic analysis of the tip/sample interactions confirms that continuum mechanics models are quite reliable in describing the tip/sample interactions. According to the continuum-based contact theory, first proposed by Hertz in 1881 [18], the surface deformation that develops upon the tip/sample contact depends on the applied force, the geometry, and the material properties of the contacting surfaces. In the Hertz formulation, the contact problem is described by the deformations of two elastic spheres without considering the adhesion forces. Later, Johnson, Kendall, and Roberts (JKR) [19] and Derjaguin, Muller, and Toporov (DMT) [20] proposed analytical models for the contact forces in which the adhesion force acting outside the contact area are also included. We note that the contact forces are short-range interactions and do not come into play in the non-contact operation of AFM probes, whereas the long-range van der Waals forces are always present in all imaging modes.

Under ambient conditions, a nanoscale water bridge forms between the AFM tip and the sample due to the humidity in the surrounding air. The water-layer thickness depends on the relative humidity. The formation of the water bridge has been reported in all of the AFM

imaging modes, including the contact, non-contact, and tapping modes. This water bridge results in capillary forces, which in some cases can dominate all other tip/sample interaction forces and cause a significant amount of energy dissipation [21, 22].

1.3 Literature Review

Atomic force microscopy has received considerable attention since its initial report in 1982 [2]. The dynamics of AFM probes have driven tremendous research because they directly affect the imaging process. Particularly, a deep understanding of the nonlinear effects is crucial for enhancing the imaging contrast and resolution. For the sake of brevity, we mainly focus on the research done on tapping mode atomic force microscopy in the present study. Because both of the long-range attractive force, which is present in both of the contact and non-contact regions, and the short-range repulsive force emerging only in the contact region are nonlinear functions of the instantaneous tip/sample separation, the dynamics of the microcantilever with intermittent contacts are quite complicated. In addition, the nonlinear tip/sample interaction force is not differentiable at the contact point, which results in a non-smooth nonlinear dynamical system, requiring special treatment.

Despite the intense research, most published papers model the continuous (distributed-parameter) AFM probe as a point-mass single-degree-of-freedom system [8, 11–13, 21–27]. In this approach, the cantilever stiffness is determined based on a simple static analysis and the equivalent mass is obtained using the calculated value for the stiffness and the

cantilever first natural frequency [7] $\omega_1 = \sqrt{\frac{k_{eq}}{m_{eq}}}$. The point-mass approach is not only incapable of modeling the higher-vibration modes and possible coupling between them, but also may fail to accurately predict the dynamics of the cantilever [28, 29]. In addition, in most point-mass models, the piezo excitation is modeled as an external force acting on the equivalent mass [8, 11, 12]. However, in practice, the base of a microcantilever is subjected to a displacement excitation through a piezoelectric actuator. Including a base excitation as a displacement in the analysis introduces more complicated nonlinear dynamics due to the parametric excitation phenomenon [30, 31], which is not captured in other models. In contrast to lumped parameter models, little attention has been paid to continuous modeling of AFMs [28, 29, 32–38]. In spite of the complexities involved in modeling and analyzing an AFM probe as a continuous microcantilever rather than a point mass, such models are able to predict all of the nonlinear aspects of AFM dynamics, such as grazing bifurcations [39] and jumps, and often provide more precise and deeper insight into the physics of AFMs [28, 29].

In conventional imaging techniques, an AFM microcantilever is excited at or near its fundamental natural frequency and the feedback acts on the amplitude of its mode. Recently some researchers employed nonlinear modal interactions to get more information on the surface properties of the samples and achieve new imaging techniques. Rodriguez and Garcia [33] proposed the simultaneous excitation of the first two modes of the microcantilever to increase the compositional sensitivity of an AFM while reducing the force exerted on the sample. Later, Martinez et al. [40] utilized the output signal of the first mode to image the topography of the sample and used the phase shift of both of the first and second

modes to measure variations in the compositions of the atoms or molecules under the tip. This approach, which is called bimodal AFM [40–44], is compatible with air as well as liquid environments. Because of the significant reduction in the magnitudes of the tip/sample interaction forces, bimodal atomic force microscopy offers new possibilities for imaging extremely soft materials, such as living cells and soft polymers. However, the theoretical foundations of this so-called dual or multifrequency excitation are to be understood yet.

In addition to the eigenmodes of the microcantilever, the higher harmonics of the oscillation may be used in multifrequency approaches. We note that the higher harmonics have frequencies equal to integer multiples of the excitation frequency; they are generated by the nonlinear contact and van der Waals forces arising between the sample and the AFM tip. Nonlinear interactions between the torsional and flexural modes of the microcantilever can be, on the other hand, employed to construct novel imaging schemes. Sahin et al. [45–48] have measured the flexibility of proteins within a membrane with high spatial resolution using the torsional harmonics. Furthermore, the parametric excitation phenomenon [30] has been used to develop another category of non-conventional imaging schemes [49]. The theoretical development of this approach is poorly understood and has remained in a focus of current research.

In continuous or distributed-parameter models, the dynamics of the AFM microcantilever are governed by nonlinear partial-differential equations in space and time. The partial-differential equations and associated boundary conditions form a nonlinear initial-boundary value problem. Closed-form analytical solutions are, in general, very hard to find for this

class of problems and limited to a few special cases with very simple geometry. Therefore, approximate solutions are sought to estimate the dynamics of the system. Broadly speaking, approximate solutions are classified into numerical techniques and analytical methods. In numerical techniques, such as finite element, finite difference, and finite volume techniques, the original partial-differential equations and associated boundary conditions are transformed into a set of finite number of algebraic equations, which are solved subsequently using a variety of numerical schemes. Analytical methods, on the other hand, are divided into two categories: direct and reduced-order methods. In direct methods, a perturbation techniques [50, 51] is used to attack directly the nonlinear partial-differential equations and associated boundary conditions. In reduced-order methods, such as the Galerkin procedure, the differential quadrature method (DQM) [52–55], and the method of harmonic balance, the response is decomposed into distinct spatial and temporal parts and either the temporal or the spatial part is, then, discretized. In the method of harmonic balance, the temporal part is discretized using harmonic functions and the partial-differential equations are reduced to a set of ordinary-differential equations in terms of the spatial variable. In the DQM and Galerkin procedures, however, the spatial derivative is approximated and the distributed-parameter problem is reduced to a set of nonlinearly coupled differential equations governing the time evolution of the system dynamics.

1.4 Contributions

A quick literature survey indicates that a variety of point-mass models have been introduced so far to explore the dynamics of AFM probes. However, all of them model the external excitation as a force rather than a base displacement. Therefore, we develop an equivalent point-mass model for the three-dimensional microcantilever/tip structure subjected to a base displacement excitation. This point-mass model is used only for the sake of comparison.

Among all different discretization methods, the Galerkin procedure based on projection of the nonlinear response onto the eigenfunctions of the linear system has been mostly utilized to discretize the partial-differential equation and associated boundary conditions governing the vibrations of AFM microcantilevers. A comprehensive literature survey reveals that, although some papers have used a multimode Galerkin procedure to analyze the dynamics of AFM probes operating in liquids, to the best of our knowledge, all of the papers dealing with continuous models of AFMs assume that only the first mode participates in the response when the excitation frequency is close to the first natural frequency of the microcantilever [28, 29], irrespective of whether the AFM operates in air or vacuum. Hence, they provide no measure of how the obtained solution approximates the exact solution. It is known, on the other hand, that a single-mode Galerkin discretization is not adequate for accurate estimation of nonlinear responses, especially, in the presence of quadratic nonlinearities [56, 57]. In fact, the tip/sample interaction forces in both of the contact and non-contact regimes are very complicated, in essence, and a simple Taylor series expansion indicates that different types

of nonlinearity, including cubic and quadratic as well as parametric excitation terms, are present in the model. In addition, static analysis of the AFM microcantilever indicates that, although a single-mode Galerkin discretization is sufficient to recover the non-contact portion of the static bifurcation diagram, the contact portion is recovered only when six or more modes are employed in the Galerkin discretization.

In the present work, multi-flexural mode shapes are employed to discretize the partial-differential equation of motion and associated boundary conditions through a Galerkin procedure. It is shown, even while an AFM is operated in air, a single-mode Galerkin discretization is not sufficient to capture all of the nonlinear phenomena and leads to quantitative as well as qualitative errors. The number of modes needed to accurately predict the dynamics of an AFM probe is also determined through a convergence study. Furthermore, using Lagrange's equation of motion, we present a new formulation to investigate the nonlinear dynamics of an AFM microcantilever.

It is shown that, employing four flexural mode shapes in the Galerkin discretization, period doubling bifurcations and chaotic motions are detected. Such phenomena are not detectable using a single-mode Galerkin discretization. On the other hand, it has been demonstrated experimentally that, depending on the AFM operational parameters such as excitation frequency, initial tip/sample separation gap, and the damping coefficient, period doubling bifurcations and a weakly chaotic motion might occur in a real atomic force microscope [58–60]. However, under typical imaging conditions, a chaotic motion is not desirable and should be avoided [59, 60]. The topographical images generated by scanning a chaot-

ically oscillating tip over the sample exhibit small but significant errors at the nanoscale by introducing a deterministic uncertainty in mapping [59]. This will lead to considerable reduction in the imaging quality and contrast and deteriorate the ability of an AFM to perform high-resolution mapping. Characterizing the underlying physics would allow us to improve the imaging performance and quality by keeping the AFM operational parameters, like the excitation frequency, in a range where undesirable responses, such as chaotic motions are avoided. Understanding the AFM nonlinear dynamics can also provide helpful information to design an AFM probe for different imaging or measuring purposes. Throughout this investigation, we provide a solid theoretical framework to study the nonlinear dynamics of amplitude-modulation atomic force microscopes. We apply the present methodology to predict nonlinear phenomena, such as grazing and period doubling bifurcations and chaos, for a real AFM. Although numerical simulations are performed for a certain AFM parameters the present methodology could be applied to analyze the dynamics of any AFM probe with different geometric and material properties and might be used as a guide to practical operations of AFMs.

In the Galerkin procedure, the mode shapes about the equilibrium tip/sample separation are used as basis functions to discretize the partial-differential equation of motion and associated boundary conditions into spatial and temporal parts. On the other hand, the nonlinear interaction forces between the tip and the sample depend on the instantaneous tip/sample separation and therefor the shear force boundary condition is hard to satisfy, especially when the microcantilever tip passes from one operating state (i.e., contact or non-contact)

to another. Thus, this shear force boundary condition may be satisfied only approximately by increasing the number of mode shapes. A multimode Galerkin discretization, on the other hand, involves lengthy algebra and costly computations, especially when a large number of mode shapes is required. In contrast, the DQM provides a systematic procedure in which the discretized equations and associated boundary conditions are expressed in terms of matrix equations [56, 57]. In addition to computational efficiency, the DQM matrix-based formulation is very convenient for computer programming and the desired accuracy can be achieved by simply increasing the number of grid points [53, 54]. Furthermore, the DQM is well-suited for the study of the tip motion in the sense that the DQM approximates the spatial derivatives of the microcantilever deflection by a weighted linear sum of the deflection values at given discrete points, including the end point (i.e., the point at which the microcantilever tip is located). We also use the DQM to obtain the static deflection, the natural frequencies, and the mode shapes of the AFM microcantilever and compare them with the exact values.

Then, we utilize the discretized equations obtained based on the DQM to study the dynamics of the AFM probe subjected to a base harmonic excitation. Because forward integration in time is computationally expensive, we employ the finite difference method (FDM) [31] to compute limit-cycle responses of the dynamical system. We note that the FDM not only provides an efficient way for calculating stable limit cycles, but it is also capable of calculating unstable limit cycles, which cannot be calculated using forward integration [31]. We also note that the FDM can be applied only when the dynamical system exhibits a periodic solution and chaotic or quasi-periodic responses can not be captured using the FDM.

1.5 Outline

This dissertation covers the following:

Chapter 2: We use the Hamiltonian formulation to develop mathematical frameworks to study the nonlinear dynamics of an AFM probe based on both distributed-parameter and point-mass models. In addition, we introduce exact analytical solutions for the static and free-vibration analysis of an AFM microcantilever.

Chapter 3: We employ a multimode Galerkin procedure to discretize the initial-boundary-value problem governing microcantilever oscillations. Then, we use a rigorous numerical integration scheme to solve the initial-value problem, found based on the Galerkin discretization, and discuss the nonlinear dynamics of the AFM probe in the monostable phase through various numerical examples. We also present numerical results for the static deflection, natural frequencies, and mode shapes of the AFM microcantilever.

Chapter 4: We utilize the differential quadrature method (DQM) to discretize the partial-differential equation of motion and then employ the finite difference method (FDM) to determine periodic solutions of the corresponding dynamical system. We discuss in detail the free and forced vibrations of the AFM probe in the bistable phase using a combination of the DQM and FDM. Furthermore, we present some numerical results for an AFM operating in the monostable phase.

Chapter 5: We present conclusions and suggestions for future investigations.

Chapter 2

Mathematical Modeling

In this chapter, a mathematical model is developed to study the dynamics of an AFM in the tapping operation mode. Using microelectronic fabrication techniques, one fabricates the microcantilever and the tip as a single devise; that is, microcantilever/tip system. This system is, in fact, a three-dimensional continuous structure. The tip dimensions and mass are smaller than those of the microcantilever by several orders of magnitude and, therefore, the inertia and geometry of the tip are not factors in modeling the microcantilever/tip system. However, the tip geometry and material properties are taken into consideration in modeling the interaction forces arising between the tip and the sample. The three-dimensional microcantilever/tip system may be modeled here either as a continuous beam structure or as a point-mass single-degree-of-freedom system. We consider only non-contact van der Waals and contact DMT forces and use the extended Hamilton principle to obtain a mathematical formulation governing the microcantilever/tip motion.

2.1 Continuous model

As aforementioned, the microcantilever is modeled based on the Euler-Bernoulli assumptions for small deflections. Euler-Bernoulli beam theory assumes that the cross-section of the beam is infinitely rigid in its own plane; that is, no deformations occur in the plane of the cross-section. In addition, the cross-section planes are assumed to remain plane and normal to the deformed axis of the beam. Consequently, the transverse shear stresses are ignored according to the Euler-Bernoulli beam theory and the rotation of the cross-section is due to bending only [61].

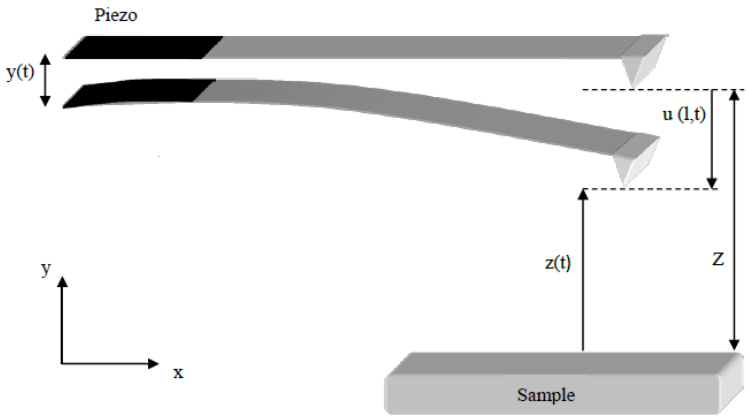

Figure 2.1: A schematic of an AFM.

As shown in figure 2.1, Z denotes the tip/sample separation distance in the reference configuration and $u(x,t)$ indicates the total deflection of the microcantilever, which can be expressed as $w(x,t)+y(t)$, where $w(x,t)$ is the deflection of the microcantilever relative to a non-inertial reference frame attached to the base. The base excitation from a dither piezo is

assumed to be a harmonic displacement; that is, $y(t) = Y\sin(\Omega t)$. Hence, the instantaneous tip/sample separation can be written as $z(t) = Z - w(l,t) - y(t)$.

2.1.1 Tip/Sample Interaction Forces

As the microcantilever oscillates in close proximity of the sample, its dynamics are significantly affected by the nonlinear distant-dependent interaction forces between the cantilever tip and the sample surface. So far, a variety of tip/sample interaction models have been utilized to simulate the AFM dynamics. Long-range interactions of the van der Waals type between the tip and the sample may be approximated by assuming a spherical tip apex and a flat sample surface as follows [6, 8]:

$$F_{vdW} = -\frac{HR}{6z^2}$$

where F_{vdW} represents the van der Waals non-contact force; H and R, are, respectively, the Hamaker constant and the tip radius. We note that the van der Waals force is always attractive in air or vacuum. For rough surfaces, the roughness of the sample surface might be, alternatively, approximated by a succession of half spheres and, therefore, the sphere-sphere approximation is used rather than sphere-flat geometry to estimate the van der Waals interactions [6]:

$$F_{vdW} = -\frac{H}{6z^2}\frac{R_t R_s}{R_t + R_s}$$

with R_t and R_s being the tip radius and the effective radius of the surface under the tip, respectively.

Among the several models available in the existing literature, the DMT model [20] is used here to approximate the short-range repulsive tip/sample interactions, arising during the contact period:

$$F_r = \frac{4}{3} E^* \sqrt{R} (a_0 - z)^{3/2}$$

where F_r represents the repulsive contact force; a_0 signifies the intermolecular distance at which contact is initiated; and E^* is the effective modulus of elasticity of the tip/sample interface, which is given by [20]

$$\frac{1}{E^*} = \frac{1 - \nu_{tip}^2}{E_{tip}} + \frac{1 - \nu_{sample}^2}{E_{sample}}$$

Here, ν_{tip} and E_{tip} are, respectively, the Poisson ratio and modulus of elasticity of the cantilever material and, similarly, ν_{sample} and E_{sample} are those of the sample material. We note that several assumptions have been made in developing the DMT model: all deformations are assumed to be in the linear elastic range and the contact geometry is axisymmetric with no shear force. In addition, the contact area is assumed to be small compared to the tip apex area, which is, presumably, a sphere. We note that the attractive van der Waals forces are present even when the AFM tip is in contact with the sample, but it is assumed to be constant during contact. Therefore, the total contact force based on the DMT model can be expressed as

$$F_{DMT} = -\frac{HR}{6a_0^2} + \frac{4}{3} E^* \sqrt{R} (a_0 - z)^{3/2}$$

We neglect the capillary effect in the present research and use the following tip/sample

interaction model throughout this Dissertation:

$$F(z) = \begin{cases} F_{vdW} = -\frac{HR}{6z^2} & \text{if } z \geq a_0 \\ F_{DMT} = -\frac{HR}{6a_0^2} + \frac{4}{3}E^*\sqrt{R}(a_0 - z)^{3/2} & \text{if } z < a_0 \end{cases} \tag{2.1}$$

2.1.2 Equation of Motion and Boundary Conditions

The total kinetic energy of the microcantilever is given by

$$T = \frac{1}{2}\int_0^l \rho A \left[\dot{w}(x,t) + \dot{y}(t)\right]^2 dx \tag{2.2}$$

where ρ and A are the cantilever material density and cross-section area, respectively. The total potential energy of the AFM/sample system consists of the microcantilever elastic energy due to flexural deformations and the potential energy corresponding to the tip/sample interaction forces; that is, the van der Waals and DMT potential energies. The elastic potential energy, which is obtained based on the Euler-Bernoulli assumptions for small deflections, may be expressed as

$$V_e = \frac{1}{2}\int_0^l EI \left[\frac{\partial^2 w(x,t)}{\partial x^2}\right]^2 dx \tag{2.3}$$

with E and I being, respectively, the cantilever modulus of elasticity and second moment of area. The potential due to the tip/sample interaction is given upon integration of $V = -\int F(z)dz$ as follows:

$$V_{vdW} = -\frac{HR}{6[Z - w(l,t) - y(t)]} \qquad \text{for } z \geq a_0 \tag{2.4}$$

$$V_{DMT} = \frac{HR}{6a_0^2}[Z - w(l,t) - y(t)] + \frac{8}{15}E^*\sqrt{R}[a_0 - Z + w(l,t) + y(t)]^{5/2} \qquad \text{for } z < a_0 \tag{2.5}$$

We note that defining a potential function for the contact force, which is repulsive, has no physical justification and such a potential is introduced for mathematical purpose only. The total potential energy is the sum of the elastic potential energy and the potential energy due to the tip/sample interaction forces. Hence, the Lagrangian can be expressed as

$$L = T - V = \frac{1}{2}\int_0^l \rho A \left[\dot{w}(x,t) + \dot{y}(t)\right]^2 dx - \frac{1}{2}\int_0^l EI \left[\frac{\partial^2 w(x,t)}{\partial x^2}\right]^2 dx + \frac{HR}{6[Z - w(l,t) - y(t)]} \tag{2.6}$$

for the non-contact region $Z - w(l,t) - y(t) \geq a_0$ and

$$\begin{aligned} L = T - V =& \frac{1}{2}\int_0^l \rho A \left[\dot{w}(x,t) + \dot{y}(t)\right]^2 dx - \frac{1}{2}\int_0^l EI \left[\frac{\partial^2 w(x,t)}{\partial x^2}\right]^2 dx \\ & - \frac{HR}{6a_0^2}[Z - w(l,t) - y(t)] - \frac{8}{15}E^*\sqrt{R}[a_0 - Z + w(l,t) + y(t)]^{5/2} \end{aligned} \tag{2.7}$$

for the contact region $Z - w(l,t) - y(t) < a_0$. Finally, the energy dissipation function can be expressed as

$$D = \frac{1}{2}\int_0^l c \left[\dot{w}(x,t) + \dot{y}(t)\right]^2 dx \tag{2.8}$$

where c is the viscous damping coefficient per unit length of the microcantilever and obtained as [38]

$$c = \frac{\rho A \omega_k}{Q_k} \tag{2.9}$$

with ω_k and Q_k being the k-th natural frequency of the microcantilever and its corresponding quality factor. It is worth noting that the microcantilever internal energy losses also contribute to the quality factor, although these losses are usually negligible in comparison with the energy dissipation through the viscous damping mechanism due to the surrounding air.

The extended Hamilton principle is, next, employed to derive the equation of motion and associated boundary conditions; that is,

$$\int_{t_1}^{t_2}(\delta L+\delta W_e)dt=\int_{t_1}^{t_2}(\delta T-\delta V+\delta W_e)dt=0 \tag{2.10}$$

where W_e is the work done by the external forces on the system. We note that, according to the extended Hamilton principle, all variations vanish at t = t_1 and $t = t_2$. The energy dissipation due to viscous damping can be regarded as a negative work done by external forces.

Taking the first variation of the kinetic energy, Eq. (2.2), and using integration by parts yields

$$\int_{t_1}^{t_2}\delta T dt=-\int_{t_1}^{t_2}\int_0^l \rho A[\ddot{w}(x,t)+\ddot{y}(t)]\delta w dx dt \tag{2.11a}$$

Similarly, for the elastic potential energy, we take the first variation, use integration by parts, and obtain

$$\delta V_e=\int_0^l EI\frac{\partial^4 w(x,t)}{\partial x^4}\delta w dx-\frac{\partial}{\partial x}\left[EI\frac{\partial^2 w(x,t)}{\partial x^2}\right]_{x=l}\delta w_l+EI\frac{\partial^2 w(x,t)}{\partial x^2}|_{x=l}\frac{\partial}{\partial x}\delta(w_l) \tag{2.11b}$$

Variation of the work done by the external forces can be expressed as

$$\delta W_e=-\int_0^l c[\dot{w}(x,t)+\dot{y}(t)]\delta w dx \tag{2.11c}$$

And, finally, the first variations of the van der Waals and DMT potentials are given by

$$\delta V_{vdW}=-\frac{HR}{6[Z-w(l,t)-y(t)]^2}\delta w_l \qquad \text{for } z\geq a_0 \tag{2.11d}$$

$$\delta V_{DMT}=-\frac{HR}{6a_0^2}\delta w_l+\frac{4}{3}E^*\sqrt{R}[a_0-Z+w(l,t)+y(t)]^{3/2}\delta w_l \qquad \text{for } z<a_0 \tag{2.11e}$$

Substituting Eqs. (2.11a) through (2.11e) into Eq. (2.10), we find that the dynamics of the system is governed by

$$EIw^{iv}(x,t) + \rho A\ddot{w}(x,t) + c\dot{w}(x,t) = -\rho A\ddot{y}(t) - c\dot{y}(t) \tag{2.12}$$

subject to the boundary conditions

$$w(0,t) = 0, \quad w'(0,t) = 0, \quad w''(l,t) = 0 \tag{2.13}$$

and

$$EIw'''(l,t) = -\frac{HR}{6[Z - w(l,t) - y(t)]^2} \tag{2.14}$$

in the non-contact region and

$$EIw'''(l,t) = -\frac{HR}{6a_0^2} + \frac{4}{3}E^*\sqrt{R}[a_0 - Z + w(l,t) + y(t)]^{3/2} \tag{2.15}$$

in the contact region. We note that the nonlinear interaction forces appear in the boundary conditions and not in the partial-differential equation. Therefore, the initial-boundary-value problem presented by equations (2.12) through (2.15) is composed of a linear partial-differential equation, which is, respectively, fourth-order and second-order in the space and time variables, and four boundary conditions, one of them is not only nonlinear and time-dependent but also non-smooth function of the tip/sample separation gap and consequently time. Such a complicated initial-boundary-value problem does not seem to admit any exact analytical solutions. Approximate analytical solutions are, thus, employed to analyze the problem. It should be mentioned that the piecewise continuous shear boundary conditions given by (2.14) and (2.15) give rise to a non-smooth dynamics system, which requires special numerical treatment.

2.2 Point-Mass Model

The microcantilever/tip structure can be, alternatively, approximated by a point-mass spring, which is excited by an external force while the tip/sample interaction forces are also present. In this approach, the motion of the AFM microcantilever tip is assumed to be governed by a single nonlinear second-order differential equation of the form

$$m_{eq}\ddot{v}(t) + c_{eq}\dot{v}(t) + k_{eq}v(t) = F_{ext} + F_{eq}(v) \tag{2.16}$$

where $v(t) = w(l,t)$ denotes the tip deflection with respect to a non-inertial frame attached to the microcantilever base ($z = Z - v(t) - y(t)$). The parameters m_{eq}, k_{eq}, c_{eq}, F_{ext}, and $F_{eq}(v)$ are, respectively, the equivalent (effective) mass, the equivalent stiffness, the equivalent damping coefficient, the equivalent excitation force, and the equivalent tip/sample interaction force.

To determine the equivalent parameters of the point-mass model, such as the equivalent mass or the excitation amplitude, we need to discretize the partial-differential equation (2.12) and associated boundary conditions (2.13) through (2.15) based on a single-mode Galerkin approximation. To this end, we assume that the general solution of the initial-boundary-value problem can be approximated as

$$w(x,t) = \phi(x)q(t) \tag{2.17}$$

where $\phi(x)$ is the microcantilever first flexural mode shape and $q_n(t)$ is an unknown temporal function. It will be shown, later, that the natural frequencies and mode shapes of the

AFM microcantilever are very close to those of the free-end microcantilever with the same material and geometrical properties (i.e., where there is no shear force present at the end). Therefore, the first mode shape of the free-end microcantilever is utilized in equation (2-17) to approximate the nonlinear response of the AFM tip. Substituting Eq. (2.17) into Eqs. (2.6) through (2.8) and applying the Hamilton extended principle

$$\frac{d}{dt}\left(\frac{\partial L}{\partial \dot{q}}\right) - \frac{\partial L}{\partial q} = -\frac{\partial D}{\partial \dot{q}} \tag{2.18}$$

we obtain the following equation governing the microcantilever oscillations:

$$\ddot{q} + \frac{c}{\rho A}\dot{q} + \omega_1^2 q = -\frac{\int_0^l \phi dx}{\int_0^l \phi^2 dx}\ddot{y} - \frac{c}{\rho A}\frac{\int_0^l \phi dx}{\int_0^l \phi^2 dx}\dot{y} - \frac{\phi(l)}{\rho A \int_0^l \phi^2 dx}F(z) \tag{2.19}$$

The natural frequencies and mode shapes of a free-end microcantilever are, on the other hand, obtained by solving the following eigenvalue problem:

$$EIw^{iv}(x,t) + \rho A\ddot{w}(x,t) = 0 \tag{2.20}$$

$$w(0,t) = 0, \quad w'(0,t) = 0, \quad w''(l,t) = 0, \quad w'''(l,t) = 0 \tag{2.21}$$

Employing separation of variables, one can solve equations (2.20) and (2.21) and finds that the first mode shape of the microcantilever is given by

$$\phi(x) = \frac{\cos(\beta) + \cosh(\beta)}{\sin(\beta) + \sinh(\beta)}\Big[\sin(\frac{\beta}{l}x) - \sinh(\frac{\beta}{l}x)\Big] - \cos(\frac{\beta}{l}x) + \cosh(\frac{\beta}{l}x) \tag{2.22}$$

where β is the first positive real root of $1+\cos(\beta)\cosh(\beta) = 0$; that is, $\beta = 1.875$. Moreover, the first natural frequency of the microcantilever is given by

$$\omega_1^2 = \left(\frac{\beta}{l}\right)^4 \frac{EI}{\rho A} \tag{2.23}$$

It can be shown that

$$\int_0^l \phi^2 dx = l \tag{2.24a}$$

and

$$\phi(l) = 2 \tag{2.24b}$$

It can also be shown that

$$\int_0^l \phi(x) dx = \frac{2l}{\beta} \frac{\cos(\beta) + \cosh(\beta)}{\sin(\beta) + \sinh(\beta)} \tag{2.25a}$$

Substituting the first positive real root of the characteristic equation (i.e., $\beta = 1.875$) into Eq. (2.25a) results in

$$\int_0^l \phi(x) dx = 0.783l \tag{2.25b}$$

Multiplying both sides of equation (2.19) by $\phi(l)$ and using Eqs. (2.9), (2.24), and (2.25b), we obtain

$$\ddot{v}(t) + \frac{\omega_1}{Q_1}\dot{v}(t) + \omega_1^2 v(t) = \frac{F_{ext} + F_{eq}(v)}{m_{eq}} \tag{2.26}$$

where the equivalent forces are given by

$$F_{ext} = -1.566 m_{eq} \ddot{y} \tag{2.27a}$$

$$F_{eq}(v) = \begin{cases} \frac{HR}{6\left[Z - v(t) - y(t)\right]^2} & \text{for the non-contact region} \\ \frac{HR}{6a_0^2} - \frac{4E^*\sqrt{R}}{3}[a_0 - Z + v(t) + y(t)]^{3/2} & \text{for the contact region} \end{cases} \tag{2.27b}$$

and the equivalent mass is given by

$$m_{eq} = \frac{1}{4} m \tag{2.28}$$

with m and m_{eq} being, respectively, the total mass and equivalent mass of the AFM micro-cantilever.

Numerical simulations reveal that the damping term on the right-hand side of equation (2.19) does not have a significant effect on the AFM tip response and is, therefore, neglected in developing a simple point-mass model. Finally, comparing equation (2.16) and (2.26), we conclude that

$$c_{eq} = m_{eq}\frac{\omega_1}{Q_1} \tag{2.29}$$

and

$$k_{eq} = m_{eq}\omega_1^2 \tag{2.30}$$

Substitution of Eqs. (2.23) and (2.28) into Eq. (2.30) yields the equivalent stiffness as

$$k_{eq} = \frac{1.875^4}{4}\frac{EI}{l^3} = 3.09\frac{EI}{l^3} \tag{2.31}$$

The equivalent spring constant obtained based on the static deflection is, on the other hand, given by

$$k_s = 3\frac{EI}{l^3} \tag{2.32}$$

It is seen that the static stiffness k_s is very close to k_{eq} found based on the single-mode Galerkin discretization and, hence, can be used as the equivalent stiffness in the point-mass model. As it will be shown in numerical results, the point-mass model is not capable of accurately predicting all of the nonlinear phenomena exhibited by the AFM microcantilever and may fail to capture the grazing bifurcations occurring in the tapping mode AFM.

2.3 Static Deflection

The equations, which govern the static deflection $w^*(x)$ of the microcantilever, can be obtained from Eqs. (2.12)-(2.15) by dropping the time derivatives and the base excitation. The resulting problem is

$$w^{*iv}(x) = 0 \tag{2.33}$$

$$w^*(0) = 0, \quad w^{*'}(0) = 0, \quad w^{*''}(l) = 0 \tag{2.34}$$

$$EIw^{*'''}(l) = -\frac{HR}{6[Z - w^*(l)]^2} \tag{2.35}$$

in the non-contact region and

$$EIw^{*'''}(l) = -\frac{HR}{6a_0^2} + \frac{4}{3}E^*\sqrt{R}[a_0 - Z + w^*(l)]^{3/2} \tag{2.36}$$

in the contact region. The static problem can be easily solved upon integrating Eq. (2.33) and implementing the boundary conditions presented in (2.34). The result is

$$w^*(x) = \frac{1}{2}c_1\big(\frac{1}{3}x^3 - lx^2\big) \tag{2.37}$$

where c_1 is determined by implementing the boundary conditions given by Eqs. (2.35) and (2.36) and solving the resultant nonlinear algebraic equations. The tip deflection can, then, be found using equation (2.37). Alternatively, the tip deflection can be directly determined by solving the following nonlinear equations:

$$w^*(l) = \frac{HRl^3}{18EI[Z - w^*(l)]^2} \tag{2.38}$$

for the non-contact region and

$$w^*(l) = \frac{HRl^3}{18Ea_0^2} - \frac{4E^*l^3}{9EI}\sqrt{R}[a_0 - Z + w^*(l)]^{3/2} \tag{2.39}$$

for the contact region.

2.4 Free Vibrations of the AFM Microcantilever

Due to the nonlinear interaction forces arising between the AFM tip and the sample, the equations describing the microcantilever motion are highly nonlinear. Hence, to determine the free-vibration responses of the microcantilever, including the natural frequencies and mode shapes, we need to linearize the shear-force nonlinear boundary condition around the static equilibrium position. Thus, we let

$$w(x,t) = w^*(x) + v(x,t) \tag{2.40}$$

Substituting equation (2.40) into equations (2.12)-(2.15) and dropping the damping and excitation terms, we obtain the following equations:

$$EIv^{iv}(x,t) + EIw^{*iv}(x) + \rho A\ddot{v}(x,t) = 0 \tag{2.41}$$

$$v(0,t) + w^*(0) = 0, \quad v'(0,t) + w'^*(0) = 0, \quad v''(l,t) + w''^*(l) = 0 \tag{2.42}$$

$$v'''(l,t) + w'''^*(l) = -\frac{HR}{6EI[Z - w^*(l) - v(l,t)]^2} \qquad \text{if } Z - w^*(l) - v(l,t) \geq a_0 \tag{2.43}$$

$$v'''(l,t) + w'''^*(l) = -\frac{HR}{6EIa_0^2} + \frac{4E^*\sqrt{R}}{3EI}[a_0 - Z + w^*(l) + v(l,t)]^{3/2} \qquad \text{if } Z - w^*(l) - v(l,t) < a_0 \tag{2.44}$$

Using equations (2.33)-(2.36) and linearizing the outcome for small $v(x,t)$, we obtain the following eigenvalue problem:

$$EIv^{iv}(x,t) + \rho A\ddot{v}(x,t) = 0 \tag{2.45}$$

$$v(0,t)=0,\quad v'(0,t)=0,\quad v''(l,t)=0 \tag{2.46}$$

$$v'''(l,t)=-\frac{HR}{3EI[Z-w^*(l)]^3}v(l,t)\qquad \text{if } Z-w^*(l)-v(l,t)\geq a_0 \tag{2.47}$$

$$v'''(l,t)=\frac{2E^*\sqrt{R}}{EI}[a_0-Z+w^*(l)]^{1/2}v(l,t)\qquad \text{if } Z-w^*(l)-v(l,t)< a_0 \tag{2.48}$$

Using separation of variables to solve equations (2.45)-(2.48), we obtain the mode shapes

$$\phi_n(x)=\gamma_n\Big\{\frac{\cos(\beta_n)+\cosh(\beta_n)}{\sin(\beta_n)+\sinh(\beta_n)}\Big[\sin(\frac{\beta_n}{l}x)-\sinh(\frac{\beta_n}{l}x)\Big]-\cos(\frac{\beta_n}{l}x)+\cosh(\frac{\beta_n}{l}x)\Big\} \tag{2.49}$$

and the natural frequencies

$$\omega_n=\frac{\beta_n^2}{l^2}\sqrt{\frac{EI}{\rho A}} \tag{2.50}$$

where the β_n are the roots of

$$\beta_n^3\big[1+\cos(\beta_n)\cosh(\beta_n)\big]=\alpha\big[\cosh(\beta_n)\sin(\beta_n)-\cos(\beta_n)\sinh(\beta_n)\big] \tag{2.51}$$

and

$$\alpha=\begin{cases}\frac{HR}{3EI[Z-w^*(l)]^3} & \text{for the non-contact region}\\ -\frac{2E^*\sqrt{R}}{EI}[a_0-Z+w^*(l)]^{1/2} & \text{for the contact region}\end{cases} \tag{2.52}$$

These mode shapes are orthogonal and the γ_n are chosen so that they are orthonormal; that is,

$$\int_0^l \phi_n(x)\phi_m(x)dx=\delta_{mn} \tag{2.53}$$

where δ_{mn} is the Kronicker delta defined by

$$\delta_{mn}=\begin{cases}0 & \text{if } m\neq n,\\ 1 & \text{if } m=n.\end{cases}$$

Chapter 3

Nonlinear Dynamics of the AFM Microcantilever in the Monostable Phase

A multimode Galerkin approximation is used to discretize the partial-differential equation of motion and associated boundary conditions governing the cantilever response and obtain a set of nonlinearly coupled ordinary-differential equations governing the time evolution of the system dynamics. A comprehensive numerical analysis is, then, performed for a wide range of the excitation amplitude and frequency. The tip oscillations are examined using nonlinear dynamic tools, such as phase portraits and Poincaré maps, through several examples. The AFM tip is assumed to be located in the monostable portion of the static bifurcation diagram

in all numerical examples throughout this chapter.

3.1 Multimode Galerkin Discretization

Nonlinear dynamics of continuous systems, such as beams and plates, are, in principle, governed by spatial-temporal partial-differential equations. Since exact solutions are generally not available for this class of initial-boundary-value problems, reduced-order techniques are used to transform the partial-differential equations and associated boundary conditions into a set of ordinary-differential equations. One of the most popular reduced-order methods, which has been extensively used to investigate nonlinear oscillations of continuous systems, is the Galerkin procedure, in which, the spatial variation is represented using the linear mode shapes of the vibrations. As a result of the Galerkin procedure, a set of nonlinear coupled second-order ordinary-differential equations is obtained governing the temporal behavior of the system. In theory, the spatial variation may be approximated by functions other than the linear mode shapes of the system, but using the mode shapes would make the algebra much simpler due to the orthogonality of the mode shapes, the number of equations in the reduced-order model is smaller, and the results are more convenient for physical interpretation. In a sense, the contribution of each mode to the response can be examined.

We use the Galerkin procedure to reduce the partial-differential equation and associated boundary conditions given by Eqs. (2.12) through (2.15) into a set of nonlinear ODEs. To

this end, we assume that

$$w(x,t) = \sum_{n=1}^{N} \phi_n(x) q_n(t) \tag{3.1}$$

where ϕ_n is the microcantilever n-th flexural mode shape and the q_n are unknown temporal functions. Also, N indicates the number of modes participating in the response. Substituting equation (3.1) into equations (2.6)-(2.8), we obtain the following Lagrangian and energy dissipation function in discretized forms:

$$\begin{aligned} L = \frac{1}{2}\int_0^l \rho A \left[\sum_{n=1}^{N} \phi_n(x)\ddot{q}_n(t) + \ddot{y}(t)\right]^2 dx - \frac{1}{2}\int_0^l EI \left[\sum_{n=1}^{N} \phi_n''(x) q_n(t)\right]^2 dx \\ + \frac{HR}{6[Z - \sum_{n=1}^{N} \phi_n(l) q_n(t) - y(t)]} \end{aligned} \tag{3.2}$$

for the non-contact region and

$$\begin{aligned} L = \frac{1}{2}\int_0^l \rho A \left[\sum_{n=1}^{N} \phi_n(x)\ddot{q}_n(t) + \ddot{y}(t)\right]^2 dx - \frac{1}{2}\int_0^l EI \left[\sum_{n=1}^{N} \phi_n''(x) q_n(t)\right]^2 dx \\ - \frac{HR}{6a_0^2}\big[Z - \sum_{n=1}^{N} \phi_n(l) q_n(t) - y(t)\big] - \frac{8}{15} E^* \sqrt{R}\big[a_0 - Z + \sum_{n=1}^{N} \phi_n(l) q_n(t) + y(t)\big]^{5/2} \end{aligned} \tag{3.3}$$

for the contact region. The energy dissipation function is written as

$$D = \frac{1}{2}\int_0^l c \left[\sum_{n=1}^{N} \phi_n(l)\dot{q}_n(t) + \dot{y}(t)\right]^2 dx \tag{3.4}$$

Now, we apply the extended Hamilton principle

$$\frac{d}{dt}\left(\frac{\partial L}{\partial \dot{q}_n}\right) - \frac{\partial L}{\partial q_n} = -\frac{\partial D}{\partial \dot{q}_n} \qquad n = 1, 2, \ldots, N \tag{3.5}$$

and the orthonormality condition to obtain the discretized equations

$$\ddot{q}_n + c_n\dot{q}_n + \omega_n^2 q_n - \frac{EI\phi_n(l)}{\rho A}\sum_{m=1}^{N} \phi_m'''(l) q_m + f_n(q_1, q_2, \ldots, q_N) = -\int_0^l \phi_n(x)dx(\ddot{y} + c_n\dot{y}) \tag{3.6}$$

where $c_n = c/(\rho A) = \frac{w_n}{Q_n}$, modal damping was assumed, and

$$f_n = \begin{cases} -\frac{HR\phi_n(l)}{6\rho A\left[Z - y(t) - \sum_{m=1}^{N}\phi_m(l)q_m(t)\right]^2} & \text{for the non-contact region} \\ -\frac{HR\phi_n(l)}{6\rho A a_0^2} + \frac{4E^*\sqrt{R}\phi_n(l)}{3\rho A}[a_0 - Z + y(t) + \sum_{m=1}^{N}\phi_m(l)q_m(t)]^{3/2} & \text{for the contact region} \end{cases} \tag{3.7}$$

We introduce, for the sake of convenience, the following nondimensional variables (denoted by bars):

$$\bar{t} = t\omega_1, \quad \bar{Z} = \frac{Z}{Z^*}, \quad \bar{a}_0 = \frac{a_0}{Z^*}, \quad \bar{Y} = \frac{Y}{Z^*}, \quad \bar{q}_n = \frac{\phi_n(l)q_n}{Z^*}, \quad \bar{\Omega} = \frac{\Omega}{\omega_1} \tag{3.8}$$

where Z^* is the equilibrium tip/sample separation distance; that is, $Z^* = Z - w^*(l)$. Substituting Eq. (3.8) into Eqs. (3.6) and (3.7) yields the following nondimensional form of the discretized equations;

$$\begin{aligned} \frac{d^2\bar{q}_n}{d\bar{t}^2} + \frac{1}{Q}\frac{d\bar{q}_n}{d\bar{t}} + \frac{\omega_n^2}{\omega_1^2}\bar{q}_n - \frac{EI\phi_n(l)}{\rho A\omega_1^2}\sum_{m=1}^{N}\phi_m'''(l)\bar{q}_m + \bar{f}_n(\bar{q}_1, \bar{q}_2, \ldots, \bar{q}_N) \\ = -\phi_n(l)\int_0^l \phi_n(x)dx\left[\frac{d^2\bar{y}}{d\bar{t}^2} + \frac{1}{Q}\frac{d\bar{y}}{d\bar{t}}\right] \end{aligned} \tag{3.9}$$

and

$$\bar{f}_n = \begin{cases} -\frac{HR\phi_n^2(l)}{6\rho A\omega_1^2 Z^{*3}\left[\bar{Z} - \bar{y}(t) - \sum_{m=1}^{N}\phi_m(l)\bar{q}_m(t)\right]^2} & \text{for the non-contact region} \\ -\frac{HR\phi_n^2(l)}{6\rho A\omega_1^2\bar{a}_0^2 Z^{*3}} + \frac{4E^*\sqrt{RZ^*}\phi_n^2(l)}{3\rho A\omega_1^2}\left[\bar{a}_0 - \bar{Z} + \bar{y}(\bar{t}) + \sum_{m=1}^{N}\phi_m(l)\bar{q}_m(\bar{t})\right]^{3/2} & \text{for the contact region} \end{cases} \tag{3.10}$$

where

$$\bar{y}(\bar{t}) = \bar{Y}\sin(\bar{\Omega}\bar{t}) \tag{3.11}$$

Throughout this chapter, we perform numerical simulations using the data given for the

Table 3.1: Parameters and properties of the AFM

Tip radius R	10 nm
Length l	250 μm
Cross-section area A	8.09 $e^{-11}m^2$
Second moment of area I	3.57 $e^{-23}m^4$
Density ρ	2300 kg/m^3
Modulus of elasticity E	130 GPa
Effective modulus of elasticity E^*	10.2 GPa
Quality factor in air Q	33.3
Hamaker constant H	2.96 $e^{-19}J$
Intermolecular distance a_0	0.38 nm

AFM in Ref. [28] and listed in Table 3.1. We note that although all numerical simulations throughout this chapter have been performed for a certain AFM parameters, the methodology developed here can be applied to any different AFM. However, depending on AFM geometric and material properties and operational parameters different results might be observed for different AFM probes. We begin with the tip/sample interaction force and plot variation of the interaction force with the instantaneous tip/sample gap in Fig. 3.1. As observed in the figure, when the tip is far from the sample, the interaction force approaches zero, but, as it comes down close to the contact point (i.e., $z = a_0$), the interaction force decreases sharply and reaches its minimum at $z = a_0$. We note that the only force present

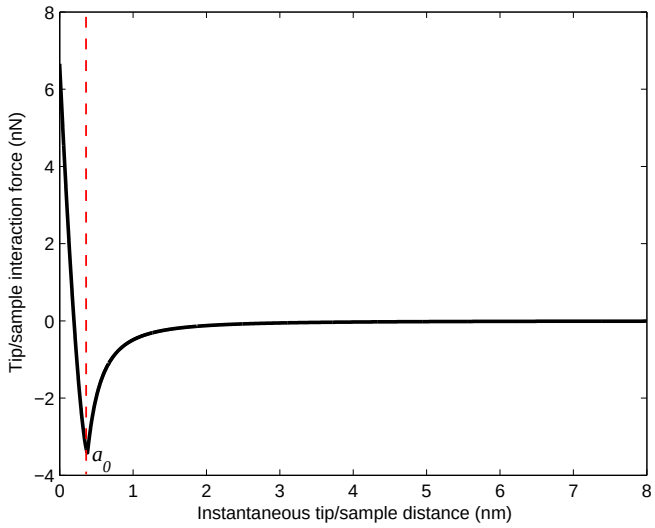

Figure 3.1: Variation of the tip/sample interaction force with the instantaneous tip/sample separation distance.

in this region, which is called the non-contact region, is the attractive van der Waals force. When the tip touches the sample and enters the contact region, the interaction force increases with a very high gradient. The interaction force is, initially, negative in the contact region due to the dominant van der Waals force, but, as the tip penetrates the sample, the interaction force changes sign and becomes positive due to the strong repulsive force arising between the tip and the sample during contact. We also note that the interaction force is, although continuous at point $z = a_0$, it is not differentiable at this point. Therefore, the corresponding dynamical system is regarded as a non-smooth dynamical system. Numerical solutions of such a dynamical system are costly and require special computational schemes, which are discussed later.

3.2 Static Deflection

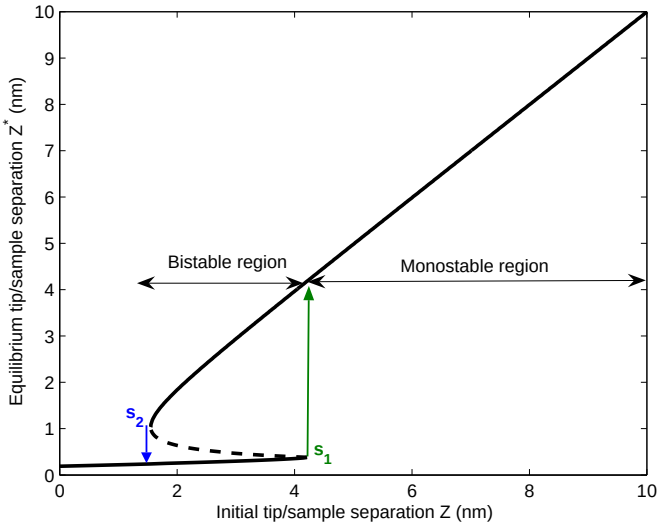

Figure 3.2: Variation of the tip and static deflection with the initial tip/sample separation.

The next step is to solve Eqs. (2.38) and (2.39) for the AFM parameters listed in Table 3.1. We solve these equations numerically to obtain the static deflection of the microcantilever. Variation of the equilibrium tip/sample separation distance Z^* with the initial tip/sample separation distance Z is shown in Figure 3.2a. These results are in perfect agreement with those of Lee et al. [28]. There are three branches: two are stable and one is unstable. The stable branches are connected with the unstable branch by two saddle-node bifurcation points s_1 and s_2. The lower stable branch represents contact deflections, whereas the upper branch represents non-contact deflections. Starting with an initial tip/sample separation Z below s_2 and increasing it, one finds that the static deflection will be in the contact region until s_1 is exceeded. As a result, the static deflection undergoes a saddle-node bifurcation, resulting

in a jump up to the upper branch (non-contact region). On the other hand, starting from a $Z > s_1$ and decreasing it, one finds that the static deflection follows the upper branch (non-contact state) until Z decreases below s_1 where the static deflection undergoes a saddle-node bifurcation, resulting in a jump down to the lower branch (contact state). In the interval $[s_1,s_2]$, there are two stable deflections: one in the contact state and one in the non-contact state. Therefore, three distinct regions are distinguished in the static bifurcation curve: two monostable regions and a bistable region. One of the monostable regions is far from the sample (i.e., $Z > s_1$) and the other one is very close to sample in the contact region (i.e., $Z < s_2$). For the monostable region in the contact state, the AFM tip is, effectively, stuck to the sample and, therefore, not of practical interest. Consequently, we devote our attention to the monostable phase far from the sample and the bistable phase throughout this dissertation.

We point out here that the stability of the static solution is determined based on the Lagrange-Dirichlet stability theorem. According to this theorem, stability is determined by the sign of the second variation of the total potential energy function; that is, the sum of the microcantilever elastic potential energy and the potential energy due to the tip/sample interaction forces. To this end, we drop the external excitation in Eqs. (2.3)-(2.5) and add them up to find the following total potential function:

$$V = \frac{1}{2}\int_0^l EIw''^2(x)dx - \frac{HR}{6[Z - w(l)]} \tag{3.12}$$

for the non-contact region and

$$V = \frac{1}{2}\int_0^l EIw''^2(x)dx + \frac{HR}{6a_0^2}[Z - w(l)] + \frac{8}{15}E^*\sqrt{R}[a_0 - Z + w(l)]^{5/2} \tag{3.13}$$

for the contact region. The second variation of the total potential function given by Eqs. (3.12) and (3.13) is evaluated at the static equilibrium solution $\big($i.e., $w(x) = w^*(x)\big)$ to determine its stability. If the result is positive, the equilibrium solution is stable, and if it is negative, the equilibrium is unstable.

We note that the static curves displayed in Fig. 3.2 can be, alternatively, generated by treating Z^* as a known parameter and solving the algebraic system for Z. To this end, we rewrite Eqs. (2.38) and (2.39) in the following forms:

$$Z - Z^* = \frac{HRl^3}{18EIz^{*2}} \tag{3.14}$$

for the non-contact region and

$$Z - Z^* = \frac{HRl^3}{18EIa_0^{*2}} - \frac{4E^*l^3}{9EI}\sqrt{R}\big[a_0 - Z^*\big]^{3/2} \tag{3.15}$$

for the contact region. This way the nonlinear system of algebraic equations is reduced to a linear system in terms of Z, which is computationally less expensive and much easier to solve than the original nonlinear system.

We note that the Galerkin procedure can be, also, used to compute the static deflection of the AFM microcantilever. Starting with Eqs. (3.6) and (3.7) and dropping the time derivative, the external excitation, and the damping term results in the static equilibrium

equations based on a multimode Galerkin discretization. The result is

$$q_n - \frac{EI\phi_n(l)}{\rho A\omega_n^2}\sum_{m=1}^{N}\phi_m'''(l)q_m + g_n(q_1, q_2, \ldots, q_N) = 0 \tag{3.16}$$

and

$$g_n = \begin{cases} -\frac{HR\phi_n(l)}{6\rho A\omega_n^2\left[Z-\sum_{m=1}^{N}\phi_m(l)q_m\right]^2} & \text{for the non-contact region} \\ -\frac{HR\phi_n(l)}{6\rho A\omega_n^2 a_0^2} + \frac{4E^*\sqrt{R}\phi_n(l)}{3\rho A\omega_n^2}\left[a_0 - Z + \sum_{m=1}^{N}\phi_m(l)q_m\right]^{3/2} & \text{for the contact region} \end{cases} \tag{3.17}$$

Solving the system of nonlinear algebraic equations (3.16) and (3.17), we obtain approximations to the static deflection curves. Numerical studies performed using different number of mode shapes in the Galerkin procedure indicates that only one mode shape is sufficient to recover the non-contact portion of the static deflection curve found based on the analytical solution of the original Euler-Bernoulli beam equation. However, at least six mode shapes are required to recover the contact portion of the static deflection curve. These results imply that including six mode shapes, for the case when the tip is initially located in the contact region, is, although necessary, might not be adequate in the dynamics case. Similarly, when the tip lies in the non-contact region in the reference configuration, a single-mode Galerkin discretization might not be enough to analyze the dynamics of the AFM microcantilever. In the other word, the static analysis based on the Galerkin procedure only provides the minimum number of mode shapes required for the dynamic analysis.

3.3 Parametric Study of The Static Deflection Curve

To generalize the discussion made in the previous section and examine the effect of various geometrical and material parameters on the AFM microcantilever static deflection curve, we conduct a parametric investigation on the static bifurcation diagram. To this end, equations (3.14) and (3.15) are rewritten in a nondimensional form by using a_0 as the characteristic length:

$$\begin{cases} \bar{Z} = \bar{Z}^* + \frac{\alpha_1}{\bar{Z}^{*2}} & \bar{Z}^* \geq 1 \\ \bar{Z} = \bar{Z}^* + \alpha_1 - \alpha_2(1-\bar{Z}^*)^{3/2} & \bar{Z}^* < 1 \end{cases}$$

where

$$\bar{Z} = \frac{Z}{a_0}, \quad \bar{Z}^* = \frac{Z^*}{a_0}, \quad \alpha_1 = \frac{HRl^3}{18EIa_0^3}, \quad \alpha_2 = \frac{4E^*L^3\sqrt{Ra_0}}{9EI}$$

We note that Eq. (3.18) indicates that the nondimensional tip deflection depends only on two nondimensional parameters α_1 and α_2. We also note that for the AFM properties listed in Table 3.1, these nondimensional parameters are obtained as $\alpha_1 = 10.0897$ and $\alpha_2 = 29.7521$. Effects of the variations of α_1 and α_2 on the tip static deflection curves are studied by generating static deflection curves for different values of α_1 and α_2. To cover all the possible values that α_1 and α_2 can mathematically admit, we first start with a small α_1 and fix it at $\alpha_1 = 0.01$ and generate the static deflection curves for several values of α_2. Then we fix α_1 at a large value, say $\alpha_1 = 1000$, and plot the static deflection curves for various values of α_2. Finally, we repeat the same procedure by keeping α_2 fixed and changing α_1. This way, the impact of all mathematically possible values of α_1 and α_2 on the tip static behavior are examined (both α_1 and α_2 are positive by definition). We note that some of these values

might be physically impractical and never occur in a real AFM. Figure 3.4 displays static bifurcation curves for $\alpha_1 \ll 1$ and different values of α_2. As observed in the figure, for small values of α_1, static deflection curves consist of two stable branches: a non-contact branch and a contact branch. No bistable region is detected for this case. The static bifurcation diagrams are, on the other hand, depicted in Figure 3.4, for $\alpha_1 \gg 1$ and several values of α_2. For the all values of α_2 used to generates the bifurcation curves, three different branches are detected: A stable contact branch, an unstable non-contact branch and a stable non-contact branch. For a small range of the nondimensional initial tip/sample separation gap, a stable contact and non-contact branches coexist and therefore the bifurcation curves are divided to distinct monostable and bistable regions. We note that the contact branch is very close to the sample and therefore it is not of a practical interest. Similarly, we present the static deflection curves in Figure 3.5 for $\alpha_2 \ll 1$ and several values of α_1. As seen in the figure, monostable and bistable regions are distinguished for different values of α_1 and the width of the bistable region increases by increasing value of α_1. Finally, Figure 3.6 illustrates the variations of the nondimensional equilibrium tip/sample gap with the nondimensional initial tip/sample gap for $\alpha_2 \gg 1$ and different values of α_1. Again, bistable and monostable regions are detected for this case. In general, we may conclude that depending on the AFM geometrical and material properties, different behaviors are observed in static bifurcation diagrams. Although for most cases both monostable and bistable regions are present in the bifurcation curve, there are values of α_1 and α_2 for which no bistable region is detected. However, for the real AFM probes used in the present investigation, distinct monostable and

bistable regions are detectable. We also note that the present parametric study has been developed to explore possibility of different behaviors which could be exhibited by the AFM tip in the static mode and some cases detected here mathematically might never happen in reality due to the impractical values of nondimensional parameters α_1 and α_2. It can be shown that for $\alpha_1 \geq \frac{1}{2}$ and arbitrary α_2, static bifurcation diagram consists of two distinct bistable and monostable regions. We note that to have a bistable region the non-contact branch corresponding to $\bar{Z} = \bar{Z}^* + \frac{\alpha_1}{\bar{Z}^{*2}}, \quad \bar{Z}^* \geq 1$ must have a local minimum. To find the local minimum, we differentiate with respect to $\bar{Z}^*$:

$$\frac{d\bar{Z}}{d\bar{Z}^*} = 1 - \frac{2\alpha}{\bar{Z}^*} \qquad \bar{Z}^* \geq 1 \tag{3.18}$$

Setting $\frac{d\bar{Z}}{d\bar{Z}^*}$ equal zero and using condition $\bar{Z}^* \geq 1$, we conclude that $\alpha_1 \geq \frac{1}{2}$. Therefor, the necessary condition to have a bistable region in the static deflection diagram is to have $\alpha_1 \geq \frac{1}{2}$. Otherwise, no bistable region is detected in the tip static deflection curve (See Fig. 3.3). This mathematical observation is in complete agreement with numerical simulations performed for different values of α_1 and α_2 and presented by figures 3.3 through 3.6. We note that for values of α_1 and α_2 close to those corresponding to the AFM properties listed in Table 3.1 (i.e.,$\alpha_1 = 10.0897$ and $\alpha_2 = 29.7521$), no significant change is observed and very similar curves are obtained for the tip static deflection.

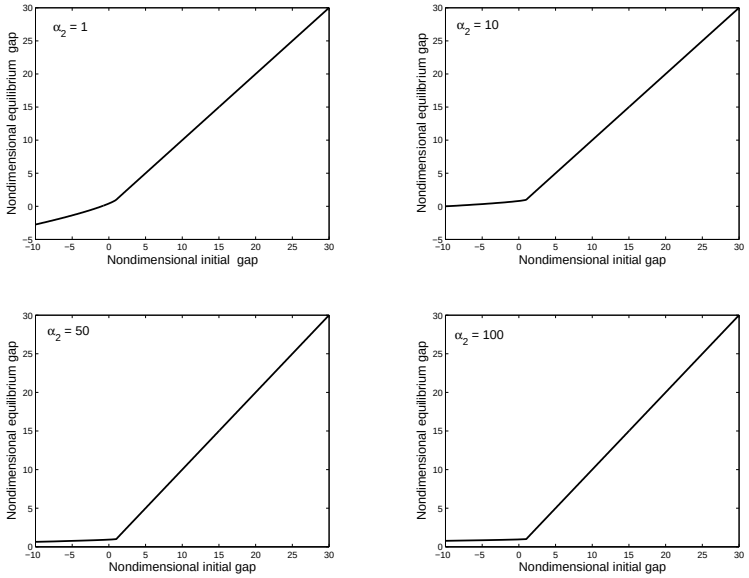

Figure 3.3: Static bifurcation diagrams for $\alpha_1 = 0.01$ and different values of α_2 .

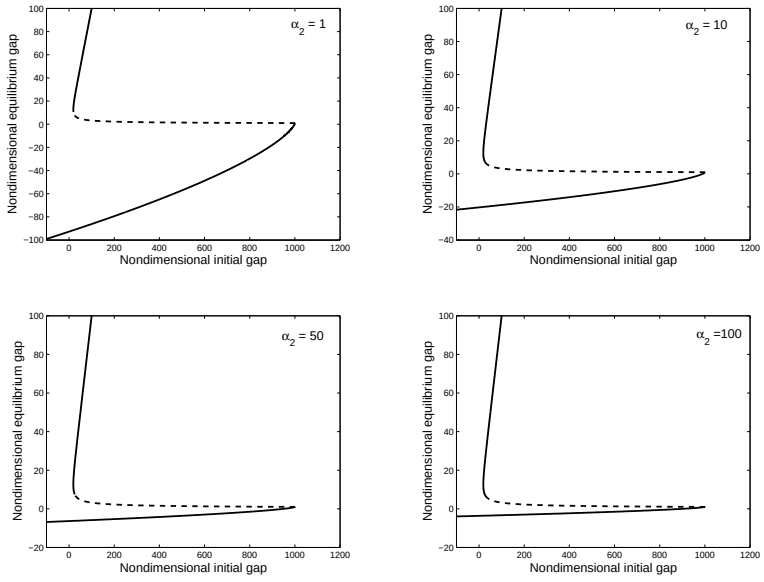

Figure 3.4: Static bifurcation diagrams for $\alpha_1 = 1000$ and different values of α_2 .

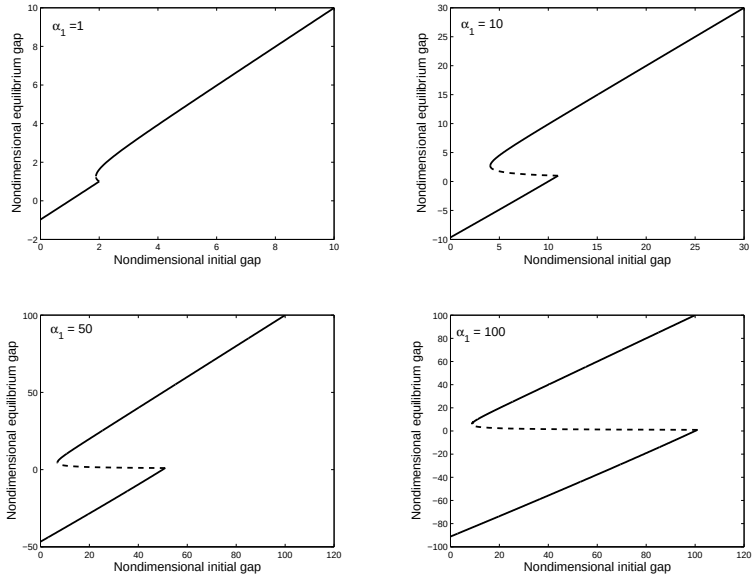

Figure 3.5: Static bifurcation diagrams for $\alpha_2 = 0.01$ and different values of α_1 .

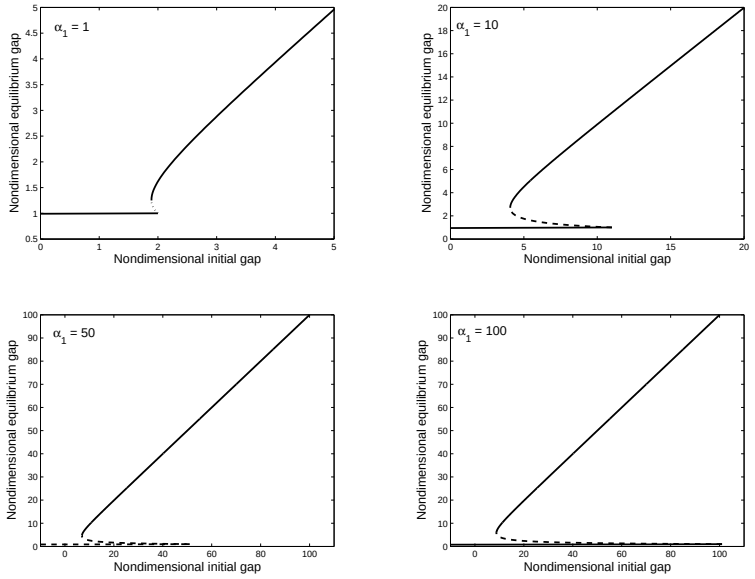

Figure 3.6: Static bifurcation diagrams for $\alpha_2 = 1000$ and different values of α_1 .

3.4 Natural Frequencies and Mode Shapes

Since the mode shapes of the microcantilever about the static equilibrium are used as basis functions in the Galerkin procedure, we need to compute the natural frequencies and mode shapes around the chosen static deflection. The natural frequencies of the AFM microcantilever are determined by numerically integrating Eq. (2.51). We focus in this chapter on investigating the AFM dynamics in the monostable phase; the monostable region in the static bifurcation diagram starts from $s_1 = 4.214$ nm according to Figure 3.2. Therefore, we picked $Z = 5$ nm and $Z = 60$ nm and compared the natural frequencies with those obtained for a free cantilever beam, see Eq. (2.23). The results are presented in Table 3.2. Clearly, the fourth and higher natural frequencies agree with those of the free cantilever to six significant figures and the third natural frequency agrees with that of the free cantilever to five significant figures. The difference in the first natural frequency is about 0.44 %, whereas the difference in the second natural frequency is about 0.01 %. Moreover, there is a little difference between the mode shapes and those of a free cantilever, as shown in Figure 3.7, and hence one can use the mode shapes of a free cantilever in the Galerkin procedure.

To get more insight into the free vibrations of the AFM microcantilever, we delineate variation of the first natural frequency of the microcantilever with the initial tip/sample separation distance Z in Fig. 3.8a. Except for a small range of the initial tip/sample separation distance, which is close to the border with the bistable region, the first natural frequency of the AFM microcantilever is very close to that of a free-end microcantilever. Close examination

Table 3.2: Comparison of the natural frequencies of the AFM with those of a cantilever beam

Z	f_1 (kHz)	f_2 (kHz)	f_3 (kHz)	f_4 (kHz)	f_5 (kHz)	f_6 (kHz)	f_7 (kHz)	f_8 (kHz)
5 nm	44.5202	280.196	784.634	1537.59	2541.75	3796.93	5303.15	7060.41
60 nm	44.7154	280.228	784.645	1537.59	2541.75	3796.93	5303.15	7060.41
free	44.7155	280.228	784.645	1537.59	2541.75	3796.93	5303.15	7060.41

of the figure reveals that, even for the border point $s_1 = 4.214$ nm in which the largest difference is seen, the difference between the fundamental frequencies of the AFM and free-end microcantilevers is less than 1 %. In addition, Figure 3.8 clearly demonstrates that, when the AFM tip is initially located far from the sample in the non-contact monostable region, one can safely assume that the AFM and free-end microcantilevers have identical natural frequencies. This range of the initial tip/sample separation gap is, in fact, the common range for most practical purposes. Similarly, variation of the second natural frequency of the AFM microcantilever with the tip/sample gap in the reference configuration is depicted in Fig. 3.8b. The same trend is observed for the second natural frequency and the difference between the second natural frequencies of the AFM and free-end microcantilevers is even smaller than that of the first natural frequencies. We also note that, as far as the AFM operates in the monostable phase, decreasing the initial tip/sample separation gap leads to a slight softening of the microcantilever due to the van der Waals attractive force.

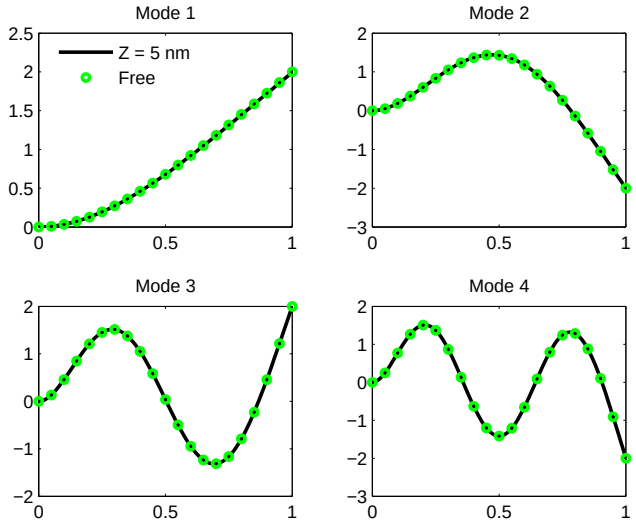

Figure 3.7: Comparison of the first four mode shapes with those of a free cantilever.

3.5 Nonlinear Dynamics

Depending on whether the tip static deflection is located in the monostable or bistable region, the AFM is expected to exhibit totally different dynamical behavior under base excitation. However, in most practical applications, the operational regime for tapping mode microscopy is in the monostable non-contact region and, hence, the present chapter is limited to equilibrium tip/sample separations located on the mono-stable upper branch [28]. More specifically, Z is assumed to be 60 nm for all numerical calculations performed in this chapter, unless otherwise mentioned. In addition, the quality factor is assumed to be constant $Q = 33.3$.

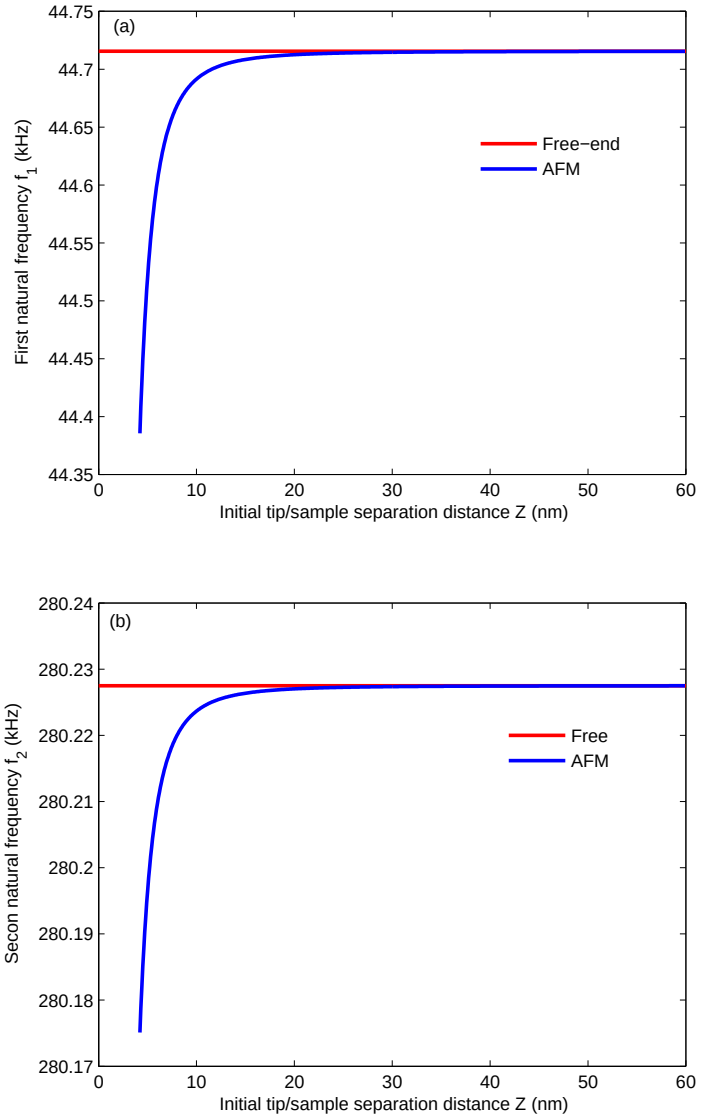

Figure 3.8: Variation of the (a) first and (b) second natural frequencies of the AFM micro-cantilever with the initial tip/sample separation distance.

3.5.1 Numerical Scheme

We solve the nondimensional discretized equations (3.9) and (3.10) using numerical integration techniques. We note that the dynamics of the AFM, including the discretized equations, is a non-smooth dynamical system with time-dependent coefficients and strong nonlinearities, which causes numerical complications and requires rigorous numerical schemes. We also note that no simplifications are made regarding the non-smooth interaction forces and they are considered as appearing in Eqs. (3.9) and (3.10) in all numerical simulations. A variety of numerical integration schemes may be employed to solve initial-value problems of ordinary-differential equations (ODE). The first step is to reformulate the initial-value problem and present it as a system of first-order ODEs

$$\frac{dy}{dt} = f(t, y) \qquad for \quad t > t_0$$

with the initial condition

$$y(t_0) = y_0$$

where t is the independent variable, $y(t)$ is the unknown function of t, $y_0(t)$ is the given initial condition, and $f(t, y)$ is a given function of time describing the differential equation. We note that the above equation is, in principle, a vector equation with finite dimensions. In all numerical solutions, the temporal variable t is discretized, say $t_j, j = 1, 2, \ldots, N$, and then the values of the unknown function y are determined at the t_j; that is $y_j = y(t_j), j = 1, 2, \ldots, N$.

Numerical solutions of the initial-value problems are classified as one-step and multi-step methods. In one-step methods, such as Runge-Kutta methods, the numerical value of the

unknown function at each step is calculated using the calculated value at the previous step only (i.e., y_{j-1} is not involved in the calculation of y_{j+1}). The simplest one-step method is Euler's method in which one keeps only the first two terms in the Taylor series expansion

$$y_{j+1} = y_j + hf(t_j, y_j)$$

where h is the time step. Keeping higher-order terms in the Taylor series, one achieves a more accurate numerical solution. However, a higher-order one-step method requires more evaluations of the function f. For example, the Euler method requires only one evaluation of the function f, whereas the fourth-order Runge-kutta method requires four evaluations of f in each step; that is,

$$k_1 = f(t_j, y_j)$$

$$k_2 = f(t_j + \frac{h}{2}, y_j + \frac{h}{2}k_1)$$

$$k_3 = f(t_j + \frac{h}{2}, y_j + \frac{h}{2}k_2)$$

$$k_4 = f(t_j + h, y_j + hk_3)$$

$$y_{j+1} = y_j + \frac{h}{6}(k_1 + 2k_2 + 2k_3 + k_4)$$

For some problems, computation of a precise numerical solution using one-step methods can be numerically expensive and ineffective. Therefore, it is desirable to have a higher-order method that requires only one evaluation in each step. This is not possible in one-step methods. Multi-step methods, however, involve only one calculation in each step but require information from previous steps. Therefore, the main advantage of multi-step methods over one-step methods is that they are more efficient, however, they are more difficult to program.

The Adams-Bashforth methods are the most widely used explicit multi-step methods. In the four-step Adams-Bashforth method, for example, values of f from four previous steps are utilized to calculate the numerical value of f at the present step; that is,

$$y_{j+1} = y_j + h\left[\frac{55}{24}f_j - \frac{59}{24}f_{j-1} + \frac{37}{24}f_{j-2} - \frac{9}{24}f_{j-3}\right]$$

with $f_j = f(t_j, y_j)$.

All of the aforementioned methods are categorized as explicit methods. They calculate the value of the unknown function at a later time step using its values at the current and previous time steps. Implicit methods, on the other hand, compute the value of the unknown function at a later time step by solving an equation involving the current values of the function at the present, previous, and later time steps. Implicit methods may be one-step in which only values of the function at the present and a later time step appear in the equation or multi-step in which the function values at the previous time steps as well are included. It is obvious that implicit methods require extra computation to solve the algebraic equations at each step and they might be much harder to implement. However, implicit methods are very useful for solving what so-called stiff ODEs for which explicit methods require impractically small time steps to keep the solution error bounded. Otherwise, the computational error may grow very fast and lead to inaccurate and unreliable results. We use the four-step Adams-Moulton method, which is an implicit multi-step method in the present research; that is,

$$y_{j+1} = y_j + h\left[\frac{251}{720}f_{j+1} + \frac{646}{720}f_j - \frac{264}{24}f_{j-1} + \frac{106}{720}f_{j-2} - \frac{19}{720}f_{j-3}\right]$$

A Fortran code was developed for numerical solution of Eqs. (3.9) and (3.10), based on the

four-step Adams-Moulton method using an adaptive procedure. In adaptive methods, the time step size is not fixed and selected automatically. An event-driven scheme [62] was also included to detect and locate the time of the next non-smooth event; that is, physically, touching or detaching the sample.

3.5.2 Point-Mass Model

The equivalent point-mass model of a continuous cantilever/tip structure subjected to a harmonic base excitation was developed in Chapter 2. Using the same nondimensional variables, as introduced in Eq. (3.8), along with $\bar{v} = \frac{v}{Z^*}$, we rewrite the nonlinear ordinary-differential equation (2.26) in the following nondimensional form:

$$\frac{d^2\bar{v}}{d\bar{t}^2} + \frac{1}{Q_1}\frac{d\bar{v}}{d\bar{t}} + \bar{v} = 1.566\bar{\Omega}^2\bar{y}(\bar{t}) + \bar{f}(\bar{v}) \tag{3.19}$$

$$\bar{f}_{eq}(\bar{v}) = \begin{cases} \frac{HR}{6k_{eq}Z^{*3}\left[\bar{Z}-\bar{v}(\bar{t})-\bar{y}(\bar{t})\right]^2} & \text{for the non-contact region} \\ \frac{HR}{6k_{eq}\bar{a}_0^2Z^{*3}} - \frac{4E^*\sqrt{RZ^*}}{3k_{eq}}[\bar{a}_0 - \bar{Z} + \bar{v}(\bar{t}) + \bar{y}(\bar{t})]^{3/2} & \text{for the contact region} \end{cases} \tag{3.20}$$

We solve Eqs. (3.18) and (3.19) numerically to find the response of the AFM microcantilever based on the point-mass model. The AFM tip responses, obtained based on the point-mass model developed in Chapter 2, are compared with those of the distributed-parameter model, obtained based on a single-mode Galerkin discretization, in Figures 3.9a and 3.9b. As observed in the figures, the point-mass and single-mode models are in perfect agreement. We expected such a close agreement even before solving the corresponding differential equations

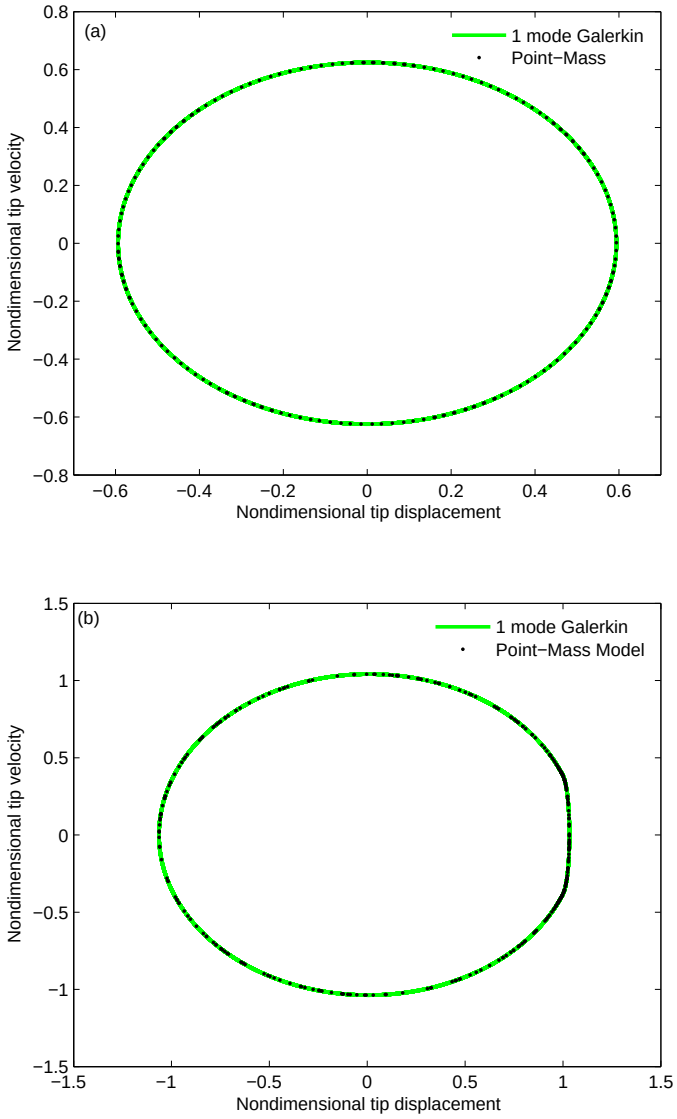

Figure 3.9: Comparison of the phase portraits of the (a) low-amplitude and (b) high-amplitude tip responses obtained with the point-mass and single-mode continuous models for $f = 47$ kHz and $\bar{Y} = 0.04$.

and constructing phase portraits because our point-mass model was tailored to be consistent with the single-mode discretization of the continuous microcantilever/tip structure and only some minor simplifications were included. We point out, here, that the goal of this section is only to compare the single-mode continuous and point-mass discrete models and, thus, the dynamics of the AFM microcantilever are not discussed here. We only mention that, for the excitation frequency and amplitude used to generate Figs. 3.9a and 3.9b, the AFM tip exhibits a bistable behavior in which low-amplitude and high-amplitude limit cycles coexist.

3.5.3 Single-Mode Approximation

We use a single-mode Galerkin discretization and generate both frequency-response curves (keeping the excitation amplitude fixed at $\bar{Y} = 0.04$ and varying the excitation frequency) and force-response curves (keeping the excitation frequency fixed at $\Omega = 46$ kHz and varying the excitation amplitude). We note that, for the AFM parameters listed in Table 3.1 and for the ranges of the excitation amplitude and frequency studied in this research, a single-mode approximation predicts that the AFM dynamics is always a period-one limit cycle; that is, no period doubling or chaotic behavior is predicted.

In Figure 3.10, we show the frequency-response curve generated by fixing the nondimensional amplitude at $\bar{Y} = 0.04$. For a certain range of the excitation frequency, two distinct stable solutions coexist: a low-amplitude non-contact branch and a high-amplitude tapping branch. Depending on the tip initial conditions, it is attracted to one of the two branches. Starting

from an excitation frequency (e.g, 40 kHz) below the fundamental natural frequency 44.7154 kHz and sweeping it up, we find that the tip amplitude increases until the limit cycle solution loses stability via a cyclic-fold bifurcation [31] at $s_1 = f = 43.46$ kHz. As a result, the tip touches the sample and enters the contact region. This region in which the tip amplitude does not change that much is called the saturated branch [28, 29]. Upon increasing the excitation frequency further, we find that the tip amplitude increases along the saturated branch and enters the bistable region and follows the high-amplitude branch. Finally, at the excitation frequency $s_4 = f = 55.6$ kHz, the periodic solution loses stability due to another cyclic-fold bifurcation. Consequently, the tip amplitude jumps down to another stable solution, the low-amplitude branch. Similarly, beginning with an excitation frequency above the first natural frequency (e.g., $f = 58$ kHz) and performing a frequency sweep down, we find that the response of the cantilever tip increases along the low-amplitude branch. Decreasing the excitation frequency further results in a saddle-node bifurcation [31] at $s_3 = f = 46.5$ kHz, which leads to a jump up to the high-amplitude branch. Finally, starting with an excitation frequency below the fundamental natural frequency and sweeping down, we find that another cyclic-fold bifurcation occurs at $s_2 = f = 43.43$ kHz and the tip jumps down to the low-amplitude non-contact branch.

Next, we fix the excitation frequency at 46 kHz, treat the excitation amplitude as the bifurcation parameter, and generate force-response curves. In Figure 3.11, we show variation of the tip amplitude with the excitation amplitude. There are two stable branches of limit cycles connected by an unstable branch of limit cycles. Increasing the excitation amplitude

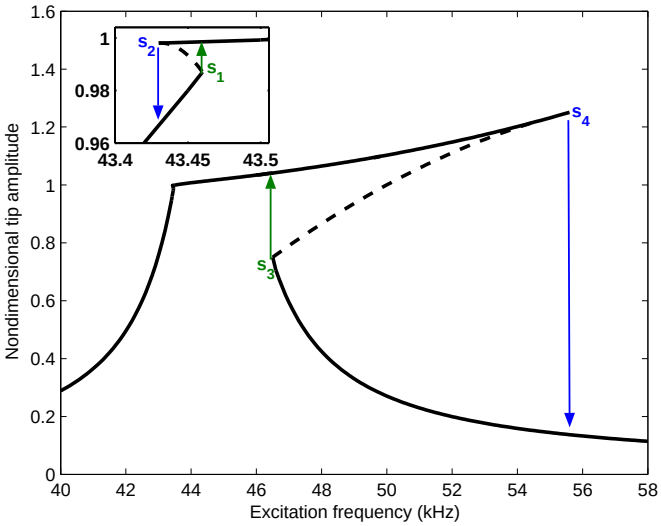

Figure 3.10: The frequency-response curve generated by fixing the nondimensional excitation amplitude at $\bar{Y} = 0.04$.

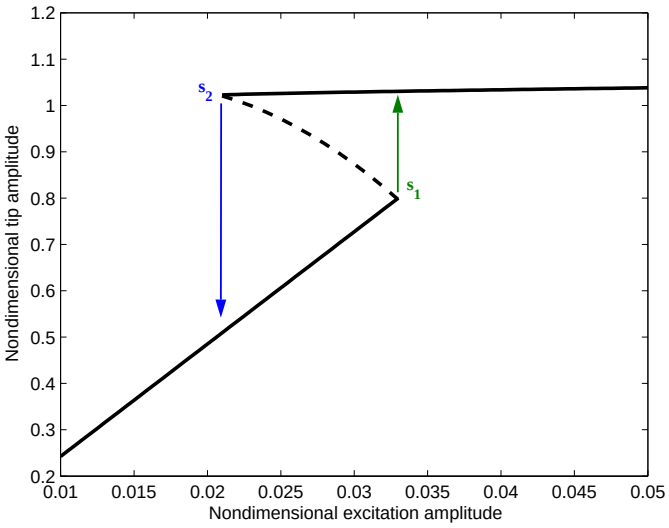

Figure 3.11: The force-response curve generated by fixing the excitation frequency at 46 kHz.

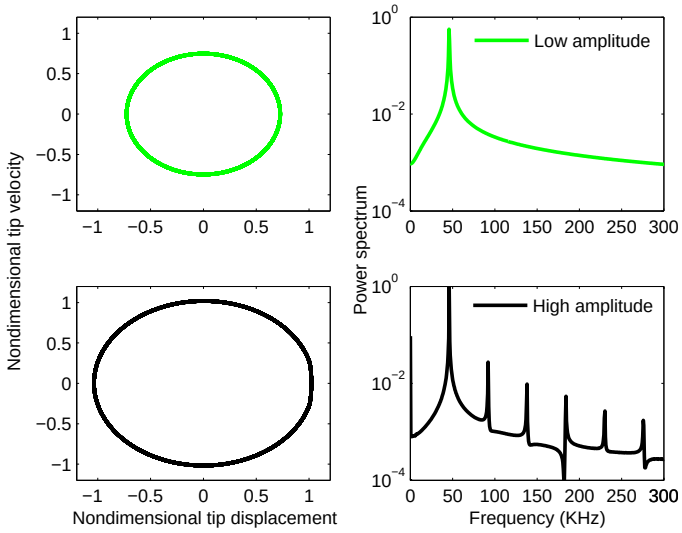

Figure 3.12: Phase portraits and spectra of the low-amplitude and high-amplitude limit cycles obtained for $\bar{Y} = 0.03$ and $f = 46$ kHz.

from a small value, we find that the tip amplitude increases along the low-amplitude stable (non-contact) branch until the excitation amplitude increases above s_1 ($\bar{Y} = 0.033$) where the tip amplitude encounters a saddle-node bifurcation. Consequently, the tip amplitude jumps up to the upper stable (contact) branch. Starting with a large excitation amplitude and decreasing it, we find that the tip amplitude decreases slowly along the upper branch until the excitation amplitude decreases below s_2 ($\bar{Y} = 0.0205$) where the tip amplitude encounters another saddle-node bifurcation. Consequently, the tip amplitude jumps down to the low-amplitude stable branch.

We note that the low-amplitude solutions contain almost a one harmonic whereas the high-amplitude solutions include higher harmonics. To get more insight into the response of the

AFM, we show in Figure 3.12 the phase portraits of the tip oscillations and their power spectra for $\bar{Y} = 0.03$ and $f = 46$ kHz. The spectrum of the high-amplitude tapping response consists of the excitation frequency, which is close to the fundamental frequency, a zero-frequency component, and higher even- and odd-harmonic components. The zero-frequency and even-harmonic components are due the quadratic nonlinearity present in the system.

3.5.4 Two-mode Approximation

Numerical results based on a two-mode Galerkin analysis are presented in this section. Again, the excitation amplitude is, first, kept constant at $\bar{Y} = 0.04$ and a frequency sweep is performed for 40 kHz $\leq f \leq$ 58 kHz. We note that, for excitation frequencies less than 44 kHz or greater than 51 kHz, the only stable solution of the system is a low-amplitude limit cycle lying in the non-contact region. This periodic solution, which is pure harmonic, is in complete agreement with the results obtained based on a one-mode analysis. In addition, for the excitation frequency range 49 kHz $\leq f \leq$ 51 kHz, the dynamical system exhibits two periodic attractors: a low-amplitude attractor and a large-amplitude attractor, as illustrated in Figure 3.13a for $f = 50$ kHz. As observed in the figure, the low-amplitude limit cycle is indistinguishable from that predicted with a one-mode discretization. In contrast, the high-amplitude limit cycle is considerably different from that predicted with a one-mode analysis. Moreover, it is worth pointing out that the two-mode tapping limit cycle penetrates into the sample slightly deeper than the one-mode high-amplitude limit cycle. Contribution of each of the two modes to the tip displacement and response are plotted in Figure 3.13b.

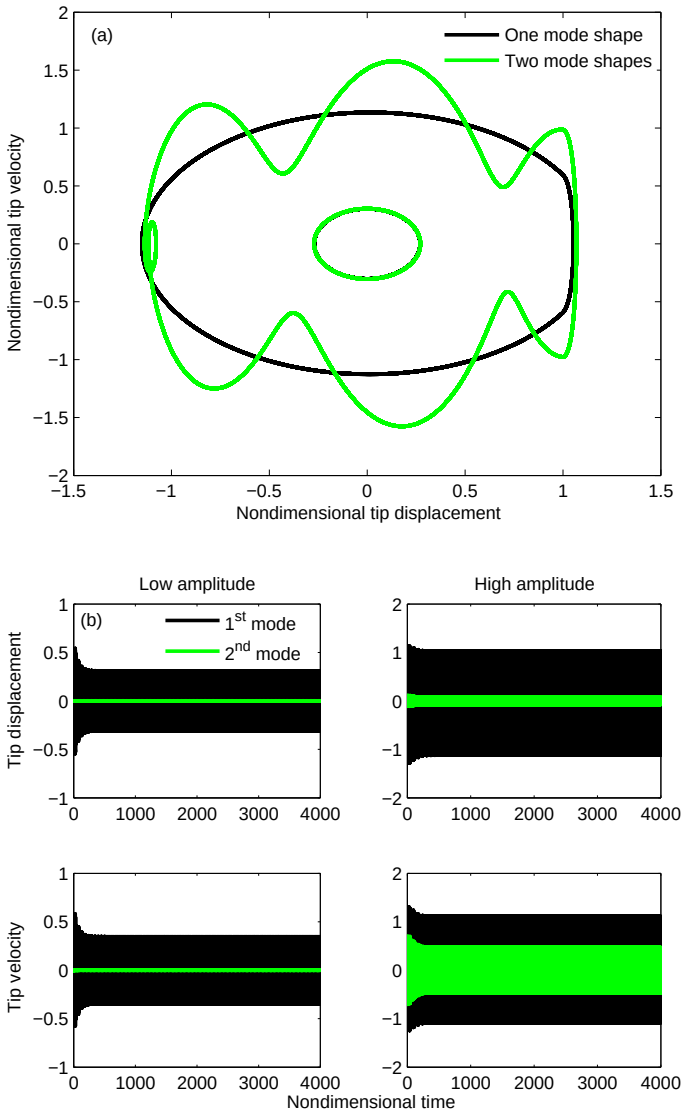

Figure 3.13: (a) Phase portraits and (b) contributions of the two modes to the time histories of the low-amplitude and high-amplitude limit cycles obtained for $\bar{Y} = 0.04$ and $f = 51$ kHz.

It is seen that the second mode has nearly no contribution to the low-amplitude response, whereas it has a significant contribution to the high-amplitude tapping response. Moreover, we observe that the effect of the second mode is stronger on the tip velocity rather than on the displacement.

We note that the aim of this section is only to emphasize the inadequacy of a one-mode discretization and the necessity of using a high number of modes in the Galerkin procedure and not to detect all different kinds of bifurcations occurring over the wide range of frequency under consideration (i.e., 44 kHz $\leq f \leq$ 49 kHz) or to identify the route leading to chaotic motion. Furthermore, as it will be discussed later, a two-mode Galerkin discretization is, in general, not enough to accurately determine the dynamical response of the AFM. Hence, for the sake of brevity, our attention is only limited to a few cases in which a two-mode discretization results in qualitatively different responses compared with those predicted with a one-mode discretization. For example, the nonlinear dynamics of the cantilever tip is closely examined through constructing phase portraits, Poincaré maps, and power spectra for $f = 44$ kHz and $f = 48$ kHz. As demonstrated in Figure 3.14a for $f = 44$ kHz, a one-mode analysis yields a period-one attractor, whereas a two-mode discretization predicts a period-two attractor, resulting from a period doubling bifurcation. It can be inferred from the phase portrait in Figure 3.14a, the Poincaré map in Figure 3.14b, and the broadband power spectrum in Figure 3.14c for $f = 48$ kHz that the tip motion determined with a two-mode analysis is chaotic. On the other hand, the response predicted with a one-mode discretization is a limit cycle. We also note that a low-amplitude periodic attractor coexists with either

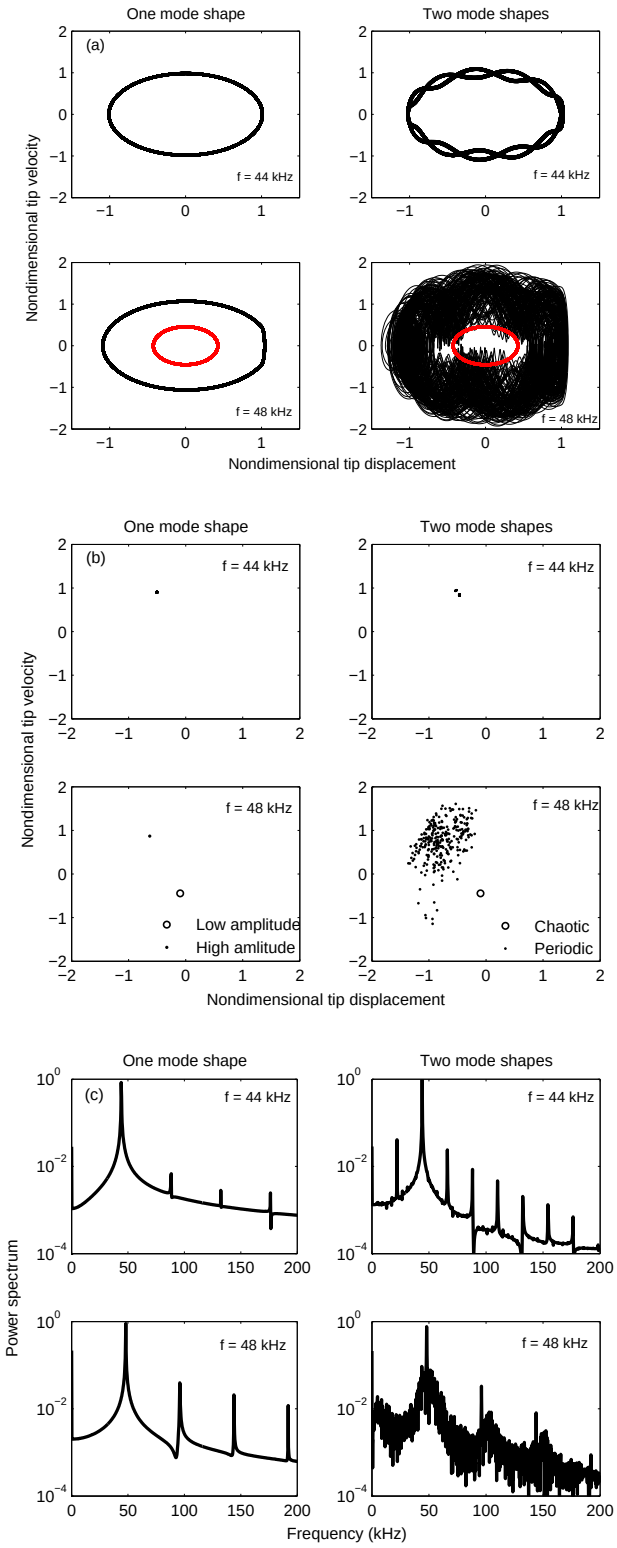

Figure 3.14: (a) Phase portraits, (b) Poincaré maps, and (c) power spectra of the attractors predicted with one-mode and two-mode discretizations for $\bar{Y} = 0.04$, $f = 44$ kHz, and $f = 48$ kHz.

a high-amplitude periodic attractor or a chaotic attractor. As seen in Figure 3.14a, the low-amplitude limit cycle is captured accurately with even a one-mode approximation.

Next, the excitation frequency is held constant at $f = 46$ kHz and the excitation amplitude is swept from a small value of $\bar{Y} = 0.01$ to $\bar{Y} = 0.05$. Because the results for each amplitude are similar, in essence, to those of the frequency sweep, the general behavior of the dynamical system may be summarized as follows:

1. For the range of excitation amplitude $\bar{Y} < 0.0209$, the only response of the cantilever tip is a periodic orbit lying in the non-contact region. The tip enters the contact region (i.e., undergoes a grazing bifurcation) at $\bar{Y} = 0.0209$, which is the same as the one predicted with a one-mode discretization. In this interval, no qualitative or quantitative difference is observed between the one-mode and two-mode results.

2. For $0.0209 \leq \bar{Y} < 0.033$, a non-contact period-one orbit coexists with a tapping period-two orbit. Again, the tip undergoes grazing bifurcation at the same value $\bar{Y} = 0.033$ obtained with a one-mode discretization (see Figure3.15a).

3. For $0.033 \leq \bar{Y} \leq 0.05$, the only response of the system is a tapping period-two orbit (see Figure3.15b).

4. No chaotic motion is detected using two modes in the discretization.

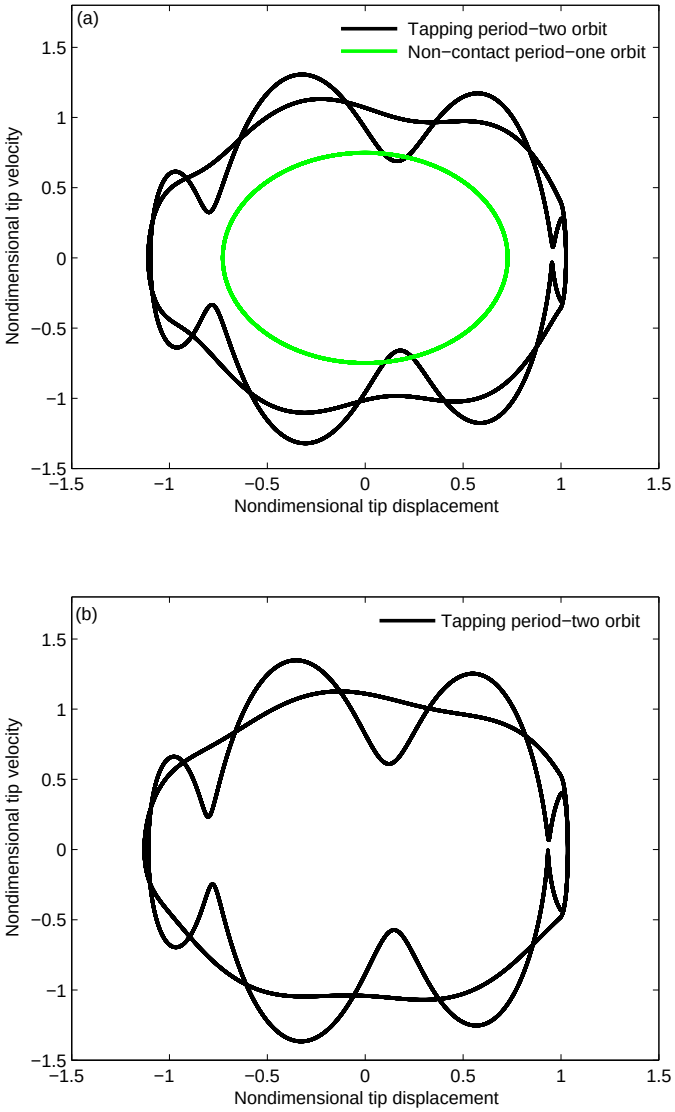

Figure 3.15: Phase portraits of the attractors obtained with a two-mode discretization for (a) $\bar{Y} = 0.03$ and (b) $\bar{Y} = 0.05$.

3.5.5 Higher-Mode Approximation

To determine the number of modes required to accurately describe the nonlinear dynamics of the AFM cantilever, we carried out an extensive investigation based on three, four, and five modes in the Galerkin discretization for various excitation amplitudes and frequencies over the aforementioned range under consideration. The numerical studies reveal that, for the present AFM parameters, four modes are sufficient not only to identify qualitative characteristics of the dynamical system, such as the different types of bifurcations and routes to chaos, but also to estimate its quantitative aspects with acceptable accuracy. Therefore, for brevity, our attention is focused in this section on a four-mode discretization. Similar to previous sections, the excitation amplitude is held constant at $\bar{Y} = 0.04$ and a frequency sweep is done. The resulting frequency-response curves are, briefly, presented here. Starting with $f = 40$ kHz and increasing it, we find that the only response of the system is a non-contact periodic orbit, which is in excellent agreement with those obtained by using one- and two-mode discretizations. As the excitation frequency approaches $f = 43.5$ kHz, a period doubling bifurcation occurs and a period-two orbit is born. Upon increasing the excitation frequency further, the system undergoes another qualitative change at $f = 44.1$ kHz and the tip follows a tapping mode period-one limit cycle. Then, it goes directly to chaotic motion through a grazing bifurcation [39] at $f = 44.9$ kHz. We note that the common characteristic of all various responses presented so far is that the dynamical system possesses only one attractor, which might be period-one, period-two, or chaotic motion, depending on the excitation frequency. It should be also mentioned that the grazing bifurcation occurring here is

a typical grazing bifurcation in which a stable period-one attractor goes directly to a chaotic attractor without being preceded by any classical route to chaos [31]. Grazing bifurcations are, in essence, characteristic of impact oscillators in which an oscillating object impacts frequently some other object [39]. As the excitation frequency exceeds 46.2 kHz, the chaotic attractor is diminished gradually and replaced by two periodic attractors: a low-amplitude non-contact attractor and a high-amplitude grazing attractor. As the excitation frequency is increased, the non-contact periodic attractor persists over the range of frequency under consideration but its amplitude decreases slowly. On the other hand, the high-amplitude periodic attractor becomes chaotic through another grazing bifurcation as the excitation frequency exceeds $f = 46.7$ kHZ and eventually vanishes at $f = 48.2$ kHz. The phase portraits of the response for the entire process are presented in Figure 3.16. It is worth noting that the frequency range over which the tip dynamics exhibits two stable attractors is considerably wider for the one-mode results than those obtained with more modes in the discretization (See Fig. 3.10). Moreover, comparing the two period-two orbits predicted with two- and four-mode discretizations for $f = 44$ kHz, we conclude that, despite the good quantitative and qualitative agreement between the two results, the shapes of the attractors are different in these cases.

To investigate the influence of each mode on the total response of the cantilever tip, we delineate the contribution of each mode in Figures 3.17a and 3.17b for $f = 47.5$ kHz. This choice of frequency, which corresponds to a chaotic motion, is also helpful to get more insight into chaos in atomic force microscopy. As observed in the figures, the contribution of the

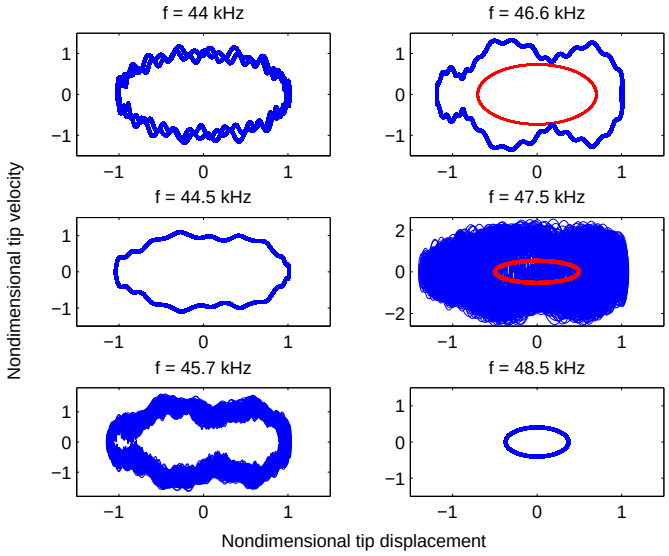

Figure 3.16: Phase portraits of the attractors obtained with a four-mode discretization for $\bar{Y} = 0.04$ and six excitation frequencies.

second mode is significant, especially, to the velocity. In addition, the third and fourth modes have a quite noticeable effect on the total velocity. This might be, partly, due to the fact that energy transfer between modes is higher in chaotic motions than in periodic motions. We note that contribution of the second and higher modes to the non-contact periodic attractor that coexists with the chaotic attractor is negligible compared to that of the first mode and therefore it is not plotted in Figures 3.17a and 3.17b (see also Figure 3.13b).

Finally, the excitation frequency is held fixed at $f = 46$ kHz and an upward excitation amplitude sweep is performed staring with $\bar{Y} = 0.01$ for which the only response of the system is a non-contact periodic (low-amplitude limit cycle) attractor. As the excitation amplitude exceeds $\bar{Y} = 0.0213$, a chaotic attractor is born, coexisting with a low-amplitude

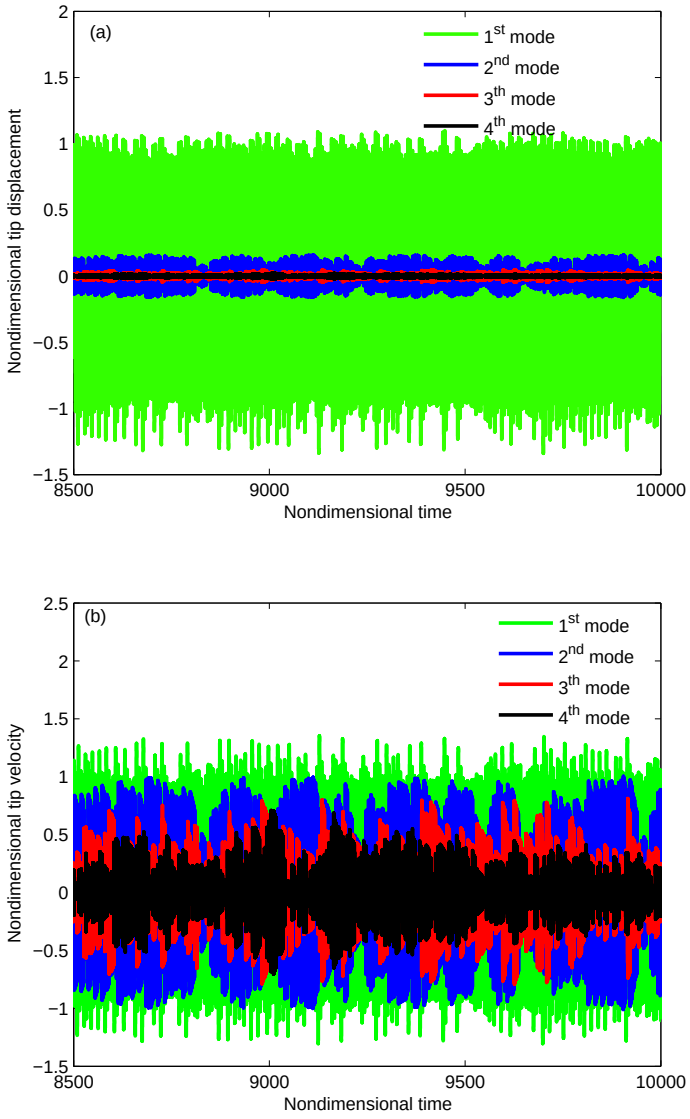

Figure 3.17: Contributions of the four modes to the time history of the tip (a) displacement and (b) velocity obtained for $\bar{Y} = 0.04$ and $f = 47.5$ kHz.

limit cycle. At $\bar{Y} = 0.025$, the chaotic attractor is replaced by a tapping periodic attractor. A period doubling bifurcation takes place afterwards at $\bar{Y} = 0.026$ followed by a sequence of period doubling bifurcations culminating in a chaotic attractor at $\bar{Y} = 0.036$. This is regarded as one of the well-established routes to chaos [31]. The period doubling route to chaos is portrayed in Figures 3.18a and 3.18b via phase portraits and power spectra, respectively. We note that, for brevity, the power spectra are depicted only for the attractor experiencing the period doubling scenario. It is worth mentioning that the non-contact periodic attractor, which coexists with the tapping periodic attractor, continues to coexist with all period doubled attractors and also the outset of the chaotic motion. As the excitation amplitude is increased further, this attractor is replaced with a tapping periodic attractor coexisting with the chaotic attractor. These coexisting attractors are, finally, replaced with a fully chaotic regime at $\bar{Y} = 0.044$. We emphasize that, in contrast with the four-mode discretization, a two-mode discretization fails to predict the chaotic attractor and the period doubling route to chaos.

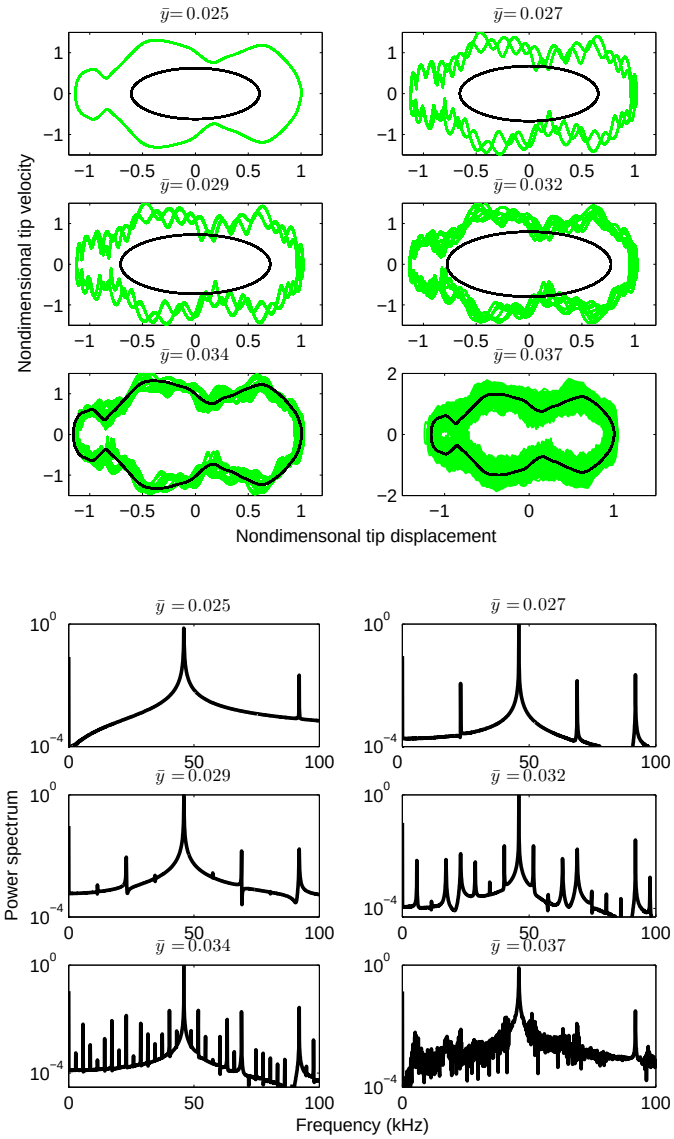

Figure 3.18: (a) Phase portraits and (b) power spectra of the period doubled attractors that lead to chaos predicted with a four-mode discretization for $f = 46$ kHz.

Chapter 4

Nonlinear Dynamics of the AFM Microcantilever in the Bistable Phase

As discussed earlier, the contact and non-contact nonlinear interaction forces between the microcantilever tip and the sample causes two different operational regimes in tapping mode atomic force microscopy: monostable and bistable regimes. Depending on the initial tip/sample separation, the AFM operates in either the monostable or the bistable regime. Dynamics of the AFM microcantilever in the monostable phase was discussed in Chapter 3. The objective of the present chapter is to investigate the nonlinear dynamics of AFM probes in the bistable region where the microcantilever tip is initially located in the bistable region, which is, generally, close to the sample. Because two stable attractors coexist in the corresponding static bifurcation diagram, the dynamical behavior of the microcantilever in this region is expected to be considerably different from those in the monostable region.

Starting with the nonlinear partial-differential equation and associated boundary conditions governing the microcantilever motion given by Eqs. (2-12)-(2.14), we develop a reduced-order model based on the differential quadrature method (DQM) [52–55]. Because forward integration in time is computationally expensive, we employ the finite difference method (FDM) [31] to compute limit-cycle responses of the dynamical system. We note that the FDM not only provides an efficient way for calculating stable limit cycles but it is also capable of calculating unstable limit cycles, which cannot be calculated using forward integration [31].

4.1 Differential Quadrature Method

Most engineering problems are governed by a set of partial-differential equations. It is very difficult, in general, to find a closed-form solution for such equations. Approximate solutions have been, therefore, developed to solve PDEs. In most cases, the approximate solutions are represented by functional values at certain discrete points (grid points or mesh points). There are many numerical discretization methods available in the literature. Among them, the finite difference method (FDM), finite element method (FEM), and finite volume method (FVM) are regarded as lower-order methods, while spectral and pseudospectral methods are considered global methods. Most numerical solutions of the engineering problems can be carried out by low-order methods, such as FEM, FDM, and FVM. In some applications the numerical solutions of the partial-differential equations are required only at a few specified

points. To achieve a sufficiently accurate solution, lower-order methods still need a large number of grid points. As a result, a lot of virtual storage and massive computational effort are required. Higher-order methods, on the other hand, can result in accurate numerical solutions using very few grid points because the higher-order methods, in general, have a higher order of truncation error.

In an attempt to present an efficient discretization technique to achieve precise numerical solutions by employing a remarkably small number of grid points, researchers have introduced the differential quadrature method (DQM) [52, 63–65]. The basic idea behind the DQM is that a partial derivative of a function with respect to a coordinate direction is expressed as a linear weighted sum of all of the function values at all grid (mesh) points along that direction. Historically, the DQM was initiated based on the idea of the integral quadrature. The main problem in the DQ method is to determine the weighting coefficients for the discretization of the derivatives of the different orders. Several different methods have been proposed in the literature to compute the weighting coefficients within the DQM [52, 63, 66–68].

Lagrangian interpolation polynomials have been employed as test functions to present an explicit formula to obtain the weighting coefficients [66, 67]. Such a DQ method in which polynomials are used as the test functions to approximate the solution is referred as the polynomial-based differential quadrature method (PDQM). A major breakthrough in the determination of the weighting coefficients was made by employing a linear vector space analysis [68]. Using the properties of linear vector spaces, it was shown that all of the methods used to compute the weighting coefficients in the DQM can be generalized by

a convenient choice of the base vectors in the linear vector space [68]. In this generalized differential quadrature method (GDQM), the weighting coefficients associated the first-order derivative are determined by a simple algebraic equation without any restriction on the choice of the grid points and the weighting coefficients of the second- and higher- order derivatives are determined by a recursive relation [68]. It is worth mentioning that the solution of the partial-differential equations may be, alternatively, approximated based on a linear vector space analysis by a Fourier series expansion. The DQ formulation for this approach is different from that of the PDQM and is called the Fourier expansion-based differential quadrature method (FDQM) [69, 70].

In the present investigation, we use the generalized differential quadrature method in which the Lagrangian interpolation polynomials are used as test functions and the roots of the shifted Legendre polynomial are utilized to determine the grid point distribution [54,71]. We apply the DQM to Eqs. (2.12) through (2.14) to discretize the spatial derivatives. Similar to other discretization methods, the DQM transforms the partial-differential equation of motion and associated boundary conditions into a set of ordinary-differential equations governing the time evolution of the dynamical system. The DQM approximates the derivatives of a function w with respect to a variable ζ at a given discrete point ζ_i as a weighted linear sum of the function values at the preselected sampling (grid) points in the field domain [54, 55]; that is,

$$\frac{d^r w}{d\zeta^r} = \sum_{j=1}^{N} A_{ij}^{(r)} w_j \qquad i = 1, 2, \ldots, N \tag{4.1}$$

where N is the number of preselected sampling points and w_j represents the deflection of the

microcantilever jth grid point. In addition, the $A_{ij}^{(r)}$ are elements of the weighting coefficient matrix corresponding to the r-th order derivative. The off-diagonal elements of the weighting coefficient matrix of the first-order derivative are determined as [54, 72]

$$A_{ij}^{(1)} = \frac{\prod_{\substack{v=1 \\ v\neq i}}^{N}(\zeta_i - \zeta_v)}{(\zeta_i - \zeta_j)\prod_{\substack{v=1 \\ v\neq j}}^{N}(\zeta_j - \zeta_v)} \qquad i, j = 1, 2, 3, \ldots, N \quad j \neq i \tag{4.2}$$

The off-diagonal elements of the weighting coefficient matrix of the higher-order derivatives are given by [54, 72]

$$A_{ij}^{(r)} = r\left[A_{ii}^{(r-1)}A_{ij}^{(1)} - \frac{A_{ij}^{(r-1)}}{\zeta_j - \zeta_v}\right] \qquad i, j = 1, 2, 3, \ldots, N \quad j \neq i \tag{4.3}$$

The diagonal elements of the weighting coefficient matrix are found through [54, 72]

$$A_{ii}^{(r)} = -\sum_{\substack{v=1 \\ v\neq i}}^{N} A_{iv}^{(r)} \qquad i = 1, 2, 3, \ldots, N \tag{4.4}$$

As aforementioned, using the Lagrangian interpolation polynomials as test functions in the generalized differential quadrature method, there is no restriction on the choice of the grid points. However, to obtain a more accurate solution, the distribution of sampling points within the variable domain is assumed to be given by the following equation [54, 72, 73]:

$$\zeta_i = \frac{1}{2}\left[1 - \cos\left(\frac{i-1}{N-1}\pi\right)\right] \qquad i = 1, 2, 3, \ldots, N \tag{4.5}$$

4.2 Model Discretization

We introduce the following nondimensional variables (denoted by bars):

$$\zeta = \frac{x}{l}, \quad \bar{t} = t\omega_1, \quad \bar{w} = \frac{w}{Z^*}, \quad \bar{Z} = \frac{Z}{Z^*}, \quad \bar{a}_0 = \frac{a_0}{Z^*}, \quad \bar{Y} = \frac{Y}{Z^*}, \quad \bar{\Omega} = \frac{\Omega}{\omega_1} \tag{4.6}$$

Starting with Eqs. (2.12)-(2.14) and utilizing nondimensional parameters introduced by Eq. (4.6), we rewrite the partial-differential equation and associated boundary conditions in the following nondimensional form:

$$\frac{EI}{\rho A\omega_1^2 l^4}\frac{\partial^4 \bar{w}(\zeta,\bar{t})}{\partial \bar{t}^4}+\frac{\partial^2 \bar{w}(\zeta,\bar{t})}{\partial \bar{t}^2}+\bar{c}\frac{\partial \bar{w}(\zeta,\bar{t})}{\partial \bar{t}}=-\left[\frac{d^2\bar{y}}{d\bar{t}^2}+\bar{c}\frac{d\bar{y}}{d\bar{t}}\right] \tag{4.7}$$

$$w(0,\bar{t})=0,\quad \frac{\partial w(0,\bar{t})}{\partial \bar{t}}=0,\quad \frac{\partial^2 w(1,\bar{t})}{\partial \bar{t}^2}=0 \tag{4.8}$$

$$\frac{\partial^3 \bar{w}(1,\bar{t})}{\partial \bar{t}^3}=-\frac{HRl^3}{6EIZ^{*3}[\bar{Z}-\bar{w}(1,\bar{t})-\bar{y}(\bar{t})]^2} \qquad \text{if } \bar{z}\geq \bar{a}_0 \tag{4.9a}$$

$$\frac{\partial^3 \bar{w}(1,\bar{t})}{\partial \bar{t}^3}=-\frac{HRl^3}{6EIa_0^2Z^{*3}}+\frac{4E^*l^3}{3EI}\sqrt{RZ^*}[\bar{a}_0-\bar{Z}+\bar{w}(1,\bar{t})+\bar{y}(\bar{t})]^{3/2} \qquad \text{if } \bar{z}<\bar{a}_0 \tag{4.9b}$$

with $\bar{c}=\frac{c}{\rho A\omega_1}$. Now, we use Eq. (4.1) to discretize Eqs. (4.7)-(4.9). The result is

$$\frac{d^2\bar{w}_i}{d\bar{t}^2}+\bar{c}\frac{d\bar{w}_i}{d\bar{t}}+\frac{EI}{\rho A\omega_1^2 l^4}\sum_{j=2}^{N}A_{ij}^{(4)}\bar{w}_j=-\left[\frac{d^2\bar{y}}{d\bar{t}^2}+\bar{c}\frac{d\bar{y}}{d\bar{t}}\right] \qquad i=2,\ldots,N \tag{4.10}$$

and

$$\sum_{j=2}^{N}A_{1j}^{(1)}\bar{w}_j=0 \tag{4.11}$$

$$\sum_{j=2}^{N}A_{Nj}^{(2)}\bar{w}_j=0 \tag{4.12}$$

$$\sum_{j=2}^{N}A_{Nj}^{(3)}\bar{w}_j=-\frac{HRl^3}{6EIZ^{*3}[\bar{Z}-\bar{w}_N-\bar{y}(\bar{t})]^2} \qquad \text{if } \bar{z}\geq \bar{a}_0 \tag{4.13a}$$

$$\sum_{j=2}^{N}A_{Nj}^{(3)}\bar{w}_j=-\frac{HRl^3}{6EI\bar{a}_0^2Z^{*3}}+\frac{4E^*l^3}{3EI}\sqrt{RZ^*}[\bar{a}_0-\bar{Z}+\bar{w}_N+\bar{y}(\bar{t})]^{3/2} \qquad \text{if } \bar{z}<\bar{a}_0 \tag{4.13b}$$

It is pointed out that the zero-deflection boundary condition at the clamped end requires that $\bar{w}_1=0$. We note that a proper implementation of the boundary condition is very important for obtaining an accurate numerical solution with the DQM. Several methods

have been employed to implement the boundary conditions for structural problems. The partial-differential equations governing the motion of a structural element, such as a beam, plate, or shell are fourth-order in the space variable. Therefore, we need to apply two boundary conditions at each boundary node (grid point). The δ-technique was proposed to address the difficulties in the implementation of two boundary conditions at a single grid point [74]. In this method, the Dirichlet boundary condition (i.e., the boundary condition on displacement) is applied at the boundary point itself and the derivative condition is applied at its adjacent point, which is at a distance δ from the boundary point. It is obvious that the derivative boundary condition is not exactly satisfied by the δ-technique and numerical results are expected to depend on the choice of the δ-value. To obtain an accurate solution, one should chose the value of δ to be very small. This small value of δ, however, gives rise to a very small-spacing mesh close to the boundary, which is not consistent with the other mesh points. Consequently, the DQ coefficient matrices become ill-conditioned, which might lead to inaccurate results.

In an attempt to improve the δ-technique drawbacks, Wang and Bert [75] introduced another method in which only one of the boundary conditions is implemented at each boundary point and the second one is built into the DQ weighting coefficient matrices. Another method for boundary condition implementation, which is employed in the present study, directly substitutes the boundary conditions into the discretized governing equations [76, 77]. Details of this approach are described here for a one-dimensional problem; say a free-end cantilever. In this approach, the Dirichlet boundary condition (i.e, $w_1 = 0$) is applied at the boundary

point (i.e., point 1), whereas the derivative boundary conditions are discretized using the DQ formulation given by Eq. (4.1). The discretized conditions at the boundary points yield the following three algebraic equations in terms of $\bar{w}_2$, $\bar{w}_3$,..., and $\bar{w}_N$:

$$\sum_{j=2}^{N} A_{1j}^{(1)} \bar{w}_j = 0$$

$$\sum_{j=2}^{N} A_{Nj}^{(2)} \bar{w}_j = 0$$

$$\sum_{j=2}^{N} A_{Nj}^{(3)} \bar{w}_j = 0$$

These algebraic equations are solved for $\bar{w}_2$, $\bar{w}_{N-1}$, and $\bar{w}_N$ in terms of the deflections at the other grid points $\bar{w}_3$, $\bar{w}_4$,..., $\bar{w}_{N-2}$. The results are substituted into the discretized equation, which is applied at the interior points (i.e., $i = 3, 4, 5,..., N-2$). Therefore, this procedure ends up with a system of $N-4$ linear algebraic equations in terms of $N-4$ unknowns.

We can, alternatively, find $\bar{w}_2$, $\bar{w}_3$, and $\bar{w}_N$ in terms of $\bar{w}_4$, $\bar{w}_5$,..., $\bar{w}_{N-1}$ and follow the same procure to obtain $N-4$ algebraic equations. This way, the deflection of the end point $\bar{w}_N$ is one of the unknowns and therefore solution of the algebraic system directly yields $\bar{w}_N$. This approach is very convenient for the AFM problem where the deflection of the end point (i.e., where the tip is located) matters only. However, for the AFM problem, one of the boundary conditions is a highly nonlinear function of $\bar{w}_N$ (see Eqs. (4.13a) and (4.13b)) and, hence, it is not possible to find closed-form relationships for $\bar{w}_2$, $\bar{w}_3$, and $\bar{w}_N$ in terms of the deflections of the other grid points.

Two different ways are suggested here to address this issue. One way is solving Eqs. (4.11),

(4.12), and (4.13) for $\bar{w}_2$, $\bar{w}_3$, and $\bar{w}_{N-1}$ in terms of $\bar{w}_4$, $\bar{w}_5$,..., $\bar{w}_{N-2}$, $\bar{w}_N$. This way, $\bar{w}_2$, $\bar{w}_3$, and $\bar{w}_{N-1}$ are obtained as functions of the other grid point deflections. These functions are nonlinear in terms of $\bar{w}_N$ but linear terms of the other deflections. Substituting the expressions for $\bar{w}_2$, $\bar{w}_3$, and $\bar{w}_{N-1}$ into Eq. (4.10) yields a system of $N-4$ second-order nonlinear ODEs applied at the grid points $i = 4, 5,..., N-2, N$. For the sake of brevity, a detailed description of this method is not displayed here.

The second approach to impose the nonlinear boundary condition, which is presented here in detail, is to use Eqs. (4.11) and (4.12) to express $\bar{w}_2$ and $\bar{w}_3$ in terms of $\bar{w}_4$, $\bar{w}_5$,..., $\bar{w}_{N-1}$, $\bar{w}_N$; that is,

$$\bar{w}_2 = \sum_{j=4}^{N} a_j \bar{w}_j \tag{4.14a}$$

$$\bar{w}_3 = \sum_{j=4}^{N} b_j \bar{w}_j \tag{4.14b}$$

where

$$a_j = \frac{A_{13}^{(1)} A_{Nj}^{(2)} - A_{1j}^{(1)} A_{N3}^{(2)}}{A_{12}^{(1)} A_{N3}^{(2)} - A_{13}^{(1)} A_{N2}^{(2)}}$$

$$b_j = \frac{A_{1j}^{(1)} A_{N2}^{(2)} - A_{12}^{(1)} A_{Nj}^{(2)}}{A_{12}^{(1)} A_{N3}^{(2)} - A_{13}^{(1)} A_{N2}^{(2)}}$$

Equations (4.14a) and (4.14b) are, next, substituted into Eqs. (4.10), (4.13a), and (4.13b) to obtain the following differential-algebraic equations (DAE) [78, 79]:

$$\frac{d^2\bar{w}_i}{d\bar{t}^2} + \bar{c}\frac{d\bar{w}_i}{d\bar{t}} + \frac{EI}{\rho A \omega_1^2 l^4} \sum_{j=4}^{N} A_{ij}\bar{w}_j = -\left[\frac{d^2\bar{y}}{d\bar{t}^2} + \bar{c}\frac{d\bar{y}}{d\bar{t}}\right] \qquad i = 4, 5, \ldots, N-1 \tag{4.15}$$

$$\sum_{j=4}^{N} c_j \bar{w}_j = -\frac{HRl^3}{6EIZ^{*3}[\bar{Z} - \bar{w}_N - \bar{y}(\bar{t})]^2} \qquad \text{if } \bar{z} \geq \bar{a}_0 \tag{4.16a}$$

$$\sum_{j=4}^{N} c_j \bar{w}_j = -\frac{HRl^3}{6EI\bar{a}_0^2 Z^{*3}} + \frac{4E^* l^3}{3EI}\sqrt{RZ^*}[\bar{a}_0 - \bar{Z} + \bar{w}_N + \bar{y}(\bar{t})]^{3/2} \qquad \text{if } \bar{z} < \bar{a}_0 \quad (4.16b)$$

where

$$A_{ij} = A_{ij}^{(4)} + A_{i2}^{(4)} a_j + A_{i3}^{(4)} b_j$$

$$c_j = A_{Nj}^{(3)} + A_{N2}^{(3)} a_j + A_{N3}^{(3)} b_j$$

We note that the present DAE system consists of $N-4$ linear differential equations and one nonlinear algebraic equation. We also note that two methods were presented in this section for implementing the boundary conditions when one of the boundary conditions is nonlinear. The first method results in a system of $N-4$ second-order nonlinear ODEs, which must be solved simultaneously. On the other hand, the second method leads to a system of nonlinear DAEs, $N-4$ linear ODEs and a nonlinear algebraic equation must be solved simultaneously. Solution of a nonlinear algebraic equation at each step of numerical integration might seem to be inefficient and computationally costly, but a close examination of the nonlinear algebraic equations appearing in (4.13a) and (4.13b) reveals that both of them can be converted to a cubic equation in terms of $\bar{w}_N$. Because cubic equations can be analytically solved using the closed-form Cardano formula, there is no need to solve a nonlinear algebraic equation numerically and the real roots can be calculated using a closed-form formula. This closed-form formula results in a notable reduction in the computational time.

In summary, we need to solve $2N-8$ first-order nonlinear ODEs in the first approach and $2N-8$ linear ODEs along with one cubic equation (for which a closed-form formula is

available) in the second approach. If explicit integration methods are employed to solve the initial-value problem, no algebraic equation is solved for numerical integration and therefore there is no significant difference between the two methods in terms of time and computational efficiency. However, if implicit methods are utilized, $2N-8$ nonlinear algebraic equations need to be solved at each time step in the first method and $2N-8$ linear algebraic equations and a cubic equation need to be solved at each step. Thus, it seems that the second method is computationally more efficient, despite the challenges one may encounter for numerical solution of the DAEs. In addition, as discussed later in this chapter, a finite difference method (FDM) is used to discretize periodic orbits. To compute a periodic orbit with the FDM, we need to solve $m(2N-8)$ nonlinear algebraic equations in the first approach and $m(2N-8)$ linear equations and m nonlinear equations in the second approach, where m is the number of grid points on the orbit. There are some special numerical schemes for numerical solution of nonlinear algebraic systems to reduce computational cost when some of the equations are linear. Using such numerical methods would significantly reduce the computational efforts. Hence, it seems that the second approach is more efficient in terms of computational cost and time.

We numerically implemented both methods and found out that they yield the same numerical results. Therefore only the latter method is described in this Dissertation (i.e., the method that ends up with the DAE system).

4.3 Static Deflection

Dropping the external excitation and all of the terms involving the time derivatives in Eqs. (2.12)-(2.14), discretizing the outcome using Eq. (4.1), and implementing the boundary conditions, as described earlier in this chapter, yield the following algebraic equations governing the static deflection of the microcantilever:

$$\sum_{j=4}^{N} A_{ij} w_j^* = 0 \qquad i = 4, \ldots, N-1 \tag{4.17}$$

and

$$\sum_{j=4}^{N} c_j w_j^* = -\frac{HR}{6EI[Z - w_N^*]^2} \tag{4.18a}$$

for the non-contact region and

$$\sum_{j=4}^{N} c_j w_j^* = -\frac{HR}{6EIa_0^2} + \frac{4E^*}{3EI}\sqrt{R}[a_0 - Z + w_N^*]^{3/2} \tag{4.18b}$$

for the contact region, where w_j^* denotes the static equilibrium deflection of the jth grid point. Equations (4.17) and (4.18) represent a system of $N-4$ linear and one nonlinear algebraic equations. This system can be solved for a given value of Z to obtain the equilibrium tip/sample separation gap; that is, $Z^* = Z - w_N^*$. We note that the exact static deflection can be obtained based on an exact analysis without any discretization, as discussed in Chapter 2. As illustrated in Fig. 4.1, the static deflection obtained using the DQM with $N = 5$ is in complete agreement with the exact solution ($N = 5$ is the minimum grid points possible in the DQM). We note that the static curve displayed in Fig. 4.1 may be, alternatively, generated by treating Z^* as a known parameter and solving the algebraic system for Z; this

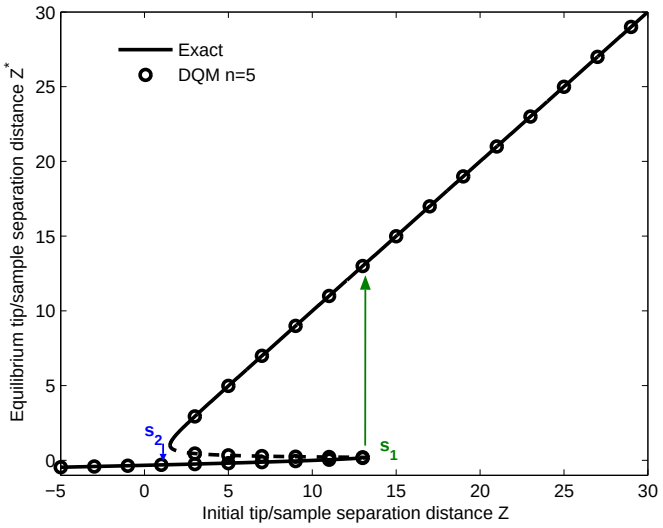

Figure 4.1: Variation of the equilibrium tip/sample separation with the initial tip/sample separation.

way the nonlinear system of the algebraic equations is reduced to a linear system in terms of the w_j^*, which is computationally less expensive than the original nonlinear system:

$$\sum_{j=4}^{N} c_j w_j^* = -\frac{HR}{6EIZ^{*2}} \tag{4.19a}$$

for the non-contact region and

$$\sum_{j=4}^{N} c_j w_j^* = -\frac{HR}{6EIa_0^2} + \frac{4E^*}{3EI}\sqrt{R}[a_0 - Z^*]^{3/2} \tag{4.19b}$$

for the contact region.

The AFM parameters given in Ref. [29], and tabulated in Table 4.1, are used for all numerical simulations performed throughout this chapter. We note that this AFM was chosen to provide a rather large bistable region compared to that of the AFM used for numerical

Table 4.1: Parameters and properties of the AFM

Tip radius R	20 nm
Cantilever length l	240 μm
Cantilever width b	64 μm
Cantilever thickness h	2.1 μm
Density ρ	2300 kg/m^3
Modulus of elasticity E	176 GPa
Effective modulus of elasticity E^*	10.4 GPa
Quality factor in air Q	66.7
Hamaker constant H	2.96 $e^{-19}J$
Intermolecular distance a_0	0.2 nm

simulations in Chapter 3. Variation of the tip/sample equilibrium distance with the initial tip/sample separation distance is displayed in Fig. 4.1. As demonstrated in the figure, depending on the initial tip/sample gap, there are two distinct operating regions: monostable and bistable regions. If the tip is initially located in either the region $Z < s_2 = 1.522$ nm or the region $Z > s_1 = 13.246$ nm, only one stable equilibrium position Z^* exists for the tip. However, if the tip is initially located between the two saddle-node bifurcations [22] $s_2 < Z < s_1$, two coexisting equilibrium positions are feasible for the tip: one located in the contact region and the other located in the non-contact region. Starting with an initial tip/sample distance far from the sample ($Z > s_1$) and approaching the sample, we find that

the tip follows the non-contact branch of the bistable region. On the other hand, starting with a small initial tip/sample distance close to the sample ($Z < s_2$) and increasing the gap, we find that the tip follows the contact branch. The latter is not of practical interest because the tip is, in fact, stuck to the sample. We note that the nonlinear dynamics of the microcantilever is expected to be totally different in the monostable and bistable regions [13]. In what follows, free and forced vibrations of the AFM microcantilever are studied using nonlinear dynamics tools in the bistable region.

4.4 Free Vibrations of The AFM Probe

We note that, because of the interaction forces between the sample and the AFM tip, the natural frequencies and mode shapes of the AFM microcantilever are, in theory, expected to be different from those of a free microcantilever. The free vibration of the microcantilever can be determined exactly by linearizing the nonlinear boundary condition and subsequently solving the corresponding eigenvalue problem, as presented in Chapter 2. However, for the sake of comparison, the DQM is employed here to discretize the free-vibration equations of the microcantilever and calculate its natural frequencies and associated mode shapes. To this end, we drop the external excitation and damping terms in Eqs. (2.12) through (2.14), introduce the nondimensional variable $\zeta = \frac{x}{l}$, employ Eq. (4.1) to discretize the equation and boundary conditions, implement the boundary conditions, and obtain

$$\ddot{w}_i + \frac{EI}{\rho A l^4} \sum_{j=4}^{N} A_{ij} w_j = 0 \qquad i = 4, 5, \ldots, N-1 \tag{4.20}$$

and

$$\sum_{j=4}^{N} c_j w_j = -\frac{HRl^3}{6EI[Z-w_N]^2} \qquad \text{if } z \geq a_0 \tag{4.21a}$$

$$\sum_{j=4}^{N} c_j w_j = -\frac{HRl^3}{6EIa_0^2} + \frac{4E^*l^3}{3EI}\sqrt{R}[a_0 - Z + w_N]^{3/2} \qquad \text{if } z < a_0 \tag{4.21b}$$

We let $w_j(t) = w_j^* + v_j(t)$, where w_j^* is the static equilibrium deflection of the jth grid point and v_j is the dynamic deflection of the same grid point around its static equilibrium, linearize the outcome using a Taylor-series expansion, employ Eqs. (4.17)-(4.18b), and obtain

$$\ddot{v}_i + \frac{EI}{\rho A l^4}\sum_{j=4}^{N} A_{ij} v_j = 0 \qquad i = 4, \ldots, N-1 \tag{4.22}$$

and

$$\sum_{j=4}^{N} c_j v_j = -\frac{HRl^3}{3EI[Z-w_N^*]^3} v_N \qquad \text{if } z \geq a_0 \tag{4.23a}$$

$$\sum_{j=4}^{N} c_j v_j = \frac{2E^*l^3}{EI}\sqrt{R}[a_0 - Z + w_N^*]^{1/2} v_N \qquad \text{if } z < a_0 \tag{4.23b}$$

Now, we eliminate v_N to obtain the following eigenvalue problem:

$$\ddot{v}_i + \frac{EI}{\rho A l^4}\sum_{j=4}^{N-1} \bar{A}_{ij} v_j = 0 \qquad i = 4, 5, \ldots, N-1 \tag{4.24}$$

where

$$\bar{A}_{ij} = A_{ij} - \frac{A_{iN}}{\eta_N} c_j$$

$$\eta_N = c_N - \begin{cases} -\frac{HRl^3}{3EI(Z-w_N^*)^3} & \text{if } z \geq a_0 \\ \frac{2E^*l^3\sqrt{R}}{EI}(a_0 - Z + w_N^*)^{1/2} & \text{if } z < a_0 \end{cases}$$

Solving the eigenvalue problem represented by Eq. (4.24) yields the natural frequencies and mode shapes of the AFM microcantilever. The resulting natural frequencies about the

contact and non-contact equilibrium positions are compared with the exact values for $Z = 5$ nm in Tables 4.2 and 4.3, respectively. It follows from Table 4.2 that using 13 grid points yields the first natural frequency about the contact equilibrium position to six significant figures. We note that, even employing less number of grid points in the DQM, results in acceptable accuracy. For example, the error in the calculated first natural frequency using 9 and 10 grid points is 0.045 % and 0.024 %, respectively. However, for vibrations about the non-contact equilibrium position, it follows from Table 3 that employing 11 grid points is enough to determine the fundamental natural frequency with a six significant figure accuracy and that employing 9 and 10 grid points estimates it with relative errors of 0.013 % and 0.0039 %, respectively. It is also seen that, for both of the contact and non-contact states, more grid points are required in the DQM to converge to the exact higher-order natural frequencies. For example, only when the number of grid points increases to 18, the DQM computed fifth natural frequency agrees with the exact value to four significant figures, whereas 10 grid-point DQM discretization is capable of accurately predicting the first natural frequency to four significant figures.

Comparing the exact values of the contact and non-contact natural frequencies presented in Tables 4.2 and 4.3 indicates that the difference between the contact and non-contact natural frequencies decreases for higher modes, whereas this difference is quite remarkable for the first and second modes. The same trend is observed for the difference between the natural frequencies of the free-end microcantilever and the AFM microcantilever operating in the non-contact region. The difference between the first natural frequencies of the free-

Table 4.2: Natural frequencies of the free microcantilever and the AFM microcantilever about the contact equilibrium position for $Z = 5$ nm

N	f_1(kHz)	f_2(kHz)	f_3(kHz)	f_4(kHz)	f_5(kHz)	f_6(kHz)
5	221.645					
6	226.174	437.511				
7	192.621	485.244	966.406			
8	189.330	462.281	978.822	1773.17		
9	191.616	444.178	981.451	1788.32	2825.15	
10	191.749	450.700	934.676	1840.74	2876.22	4179.96
11	191.706	452.914	944.057	1747.59	3011.12	4241.15
12	191.702	452.675	954.548	1765.49	2824.91	4497.15
13	191.703	452.585	953.648	1804.53	2862.50	4119.88
14	191.703	452.598	952.277	1799.78	2983.96	4195.25
15	191.703	452.601	952.837	1794.14	2962.12	4540.90
16	191.703	452.601	952.881	1794.56	2937.33	4445.72
17	191.703	452.601	952.879	1795.06	2939.80	4363.39
18	191.703	452.601	952.878	1795.04	2942.76	4373.16
Exact	191.703	452.601	952.878	1795.02	2942.33	4383.82
Free	51.5190	322.866	904.033	1771.54	2928.49	4374.66

Table 4.3: Natural frequencies of the free microcantilever and the AFM microcantilever about the non-contact equilibrium position for $Z = 5$ nm

N	f_1(kHz)	f_2(kHz)	f_3(kHz)	f_4(kHz)	f_5(kHz)	f_6(kHz)
5	48.3719					
6	50.6257	346.002				
7	51.7000	327.034	945.711			
8	51.2585	327.584	906.381	1766.85		
9	51.2999	321.483	919.748	1744.10	2823.88	
10	51.3066	322.250	894.223	1800.26	2843.51	4181.02
11	51.3068	322.847	898.122	1734.76	2975.75	4215.38
12	51.3068	322.851	904.879	1746.72	2824.84	4461.01
13	51.3068	322.831	904.546	1779.03	2855.77	4127.49
14	51.3068	322.831	903.965	1775.66	2965.49	4196.99
15	51.3068	322.832	903.994	1770.84	2946.97	4520.22
16	51.3068	322.832	904.022	1771.18	2923.97	4434.36
17	51.3068	322.832	904.022	1771.58	2926.11	4355.27
18	51.3068	322.832	904.021	1771.56	2928.87	4364.36
Exact	51.3068	322.832	904.021	1771.54	2928.49	4374.65
Free	51.5190	322.866	904.033	1771.54	2928.49	4374.66

end microcantilever and the AFM microcantilever is 272 % and 0.41 %, respectively, for the contact and non-contact states. This difference is reduced to 0.21 % and 0.0002 % for the sixth natural frequency.

Figures 4.2a and 4.2b display variation of the first and second natural frequencies with the initial tip/sample separation distance Z^* for three different cases: the free-end microcantilever and the AFM microcantilever operating in the contact and non-contact states. It is observed that, in the bistable region, the first natural frequency around the contact equilibrium position decreases as Z^* increases, but always remains larger than that around the non-contact position, despite the fact that the latter increases as Z^* increases. It is also seen that, except for a small portion of the bistable region ($Z^* < 3$ nm), the fundamental natural frequency in the non-contact region is very close to that of the free-end microcantilever. For oscillations about the contact equilibrium position, however, the fundamental natural frequency is totally different from that of the free-end microcantilever. It is further observed that the second natural frequency behaves very similar to the fundamental natural frequency and, as also demonstrated in Tables 4.3, the second natural frequency about the non-contact equilibrium is very close to that of the free-end microcantilever for the entire bistable region. The difference between the second natural frequencies of the free-end microcantilever and AFM microcantilever about the non-contact equilibrium is even smaller than that of the first natural frequencies. In addition, we note that, in the bistable phase, similar to the monostable phase, the natural frequencies of the AFM microcantilever about the contact equilibrium are always greater than the natural frequencies about the non-contact

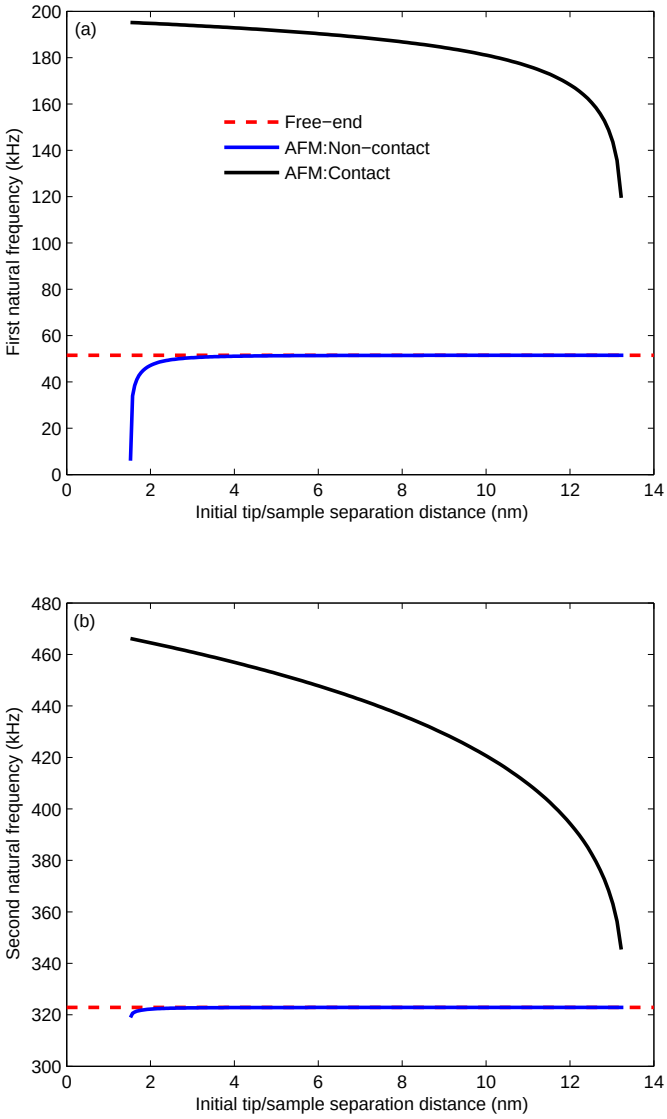

Figure 4.2: Variation of (a) the first (b) second natural frequencies with the initial tip/displacement distance in the bistable region.

equilibrium.

The mode shapes of the microcantilever are depicted in Fig. 4.3 for three different cases: vibrations about the non-contact equilibrium position ($Z = 5$ nm), vibrations about the contact equilibrium position ($Z = 5$ nm), and vibrations of the free-end microcantilever. As illustrated in the figure, the mode shapes about the non-contact static equilibrium are almost the same as those of the free-end microcantilever. On the other hand, the mode shapes of the microcantilever about the contact equilibrium position are significantly different from those of the free-end microcantilever. This difference is more notable for the first mode shape, similar to the trend observed for the natural frequencies.

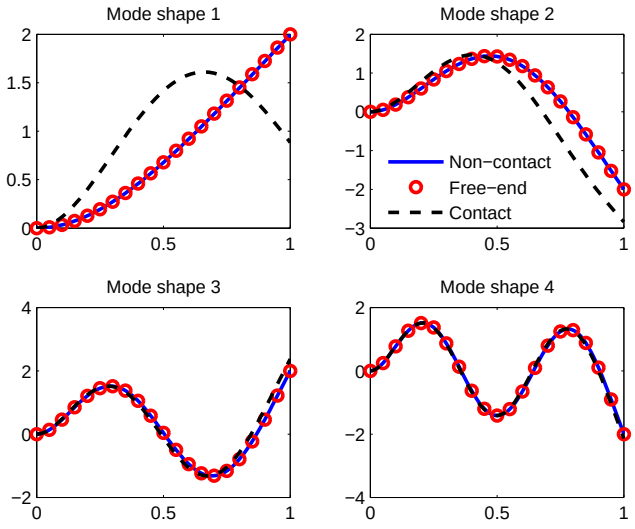

Figure 4.3: Comparison of the first four mode shapes with those of a free cantilever.

4.5 Forced Response of the AFM Probe

The reduced-order model equations (4.15) and (4.16) governing the time evolution of the system are solved, here, using two distinct methods: the brute-force approach [31] in which forward integration is performed in time to converge to a limit-cycle attractor and finite difference discretization [31] of the periodic orbit. It is, first, shown that the finite difference method (FDM) provides an accurate, efficient tool for calculating limit-cycle oscillations of the AFM probe compared to the rather expensive forward integration. Then, the FDM is employed to construct limit-cycle responses of the dynamical system for further numerical simulations. To this end, we re-scale the time so that the period is unity and discretize the periodic orbit by choosing a sufficiently dense set of uniform $(m+1)$ points: $\bar{t}_0 = 0$, $\bar{t}_1 = h$, $\bar{t}_2 = 2h$,..., $\bar{t}_p = ph$,..., $\bar{t}_m = mh = 1$; therefore the corresponding time step is $h = \frac{1}{m}$. The periodicity condition demands that the first and last points of the orbit are identical and, hence, the orbit includes only m distinct points. The DAE system represented by Eqs. (4.15) and (4.16) is solved at each of these points. Because the DAE system consists of $2(N-4)$ linear first-order differential equations and one nonlinear algebraic equation, the total number of equations to be solved is $m(2N-8)$ differential equations and m algebraic equations.

Equations (4.15) and (4.16) are represented at each point in the following form:

$$\begin{aligned} &\tfrac{d\bar{w}_{i,p}}{d\bar{t}} = \bar{w}^v_{i,p} \\ &\tfrac{d\bar{w}^v_{i,p}}{d\bar{t}} = -\bar{c}\bar{w}^v_{i,p} - \tfrac{EI}{\rho A\omega_1^2 l^4}\textstyle\sum_{j=4}^{N} A_{ij}\bar{w}_{j,p} + \bar{Y}\bar{\Omega}^2\sin(\bar{\Omega}\bar{t}_p) - \bar{c}\bar{Y}\bar{\Omega}\cos(\bar{\Omega}\bar{t}_p) \end{aligned} \qquad i = 4,5,\ldots,N-1 \tag{4.25}$$

$$\sum_{j=4}^{N} c_j \bar{w}_j = \begin{cases} -\frac{HRl^3}{6EIZ^{*3}\left[\bar{Z}-\bar{w}_{N,p}-\bar{Y}\sin(\bar{\Omega}\bar{t}_p)\right]^2} & \text{if } \bar{z} \geq \bar{a}_0 \\ -\frac{HRl^3}{6EI\bar{a}_0^2 Z^{*3}} + \frac{4E^* l^3 \sqrt{RZ^*}}{3EI}\left[\bar{a}_0 - \bar{Z} + \bar{w}_{N,p} + \bar{Y}\sin(\bar{\Omega}\bar{t}_p)\right]^{3/2} & \text{if } \bar{z} < \bar{a}_0 \end{cases} \tag{4.26}$$

where $\bar{w}_{i,p} = \bar{w}(\zeta_i, \bar{t}_p)$ and $\bar{w}^v_{i,p} = \bar{w}^v(\zeta_i, \bar{t}_p) = \frac{\bar{w}(\zeta_i,\bar{t}_p)}{d\bar{t}}$. A central difference scheme is, then, used to approximate the first derivative. Applying the FDM, we reduce the DAE system to a set of $m(2n-7)$ coupled algebraic equations; m of these equations are nonlinear and the rest are linear. A Newton-Raphson scheme is employed, next, to solve the nonlinear algebraic system.

Because the contact branch of the static bifurcation diagram is very close to the sample and the AFM tip is, in fact, stuck to the sample, this case is not of practical interest. Our attention, therefore, is limited to the non-contact branch where the tip is initially located in the bistable portion of the non-contact region. In particular, all of the numerical simulations are performed for $Z = 5$ nm (the corresponding value for the tip/sample equilibrium gap is obtained as $Z^* = 4.9789$ nm) and the nondimensional excitation amplitude $\bar{Y} = \frac{Y}{Z^*} = 0.175$ unless mentioned otherwise.

Modal damping is modeled here as a piecewise function. Because the AFM microcantilever experiences different dissipation mechanisms during the contact and non-contact phases, we model the modal damping with two distinct constant coefficients corresponding to the

non-contact and contact states as follows [29]:

$$\begin{cases} \bar{c}_1 = \frac{1}{Q} = 0.015 \\ \\ \bar{c}_2 = 4 \end{cases}$$

where Q is the quality factor, $\bar{c}_1$ denotes the damping coefficient corresponding to the non-contact regime where the energy is dissipated due to the surrounding air through a linear viscous damping mechanism, and $\bar{c}_2$ represents the damping coefficient for the contact regime where the energy is dissipated through a more sophisticated mechanism, which is modeled here, for simplicity, with a constant number (see [29] for more details).

The tip responses obtained with single-mode and multimode Galerkin discretizations are compared with those obtained with six and eight grid-point DQM approximations. Phase portraits of the tip oscillations obtained using different discretization schemes are plotted in Fig. 4.4 for the excitation frequency $f = 100$ kHz. As discussed later, the response consists of two periodic attractors for $f = 100$ kHz. Because we aim at comparison among different methods, we include only one of the attractors in this figure. It follows from Fig. 4.4 that, for the AFM parameters utilized here, using either a single-mode Galerkin discretization or a six grid-point DQM approximation leads to considerable inaccuracy in the predicted response, it might lead to qualitative errors. On the other hand, there is excellent agreement between the results of the multimode Galerkin and the eight-grid point DQM approximations. A combination of an eight-grid point DQM approximation and the FDM are, then, employed to perform all numerical simulations in what follows, unless otherwise mentioned. In addition, we mention that a convergence study has been performed to determine the number of points

required in the FDM for accurate discretization of the periodic orbit in the time domain. We found that using 200 points (i.e., $m = 200$) for temporal discretization of the orbit results in very accurate results.

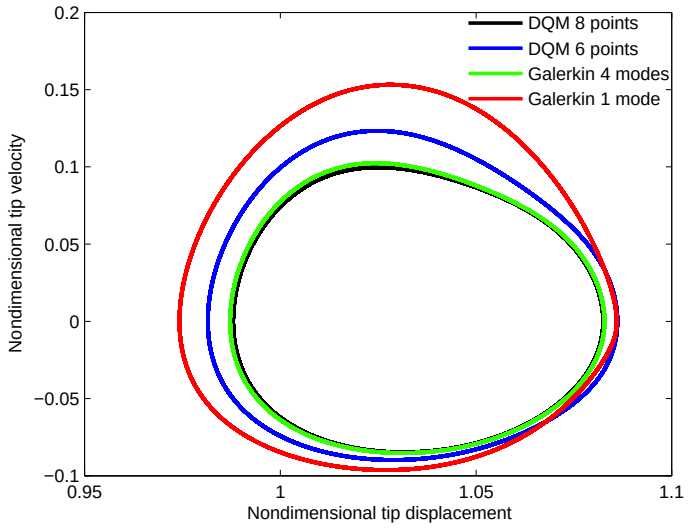

Figure 4.4: Phase portraits of the tip oscillation obtained with the different discretization schemes for $f = 100$ kHz.

Figure 4.5 displays the periodic responses of the dynamic system for the excitation frequency $f = 90$ kHz. Depending on the initial conditions, two different periodic orbits coexist. As illustrated in Figs. 4.5a and 4.5b, for some initial conditions, the tip exhibits periodic oscillations in the non-contact region and does not enter the contact region. However, starting with other initial conditions, the AFM tip gets stuck in a periodic attractor very close to the sample, which lies completely in the contact region, Figs. 4.5c and 4.5d. We note that the amplitude of the non-contact limit cycle is much larger than that in the contact region.

Figure 4.5b shows that the non-contact periodic response is almost purely harmonic, whereas Fig. 6c shows that the contact periodic response includes higher harmonics. We also note that, in spite of the high excitation amplitude (the excitation amplitude is assumed to be 17.5 % of the equilibrium gap) and the wide frequency range considered here, no tapping limit cycles are observed in the bistable region. In contrast, the numerical simulations in Chapter 3 and the results of Ref. [29] indicate that, in the monostable region, tapping periodic attractors are present for the same excitation amplitude and a wide range of the excitation frequency.

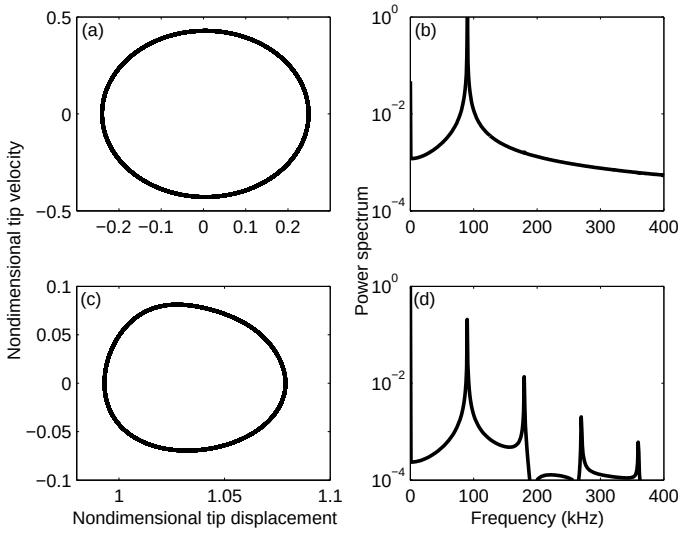

Figure 4.5: (a) Phase portrait of the non-contact periodic attractor $f = 90$ kHz and (b) its power spectrum; (c) phase portrait of the contact periodic attractor and (d) its power spectrum for $f = 90$ kHz.

The frequency-response curve (i.e., variation of the response amplitude with the excitation

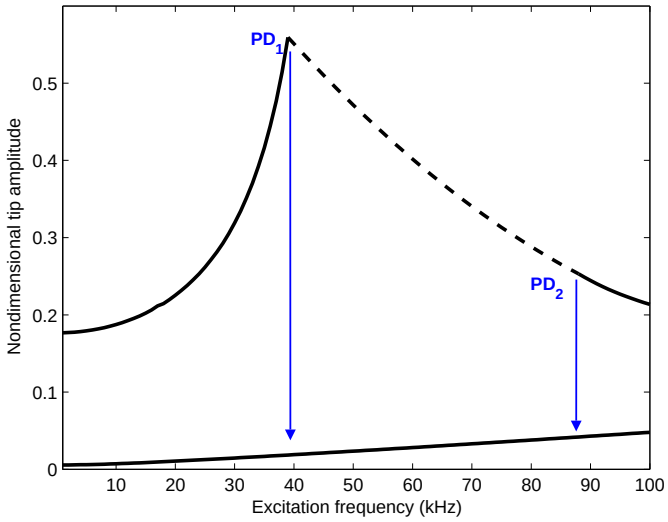

Figure 4.6: Variation of the tip amplitude with the excitation frequency for $\bar{Y} = 0.175$

frequency at a constant excitation amplitude) is presented in Fig. 4.6 for $\bar{Y} = 0.175$ and the frequency range $0 < f < 100$ kHz. It is observed that, except for 39 kHz $< f <$ 88 kHz, two stable period-one attractors coexist: low-amplitude and high-amplitude limit cycles. Surprisingly, the response amplitude is very low near the microcantilever first natural frequency (i.e., $f = 51.3068$ kHz). Beginning with a very small excitation frequency and performing a frequency sweep-up along the high-amplitude branch, we find that the tip amplitude increases until the limit cycle loses stability via a subcritical period-doubling bifurcation [31] at $PD_1 = f = 39$ kHz. As a result, the AFM tip jumps down to the stable attractor; that is, low-amplitude branch. Similarly, if we start with a large excitation frequency (e.g., $f = 100$ kHz) and decrease the excitation frequency along the high-amplitude branch, we observe that the periodic-one solution undergoes a subcritical period-doubling

bifurcation at $PD_2 = f = 88$ kHz and consequently jumps down to the stable branch. We note that the ratio of the amplitudes of the high- and low-amplitude limit cycles is large. This ratio is as large as 30 at $PD_1 = f = 39$ kHz. It means that the AFM microcantilever experiences a remarkable change in amplitude during the jumps occurring at PD_1 and PD_2. These transitions from the non-contact to the contact phase, which cause a sudden change in the tip amplitude, will lead to an improper imaging of the surface and is not desirable in practical atomic force microscopy. Such a behavior can be avoided by generating the frequency-response curves for different initial tip/sample separation distances and adjusting the excitation frequency accordingly.

We note that the stability of the periodic solutions is determined using Floquet theory. Since time explicitly appears in the governing equation, the corresponding dynamical system is a nonautonomous system. Therefore, we follow the procedure described in reference [31] for the stability analysis of nonautonomous systems. First, we transform the system of the ordinary-differential equations governing the time evolution of the dynamical system to the state space and form the Monodromy matrix associated with the periodic solution based on Floquet theory. Then, we calculate the eigenvalues of the Monodromy matrix, which are referred as Floquet multipliers. If all of the Floquet multipliers are within the unit circle, then the corresponding solution is asymptotically stable and called a stable periodic attractor or a stable limit cycle. However, if at least one of the Floquet multipliers is outside the unit circle, the associated solution is unstable and is referred to as unstable limit cycle. For more details, we refer the reader to Refs. [31, 80].

We also recall that two distinct methods were described earlier for the boundary condition implementation: one of them ends up with a DAE system, whereas the other one leads to a system of nonlinear ordinary-differential equations. The latter one was used here for the stability analysis of the periodic attractors because a well-established procedure is available to study the stability of periodic attractors governed by ordinary-differential equations.

To investigate the effect of the excitation amplitude, we generated frequency-response curves for several excitation amplitudes, but we did not observe any significant qualitative changes in the AFM microcantilever dynamics as long as the excitation amplitude does not exceed 17.5 % of the tip/sample equilibrium distance. As aforementioned, no tapping limit cycles are detected for small excitation amplitudes ($\bar{Y} \leq 0.270$), but increasing the excitation amplitude further (for a certain range of the excitation frequency) causes the microcantilever tip to touch the sample through a grazing bifurcation [39, 81, 82]. The phase portrait, Poincaré map, and power spectrum of the response are delineated in Fig. 4.7 for $\bar{Y} = 0.34$ and $f = 90$ kHz. Comparing this figure with Fig. 4.5, we conclude that the oscillation amplitude is increased notably as the excitation amplitude is increased from $\bar{Y} = 0.175$ to $\bar{Y} = 0.340$. In fact, a qualitative change takes place in the motion characteristics; the two low-amplitude contact and non-contact responses are replaced by a single high-amplitude tapping response. Comparing Fig. 4.7a with Figs. 4.5a and 4.5c reveals that the velocity of the vibrating tip is also increased as the excitation amplitude is increased. Figures 4.7b and 4.7c, on the other hand, indicate that a period-two periodic orbit is born due to the increase in the excitation amplitude. In addition to the period doubling, higher harmonics and a DC

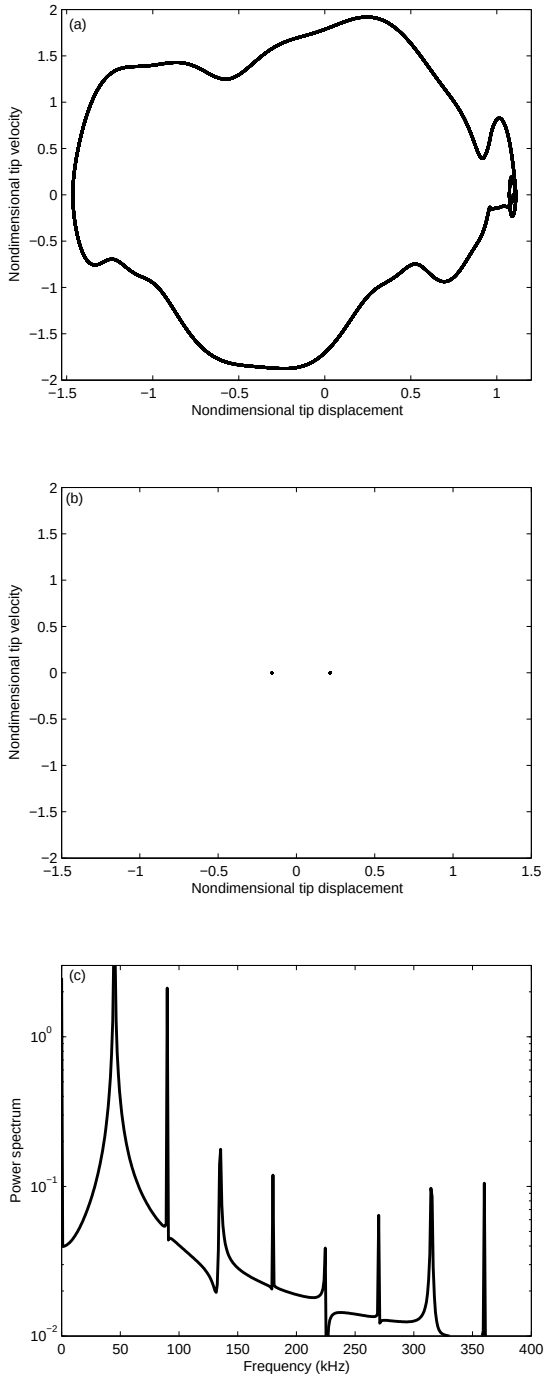

Figure 4.7: (a) Phase portrait, (b) Poincaré map, and (c) power spectrum of the tip response for $\bar{Y} = 0.340$.

component are clearly observed in the spectrum of the response, as shown in Fig. 7c. The presence of such frequencies in the tip response might be attributed to the nonlinear quadratic terms [30], which appear in the Taylor series expansion of both of the contact and non-contact forces; the contact force seems to be the force responsible for the generation of subharmonics. The power spectra presented in Figs. 4.5a and 4.5c, also, verify this conclusion; as long as the microcantilever tip oscillates in the non-contact region and does not touch the sample, the power spectrum includes only a frequency equal to that of the base excitation. However, for the contact (Fig. 4.5c) and tapping (Fig. 4.7a) limit cycles, their power spectra contain a zero-frequency and subharmonics, implying that contribution of the non-contact force in the generation of the subharmonics is insignificant. It should be, further, mentioned here that, in order to capture the rather complicated grazing dynamics of the AFM, we had to increase the number of grid points to 10. Moreover, we note that increasing the excitation amplitude further results, for certain excitation frequencies, in more complicated nonlinear phenomena, such as multi-period orbits and chaotic attractors. Such large excitation amplitudes, however, do not seem to be of practical interest and, therefore, are not pursued here.

Although this chapter was devoted to the dynamics of the AFM microcantilever in the bistable phase, we present some numerical results from the monostable phase for the AFM with the properties listed in Table 4.1. The initial tip/sample separation gap is assumed to be $Z = 60$ nm for all of the following numerical simulations unless otherwise mentioned. The damping coefficient in the present AFM is considerably larger than that of the AFM

used for numerical simulations in Chapter 3 and consequently different results are observed. The first observation is that, for a practical range of the excitation amplitude, the AFM tip always exhibits a periodic behavior and chaotic attractors or period doubling and grazing bifurcations are not detected. Figures 4.8a and 4.8b display, respectively, the phase portrait and power spectrum of the tip response for the excitation frequency $f = 52$ kHz and the excitation amplitude $\bar{Y} = \frac{Y}{Z^*} = 0.05$. These figures show that, even for a rather large value of the excitation amplitude, the response is still a periodic attractor.

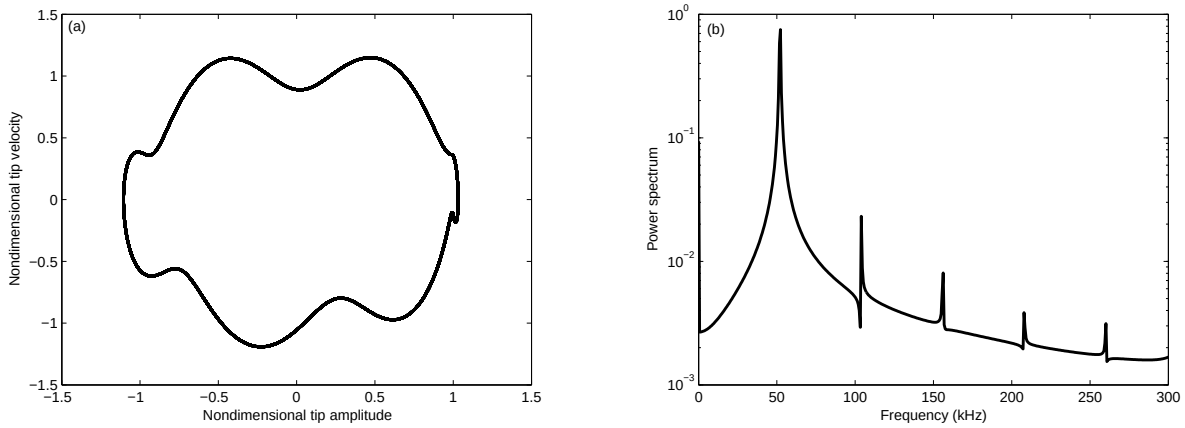

Figure 4.8: a) Phase portrait and (b) power spectrum of the tip response for $\bar{Y} = 0.05$ and $f = 52$ kHz.

Next, we explore the dynamics of the AFM tip by generating frequency-response curves for both of the amplitude and phase of the tip oscillations, which provide very useful and inclusive information, when the response is periodic. In what follows, we employ a combination of the eight-point DQM and the FDM, which was demonstrated to yield very accurate results. Variations of the response amplitude and phase are, respectively, plotted in Figs. 4.9a and

4.9b for $\bar{Y} = 0.0145$. We note that the actual excitation amplitude is the same as that used to generate Fig. 4.6 (i.e., the frequency curve in the bistable region). We keep the actual excitation amplitude Y fixed, but as the initial tip/sample gap Z and consequently the equilibrium tip/sample gap Z^* varies, we change the nondimensional excitation amplitude $\bar{Y} = \frac{Y}{Z^*}$. We also note that the response phase depicted in Fig. 4.9b is, in fact, the phase between the first harmonic of the response and the base excitation. As expected, the frequency-response curves in the monostable phase are totally different from those in the bistable phase.

Analogous to Fig. 3.10, four saddle-node bifurcations are observed for both of the response amplitude and phase. As observed in the figures, for the ranges of the excitation frequency $s_2 < f < s_1$ and $s_3 < f < s_4$, a low-amplitude non-contact limit cycle and a high-amplitude tapping limit cycle coexist. Depending on the tip initial conditions, the response is attracted to one of the two attractors. Starting with an excitation frequency (e.g, 49 kHz) below the fundamental natural frequency 51.3068 kHz and sweeping it up, we find that the tip amplitude increases until the limit cycle loses stability via a cyclic-fold bifurcation at $s_1 = f = 50.96$ kHz. As a result, the tip touches the sample and enters the contact region. We find that the tip amplitude increases along the saturated branch and enters the bistable region and follows the high-amplitude branch. Finally, at the excitation frequency $s_4 = f = 52.02$ kHz, the periodic solution loses stability due to another cyclic-fold bifurcation. Consequently, the tip amplitude jumps down to the stable low-amplitude branch. Similarly, starting with an excitation frequency above the first natural frequency (e.g., $f = 54$ kHz) and performing

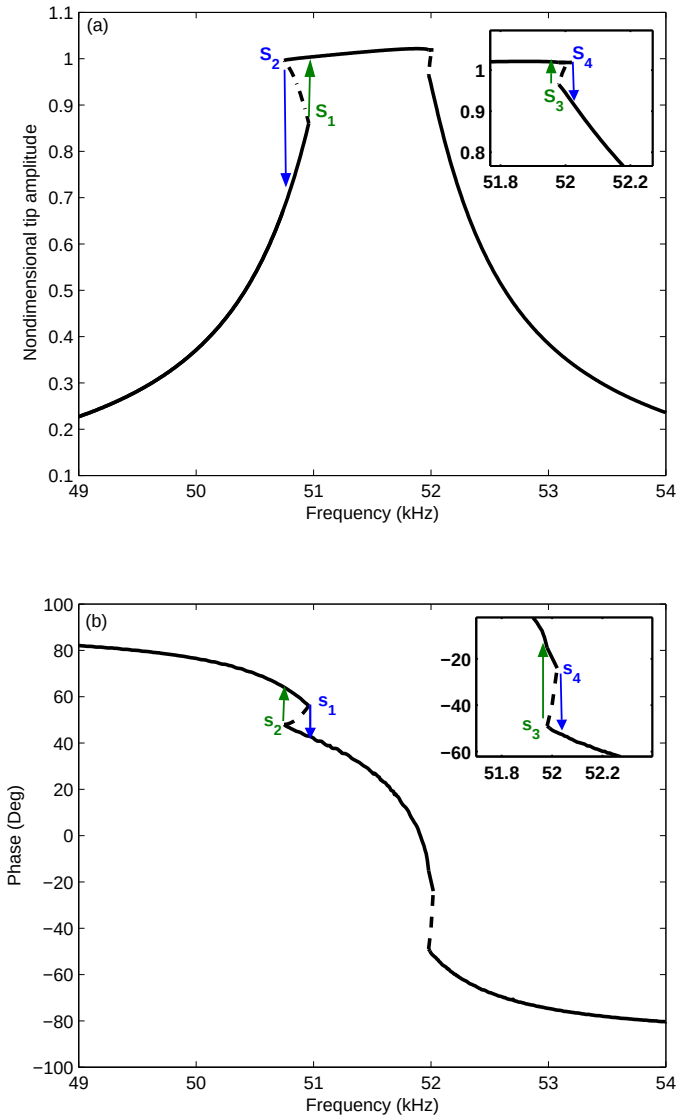

Figure 4.9: Variations of the (a) amplitude and (b) phase of the tip response with the excitation frequency for $\bar{Y} = 0.0145$.

a frequency sweep-down, we find that the tip amplitude increases along the low-amplitude branch. Decreasing the excitation frequency further results in a cyclic-fold bifurcation at $s_3 = f = 51.98$ kHz, which leads to a jump up to the high-amplitude branch. Finally, starting with an excitation frequency below the fundamental natural frequency and sweeping it down, we find that another cyclic-fold bifurcation occurs at $s_2 = f = 50.75$ kHz and the tip jumps down to the low-amplitude branch.

Similar variations are observed for the response phase. Starting with a frequency less than the fundamental frequency of the microcantilever and sweeping it up, we find that the phase response, which has a positive value, decreases and at $f = s_1$ a cyclic-fold bifurcation takes place and the AFM tip jumps down to another branch with a lower phase. If we keep increasing the excitation frequency and pass the first natural frequency (i.e., $f = 51.3068$ kHz), we find that another jump occurs due to a cyclic-fold bifurcation at $f = s_4 = 52.02$ kHz and the phase continues to decrease afterwards. On the other hand, beginning with a large excitation frequency, say $f = 54$ kHz, and performing a frequency sweep-down, we find that the phase increases starting from a negative value and jumps up at $f = s_3 = 51.98$ kHz. Decreasing the excitation frequency lower than the first natural frequency of the microcantilever results in another cyclic-fold bifurcation and a consequent jump to a higher phase at $f = s_2 = 50.75$ kHz. We note that two bistable regions are observed for both of the response amplitude and phase.

The effect of the initial tip/sample separation distance Z on the tip response is investigated through Figs. 4.10a and 4.10b. In these figures, the actual excitation amplitude Y is fixed

and equal to the excitation amplitude used to generate Fig. 4.9. We recall that, as the initial tip/sample gap changes, the microcantilever natural frequencies and mode shapes also change, but the interaction force arising between the tip and the sample has no significant impact on the natural frequencies and mode shapes of the microcantilever when the tip is located in the non-contact region. As the initial tip/sample gap Z and, consequently, the tip/sample equilibrium gap Z^* increases, the nondimensional excitation amplitude $\bar{Y} = \frac{Y}{Z^*}$ decreases. As seen in the figures, starting with a small initial tip/sample separation gap in the monostable phase (e.g., $Z = 20$ nm) and increasing Z, we find that the tip amplitude increases linearly along the tapping branch. We note that, for this portion of the diagram, the AFM tip touches the sample occasionally during its periodic motion. At $Z = s_1 = 52$ nm, the corresponding dynamical system undergoes a cyclic-fold bifurcation. As a result, the AFM tip jumps down to the low-amplitude non-contact branch and remains unaffected with a further increase of Z. For this portion of the bifurcation diagram, the AFM tip does not touch the sample. Similarly, starting with a large tip/sample separation distance in the reference configuration (e.g., $Z = 100$ nm) and decreasing Z, we find that the response amplitude remains constant and does not change with Z at the outset. Then, at $Z = s_2 = 43$ kHz, a cyclic-fold bifurcation occurs and the tip jumps up to the tapping branch with a larger amplitude. A further decrease of Z results in a linear decrease in the response amplitude. On the other hand, the response phase bifurcation diagram looks slightly different. Starting with $Z = 20$ nm and increasing the bifurcation parameter Z, we find that the response phase increases similar to the response amplitude but jumps up as a result of a cyclic-

fold bifurcation at $Z = s_1 = 52$ nm, in contrast to the tip amplitude, and then remains unchanged. We note that the phase difference between the response first harmonic and the base excitation is always positive for the range of initial tip/sample gaps considered here.

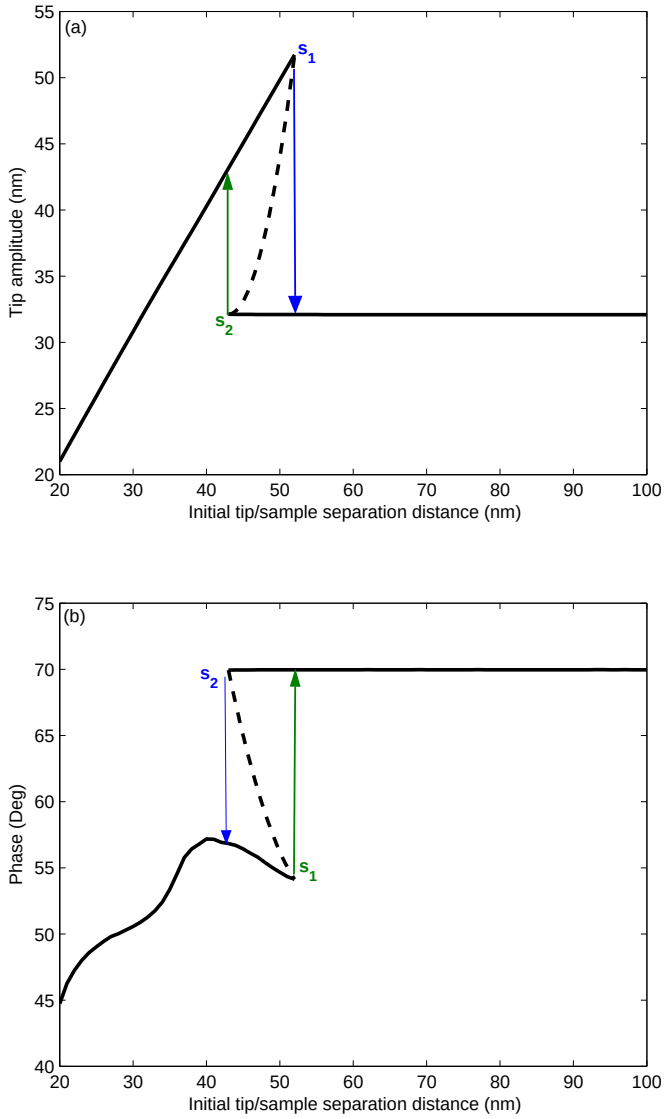

Figure 4.10: Variations of the (a) amplitude and (b) phase of the tip response with the initial tip/sample separation distance for $f = 50.5$ kHz.

Chapter 5

Conclusions and Future Work

Conclusions

This dissertation focused on the study of the nonlinear dynamics of tapping mode AFMs. We developed a distributed-parameter model for the 3-D microcantilever/tip structure based on the Euler-Bernoulli beam theory. Since the interaction forces arising between the tip and the sample are highly nonlinear, the initial-boundary-value problem governing the motion of the AFM microcantilever does not seem to admit closed-form analytical solutions. Therefore, we used reduced-order models to convert the partial-differential equation of motion and associated boundary conditions into a set of nonlinear ordinary-differential or differential-algebraic equations in terms of the temporal variable.

Starting with the static problem, we generated the static bifurcation curve for the tip/sample equilibrium separation distance in terms of the initial tip/sample separation distance in the

reference configuration. This bifurcation diagram shows that, depending on the initial location of the microcantilever tip, the AFM operates either in the monostable phase or in the bistable phase. Then, we determined the natural frequencies and mode shapes of the AFM microcantilever. The natural frequencies and mode shapes of the AFM microcantilever about a non-contact equilibrium were found to be almost the same as those of the free-end microcantilever for both of the monostable and bistable phases. However, the natural frequencies and mode shapes of the microcantilever about a contact equilibrium are considerably different from those of the free-end microcantilever.

We employed a multimode Galerkin discretization and a rigorous time integration scheme to study the nonlinear dynamics of an atomic force microscope cantilever in the monostable phase. We examined the dynamics of the AFM microcantilever through various numerical simulations carried out for a wide range of excitation frequency and amplitude. A new insight has been gained into the dynamics of tapping mode atomic force microscopy. It was found that a one-mode Galerkin discretization, although sufficient for predicting some aspects of the nonlinear dynamics of the cantilever tip, such as non-contact periodic attractors, is not able to capture all nonlinear phenomena, such as period doubling and grazing bifurcations and chaotic motion. It was also found that at least four modes are required for accurate determination of the cantilever dynamical characteristics. Contribution of each mode to the tip displacement and velocity was investigated and it was shown that the higher-order modes have significant effect on the velocity. Two different routes to chaos were identified: the well-known classical scenario of a sequence of period doubling bifurcations and the grazing

scenario, which is a characteristic of impact oscillators and non-smooth dynamical systems.

We also developed a point-mass model for the AFM microcantilever subjected to a base displacement excitation. A comparison between numerical results obtained based on this point-mass model and those of a single-mode Galerkin discretization revealed that the point-mass model is in complete agreement with the single-mode Galerkin results.

A differential quadrature method was utilized to discretize the microcantilever equation and associated boundary conditions and simulate the static and free-vibration responses of the scanning probe in the bistable phase. It was found that, even with five grid points, the DQM accurately predicts the equilibrium static deflection. However, many more grid points are needed to determine the natural frequencies with sufficient accuracy. The higher the mode is, the larger the number of required grid points is. In addition, the forced vibration responses of the AFM probe to a harmonic base excitation were investigated using a combination of the DQM and a finite difference method (FDM) to discretize, respectively, the spatial and temporal derivatives in the governing equation and associated boundary conditions. A convergence study was conducted to determine the number of DQM grid points and FDM mesh points required to provide sufficient accuracy. A dynamic analysis of the AFM probe revealed that, for a wide range of the excitation frequency, the microcantilever exhibits two distinct behaviors, depending on the initial conditions: a non-contact periodic attractor far from the sample and a contact attractor which is, effectively, stuck to the sample. Furthermore, we found that the dynamics of the AFM microcantilever in the bistable phase is totally different from those in the monostable phase. For instance, cyclic-fold bifurcations

are dominant features of the nonlinear dynamics in the monostable phase. However, in the bistable phase, period doubling bifurcations as well as cyclic-fold bifurcations are present.

We note that, although we have performed numerical simulations for certain numerical values corresponding to a real AFM's properties, the methodology developed in this investigation may be utilized to study the dynamics of any AFM with different geometrical and material properties. We also note that variation in the AFM properties may affect the responses significantly, but the methodology presented here can be still employed to predict the nonlinear dynamics of the AFM microcantilever. Assessing the validity of the results obtained through this research can only be done by performing carefully designed experiments that would bring out such responses.

Future Work

As aforementioned, recently several investigations proposed the use of higher flexural modes to enhance the sensitivity to tip/sample interactions. These studies have given rise to the development of a new operational technique called bimodal AFM [37,38,40–44,83]. In bimodal atomic force microscopy, the first and second flexural modes of the AFM microcantilever are excited simultaneously. This method opens two new channels to get information about the sample: the amplitude and phase of the second mode as well as the combination frequencies of the two modes. It has been demonstrated in the early research on the bimodal AFM that simultaneous excitation of the first two modes of the microcantilever, in the presence of modal couplings, provides the ability to detect very small variations in the long-range van

der Waals force [37,38,83]. Due to the high sensitivity of the second mode to the long-range tip/sample interactions, we can use the bimodal techniques in the non-contact operation of the AFM. This non-contact operation of the AFM causes a significant reduction in the magnitude of the tip/sample interaction force and therefore bimodal atomic force microscopy opens new avenues to generate high-resolution topographical images of soft materials like living cells. In spite of the practical importance of the bimodal AFM techniques, the theory of this microscopy technique has not been well developed and the cantilever nonlinear dynamics are to be investigated yet.

Since in the bimodal operational mode, the microcantilever can oscillate only in the non-contact regime, the method of harmonic balance is very convenient to render a reliable analytical formulation for the nonlinear dynamics of the AFM tip. In the method of harmonic balance, the harmonic functions are employed to approximate the temporal part of the response and reduce the spatiotemporal partial-differential equation governing the microcantilever motion to a set of ordinary-differential equations in terms of the space variable. The three-dimensional microcantilever/tip structure may be modeled as a continuous beam as developed in Chapter 2. We note that the partial-differential equation appearing in equation (2.12) is a linear equation and therefore application of the method of harmonic balance transforms the PDE to a set of linear ordinary-differential equations, which can be solved analytically. More complicated motions, such as quasi-periodic or chaotic motions, are not captured with the method of harmonic balance.

As another future investigation, we suggest to take the capillary effect into consideration

in modeling tip/sample interactions. Using the multimode Galerkin or DQM discretization methods, one can study the more complicated dynamical system to explore the effect of the capillary forces on the dynamics of the AFM probe. These forces arise between the AFM tip and the sample due to a water bridge, which is formed between the tip and the sample under ambient conditions.

Bibliography

[1] S. Kalinin and A. Gruverman. Scanning Probe Microscopy: Electrical and Electromechanical Phenomena at the Nanoscale. Springer, New York, USA, 2007.

[2] G. Binning, H. Roher, and C. Gerber. Surface studies by scanning tunneling microscopy. Phys. Rev. Lett., **49**, 57, 1982.

[3] G. Binnig, C.F. Quate and C. Grober. Atomic force Microscope. Phys. Rev. Lett., **56**, 930, 1986.

[4] F.J. Giessibl. Atomic resolution of the silicon (111)-(7×7) surface by atomic force microscopy. Science, **267**, 68, 1995.

[5] F.J. Giessibl. Advances in atomic force microscopy. Rev. Modern Phys., **75**, 949, 2003.

[6] R. Garcia. Amplitude Moulation Atomic Force Microscopy. Wiley-VCH, Weinheim, Germany, 2010.

[7] A. Raman, J. Melcher and R. Tung. Cantilever dynamics in atomic force microscopy. Nanotoday, **3**, 20, 2008.

[8] R Garcia and R Perez. Dynamic atomic force microscopy methods. Surf. Sci. Rep., **47**, 197, 2002.

[9] Y. Gan. Atomic and subnanometer resolution in ambient conditions by atomic force microscopy. Surf. Sci. Rep., **64**, 99, 2009.

[10] R. Garcia, R. Magerle, and R. Perez. Nanoscale compositional mapping with gentle forces. Nat. Matter., **6**, 405, 2007.

[11] R. Garcia and A.S. Paulo. Attractive and repulsive tip-sample interaction regimes in tapping-mode atomic force microscopy. Phys. Rev. B, **60**, 4961, 1999.

[12] A.S. Paulo and R. Garcia. Unifying theory of tapping-mode atomic-force microscopy. Phys. Rev. B, **66**, 041406, 2002.

[13] A.S. Paulo and R. Garcia. High-resolution imaging of antibodies by tapping-mode atomic force microscopy: attractive and repulsive tip-sample interaction regimes. Biophys. J., **78**, 1599, 2000.

[14] R. Magerle. Nanotomography. Phys. Rev. Lett., **85**, 2749, 2000.

[15] D.J. Muller. AFM: A Nanotool in Membrane Biology. Biochemistry, **47**, 7986, 2008.

[16] T.S. Druzhinina, S. Hoeppener, and U.S. Schubert. Microwave-assisted fabrication of carbon nanotube AFM tips. Nano Lett., **10**, 4009, 2010.

[17] M. Nikkhah, J.S. Strobl, R. De Vita, and M. Agah. The cytoskeletal organization of breast carcinoma and fibroblast cells inside three dimensional (3-D) isotropic silicon microstructures. Biomaterials, **31**, (16) 4552, 2010.

[18] H.R. Hertz. Gesammelte Werke (collected works), Leipzig, Germany, Vol.1, p. 155, 1895.

[19] K.L. Johnson, K. Kendall, and A.D. Roberts. Surface energy and contact of elastic solids. Proc. R. Soc. A, **324**, 301, 1971.

[20] B.V. Derjaguin, V.M. Muller, and Y. Toporov. Effect of contact deformations on adhesion of particles. J. Colloid Interface Sci., **53**, 314, 1975.

[21] L. Zitzler, S. Herminghaus, and F. Mugele. Capillary forces in tapping mode atomic force microscopy. Phys. Rev. B, **66**, 155436, 2002.

[22] N. Hashemi, H. Dankowicz, and M.R. Paul. The nonlinear dynamics of tapping mode atomic force microscopy with capillary force interactions. J. Appl. Phys., **103**, 093512, 2008.

[23] J.E. Sader, S.P. Jarvis. Accurate formulas for interaction force and energy in frequency modulation force spectroscopy., Appl. Phys. Lett., **84**, 1801, 2004.

[24] A.S. Paulo and R. Garcia. Tip-surface forces, amplitude, and energy dissipation in amplitude-modulation (tapping mode) force microscopy. Phys. Rev. B, **64**, 193411, 2001.

[25] M. Marth, D. Maier, J. Honerkamp, R. Brandsch, and G Bar. A unifying view on some experimental effects in tapping-mode atomic force microscopy. J. Appl. Phys., **85**, 7030, 1999.

[26] W. Van de Water and J. Molenaar. Dynamics of vibrating atomic force microscopy. Nanotechnology, **11**, 192, 2000.

[27] S. Misra, H. Dankowicz and M.R. Paul. Degenerate discontinuity-induced bifurcations in tapping-mode atomic-force microscopy. Physica D, **239**, 33, 2010.

[28] S.I. Lee, S.W. Howell, A. Raman, and R. Reifenberger. Nonlinear dynamics of microcantilevers in tapping mode atomic force microscopy: A comparison between theory and experiment. Phys. Rev. B, **66**, 115409, 2002.

[29] S.I. Lee, S.W. Howell, A. Raman, and R. Reifenberger. Nonlinear dynamic perspectives on dynamic force microscopy. Ultramicroscopy, **97**, 185, 2003.

[30] A.H. Nayfeh and D.T. Mook. Nonlinear Oscillations. Wiley, New York, 1979.

[31] A.H. Nayfeh and B. Balachandran. Applied Nonlinear Dynamics: Analytical, Computational, and Experimental Methods. Wiley, New York, 1995.

[32] M.Stark, R.W. Stark, W.M. Heckl, and R. Guckenberger. Inverting dynamic force microscopy: From signals to time-resolved interaction forces. Proc. Natl. Acad. Sci. USA, **99**, 8473, 2002.

[33] T.R. Rodriguez and R. Garcia. Tip motion in amplitude modulation (tapping-mode) atomic-force microscopy: Comparison between continuous and point-mass models. Appl. Phys. Lett., **80**, 1646, 2002.

[34] S. Basak and A. Raman. Dynamics of tapping mode atomic force microscopy in liquids: Theory and experiments. Appl. Phys. Lett., **91**, 064107, 2007.

[35] D. Kiracofe and A. Raman . On eigenmodes, stiffness, and sensitivity of atomic force microscope cantilevers in air versus liquids. J. Appl. Phys., **107**, 033506, 2010.

[36] J.R. Lozano, D. Kiracofe, J. Melcher, R. Garcia and A. Raman. Calibration of higher eigenmode spring constants of atomic force microscope cantilevers. Nanotechnology, **21**, 465502, 2010.

[37] T.R. Rodriguez and R. Garcia. Compositional mapping of surfaces in atomic force microscopy by excitation of the second normal mode of the microcantilever. Appl. Phys. Lett., **84**, 449, 2004.

[38] J.R. Lozano and R. Garcia. Theory of phase spectroscopy in bimodal atomic force microscopy. Phys. Rev. B, **79**, 014110, 2009.

[39] W. Chin, E. Ott, H.E. Nusse, and C. Grebogi. Grazing bifnrcations in impact oscillators. Phys. Rev. E, **50**, 4427, 1994.

[40] N.F. Martinez, S. Patil, J.R. Lozano, and R. Garcia. Enhanced compositional sensitivity in atomic force microscopy by the excitation of the first two flexural modes. Appl. Phys. Lett., **89**, 153115, 2006.

[41] M.D. Aksoy, A. Atalar. Force spectroscopy using bimodal frequency modulation atomic force microscopy. Phys. Rev. B, 83 (2011) 075416.

[42] P. Thota, S. MacLaren, H. Dancowicz, Appl. Phys. Lett., **91**, 093108, 2007.

[43] B.J. Rodriguez, C. Callahan, S.V. Kalinin, and R. porksch. Dual-frequency resonance-tracking atomic force microscopy. Nanotechnology, **18**, 475504, 2007.

[44] J.R. Lozano, R. Garcia. Theory of Multifrequency Atomic Force Microscopy. Phys. Rev. Lett., **100**, 076102, 2008.

[45] O. Sahin, C.F. Quate, O. Solgaard, and A Atalar. An atomic force microscope tip designed to measure time-varying nanomechanical forces. Nat. Nanotechnol., **2**, 507, 2007.

[46] O. Sahin. Time-varying tip-sample force measurments and steady-state dynamics in tapping-mode atomic force microscopy. Phys. Rev. B, **77**, 11505, 2008.

[47] O. Sahin, N. Erina. High-resolution and large dynamics range nanomechanical mapping in tapping-mode atomic force microscopy. Nanotechnology, **19**, 445717, 2008.

[48] S. Husale, H.H.J. Persson, and O. Sahin. DNA nanomechanics allows direct digital detection of complementary DNA and microRNA targets. Nature, **462**, 1075, 2009.

[49] M. Moreno-Moreno, A. Raman, J. Gomez-Herrero, and R. Reifenberger. Parametric resonance based scanning probe microscopy. Appl. Phys. Lett., **88**, 193108, 2006.

[50] A.H. Nayfeh. Perturbation Methods. Wiley, New York, 1973.

[51] A.H. Nayfeh. Introduction to Perturbation Technics. Wiley, New York, 1981.

[52] R.E. Bellman and J. Casti. Differential quadrature and long term integration. J. Math. Anal. Appl., **34**, 235, 1971.

[53] C.W. Bert and M. Malik. Differential quadrature method in computational mechanics: A review. Appl. mech. Rev., **49**, 1, 1996.

[54] S. Tomasiello. Differential quadrature method: Application to initial-boundary-value problems. J. Sound Vib, **218**, 573, 1998.

[55] C. Shu. Differential Quadrature and Its Application in Engineering. Springer, London, Great Bretain, 2000.

[56] S.A. Emam and A.H. Nayfeh. On the nonlinear dynamics of a buckled beam subjected to a primary-resonance excitation. Nonlinear Dynam., **35**, 1, 2004.

[57] S.A. Emam and A.H. Nayfeh. Nonlinear Responses of Buckled Beams to Subharmonic-Resonance Excitations. Nonlinear Dynam., **35**, 105, 2004.

[58] F. Jamitzky, M. Stark, W. Bunk, W.M. Heckl, and R.W. Stark. Chaos in Dynamic Atomic Force Microscopy. Nanotechnology, **17**, 213, 2006.

[59] S. Hu and A. Raman. Chaos in Atomic Force Micrscopy. Phys. Rev. Lett., **96**, 036107, 2006.

[60] F. Jamitzky and R.W. Stark. Intermittency in Amplitude Modulated Dynamic Atomic Force Microscopy. Ultramicroscopy, **110** 618, 2010.

[61] S. Timoshenko and J.N. Goodier. Theory of Elasticity. McGraw-Hill, New York, 1951.

[62] V. Acary and B. Bernard. Numerical Methods for Nonsmooth Dynamical systems. Springer-Verlag, Berlin, 2008.

[63] R.E. Bellman, B.G. Kashef, and J. Casti. Differential quadrature: a technique for the rapid solution of nonlinear partial differential equations. J. Comput. Phys., **10**, 40, 1972.

[64] R.E. Bellman, B.G. Kashef, E.S. Lee, and R. Vasudevan. Solving hard problems by easy methods: differential and integral quadrature., Comp & Math with Appl., **1**, 133, 1975.

[65] R.E. Bellman, B.G. Kashef, E.S. Lee, and R. Vasudevan. Differential quadrature and splines. Comp & Math with Appl., **1**, 371, 1975.

[66] J.R. Quang, C.T. Chang. New insights in solving distributed system equations by the quadrature methods-I. Comput Chem Engrg., **13** 779, 1989.

[67] J.R. Quang, C.T. Chang. New insights in solving distributed system equations by the quadrature methods-II Comput Chem Engrg., **13** 1017, 1989.

[68] C. Shu, B.E. Richards. High resolution of natural convection in a square cavity by generalized differential quadrature. Proc. of 3rd Conf. on Adv. in Numer. Methods in Eng: Theory and Appl., Swansee, UK, **2** 978, 1990.

[69] C. Shu, Y.T. Chew. Fouriere expansion-based differential quadrature and its application to Helmholtz eigenvalue problems., Commun. Number Methods Eng., **13** (8) 643, 1997.

[70] C. Shu, H. Xue, Explicit computation of weighting coefficients in the harmonic differential quadrature. J. Sound Vib., **204** (3) 549, 1997.

[71] R.M. Lin, M.K. LIM, and H. DU. Defection of plates with nonlinear boundary supports using generalized differential quadrature. Comput. Struct., **53** 993, 1994.

[72] F. Najar, S. Choura, S. El-Borgi, E.M., Abdel-Rahman, and A.H. Nayfeh. Modeling and design of variable-geometry electrostatic microactuators. J. Micromech. Microeng., **15** 419, 2005.

[73] F. Najar, S. Choura, S. El-Borgi, E.M., Abdel-Rahman, and A.H. Nayfeh. Dynamic analysis of variable-geometry electrostatic microactuators. J. Micromech. Microeng., **16** 2449, 2006.

[74] S.K. Jang, C.W. Bert, and A.G. Striz, Application of differential quadrature to static analysis of structural components. Int. J. Numer. Method Eng., **28** (3) 561, 1989.

[75] X. Wang, C.W. Bert. A new approach in applying differential quadrature to static and free vibrational analysis of beams and plates. J. Sound Vib., **162** (3) 566, 1993.

[76] C. Shu and H. Du. Implementation of clamped and simply supported in the GDQ free vibration analysis of beams and plates. Int. J. Solids Struc., **34** (7) 817, 1997.

[77] C. Shu and H. Du. A generalized approach for Implementing general boundary conditions in the GDQ free vibration analysis of plates. Int. J. Solids Struc., **34** (7) 837, 1997.

[78] P. Kunkel and V. Mehrmann. Differential-algebraic equations : analysis and numerical solution. Europian Mathematical Society, Z?rich, Switzerland, 2006.

[79] U.M. Ascher and L.R. Petzold. Computer methods for ordinary differential equations and differential-algebraic equations. Society for Industrial and Applied Mathematics, Philadelphia, 1998.

[80] J.V. Jose, E.J. Saletan. Classical Dynamics: A Contemporary Approach. Cambridge University Press, Cambridge, UK, 1998.

[81] X.H. Long, G. Lin, and B. Balachandran. Grazing bifurcations in an elastic structure excited by harmonicimactor motions. Physica D., **237**, 1129, 2008.

[82] A.J. Dick, B. Balachandran, H. Yabuno, M. Numatsu, K. Hayashi, M. Kuroda, and K. Ashida. Utilizing nonlinear phenomena to locate grazing in the constrained motion of a cantilever beam. Nonlinear Dynam., **57** 335, 2009.

[83] N.F. Martinez, J.R. Lozano, E.T. herruzo, F. Garcia, C. Richter, T. Sulzbach, and R. garcia. Bimodal atomic force microscopy imaging of isolated antibodies in air and liquids. nanotechnology, **19**, 384011, 2008.